

# **Nanostructures Technology, Research and Applications**

## **Academic and Research Staff**

Dr. David J.D. Carter, James M. Carter, Robert C. Fleming, Dr. James G. Goodberlet, Mark. K. Mondol, Dr. Mark L. Schattenburg, and Professor Henry I. Smith.

Visiting Scientists and Research Affiliates

Dr. Patrick N. Everett and Ken-ichi Murooka.

## **Graduate Students**

Alek Bernshteyn, Carl Chen, Joy Cheng, Alexei Ercheck, Maya Farhoud, Juan Ferrera, Mark Finlayson, Dario Gil, Jeffrey T. Hastings, Yaowu Hao, Minha Hwang, Keith Jackson, Jalal Kahn, Paul Konkola, Michael H. Lim, Anthony Lochtefeld, Mitchell W. Meinhold, Rajesh Menon, Euclid Moon, Thomas E. Murphy, David Pflug, Minghao Qi, Farhan Rana, Timothy A. Savas, Oliver Stolz, Michael Walsh, Feng Zhang.

## **Technical and Support Staff**

James Daley, Cynthia Lewis and Edward Murphy

## **1. Nanostructures Laboratory**

The Nanostructures Laboratory (NSL) at MIT develops techniques for fabricating surface structures with feature sizes in the range from nanometers to micrometers, and uses these structures in a variety of research projects. The NSL is closely coupled to the Space Microstructures Laboratory (SML) with which it shares facilities and a variety of joint programs. The NSL and SML include facilities for lithography (photo, interferometric, electron-beam, and x-ray), etching (chemical, plasma and reactive-ion), liftoff, electroplating, sputter deposition, and e-beam evaporation. Much of the equipment, and nearly all of the methods, utilized in the NSL/SML are developed in house. Generally, commercial processing equipment, designed for the semiconductor industry, cannot achieve the resolution needed for nanofabrication, is inordinately expensive, and lacks the required flexibility for our research. The research projects within the NSL/SML fall into three major categories: (1) development of nanostructure fabrication technology; (2) short-channel semiconductor devices, nanomagnetism and microphotonics; (3) periodic structures for x-ray optics, spectroscopy, atomic interferometry and nanometer metrology.

## **2. Scanning-Electron-Beam Lithography**

### **Sponsors**

National Science Foundation - DMR-9808941  
U.S. Army Research Office – DAAD19-99-1-0280  
Air Force Office of Scientific Research (AFOSR) - F49620-96-1-0126

### **Project Staff**

Mark K. Mondol, Dr. James Goodberlet and Professor Henry I. Smith

Figure 1 is a photograph of the scanning-electron-beam lithography system (VS-2A) located in the scanning-electron-beam lithography (SEBL) facility, Room 38-165. This instrument was obtained as a donation from IBM in 1993. Its digital pattern generator is based on a commercial

high-performance array processor, which uses dual RISC processors. The system is capable of creating large-area patterns composed of multiple stitched fields. Conversion software has been developed which allows a CAD data file to be fractured and translated prior to exposure by the electron-beam tool.

The VS-2A can expose substrates up to 20 cm diameter, at linewidths down to 70 nm. The goals of the SEBL facility are to: (1) provide the MIT research community with an in-house SEBL capability for writing directly on experimental device substrates; (2) advance the state-of-the-art in SEBL, particularly with regards to pattern placement accuracy and long-range spatial-phase coherence; and (3) pattern x-ray nanolithography masks for in-house use. In order to enable writing concentric circular patterns, such as Fresnel zone plates, software was developed to generate arbitrary arcs of an annulus with user-specified start and finish radii and angles.

In 1999, VS-2A was used to write x-ray masks consisting of: gratings and waveguides for channel-dropping filters, having long-range spatial-phase coherence, achieved via spatial phase locking; deep sub-100 nm channel-length dual-gate MOSFETs; diffractive marks for experiments on IBBI alignment; and zone plate lenses for a novel optical-communication component.

Photomasks were written consisting of: arrays of Fresnel phase-shift zone plates on quartz for experiments in zone-plate-array lithography (ZPAL); and 100 nm features on quartz masks for deep-UV contact photolithography experiments.

VS-2A was also used in the mode of direct-writing on device substrates for projects on: magnetic storage; a super-luminescent LED using a two-dimensional photonic band gap; 1-D photonic bandgap structures; 3-D photonic bandgap structures; contacts to bismuth nanowires; a new resist based on colloidal gold; resolution standards for scanning probe systems.

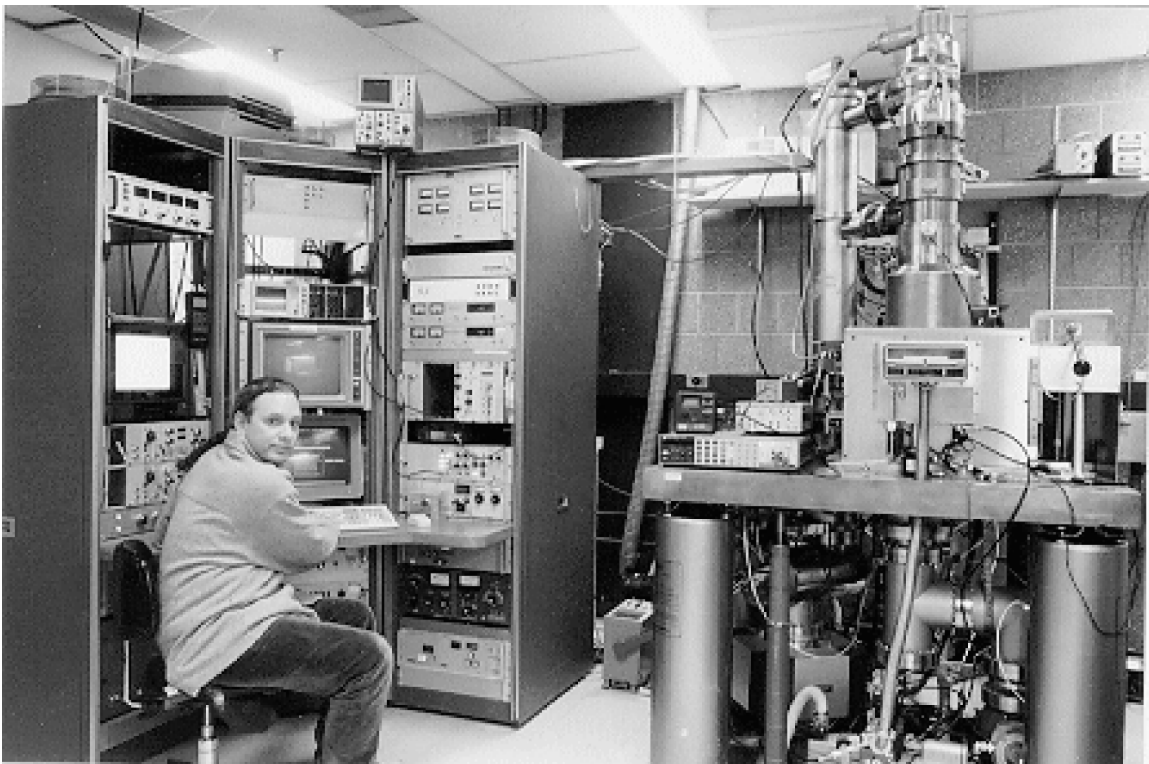


*Figure 1. Photograph of the VS-2A scanning-electron-beam lithography system. The operator is Research Specialist Mark Mondol.*

VS-2A was also used extensively in experiments on spatial-phase-locked e-beam lithography, in a program aimed at achieving nanometer-level pattern placement accuracy. A new method for high-precision measurement of interfield stitching errors was also developed based on a modified moire' technique.

The scanning-electron-beam lithography facilities of the NSL will soon be augmented through the acquisition of a Raith Turnkey 150. This system features a beam diameter as fine as 5nm, and can operate at beam energies as low as 10eV and as high as 30keV. It should enable feature sizes down to 30nm to be achieved. The primary utilization of the Raith system will be in a program to develop spatial-phase-locked e-beam lithography (SPLEBL).

### **3. Spatial-Phase-Locked Electron-Beam Lithography**

#### **Sponsors**

U.S. Army Research Office  
Grant DAAD19-99-1-0280

#### **Project Staff**

Dr. James G. Goodberlet, J. Todd Hastings, Mark K. Mondol, Feng Zhang, and Professor Henry I. Smith

Spatial-phase-locked electron-beam lithography (SPLEBL) promises to reduce pattern-placement errors in electron-beam-lithography systems to the nanometer level. Such high precision is essential for a variety of future applications. Currently, SPLEBL is the only approach capable of nanometer – level placement accuracy.

In SPLEBL, a low-level, periodic signal, derived from the interaction of the scanning e-beam with a fiducial grid on the substrate, is used to continuously track the position of the e-beam while patterns are being written. Any deviation of the beam from its intended location on the substrate is sensed, and corrections are fed back to the beam-control electronics to cancel errors in the beam's position. In this manner, the locations of patterns are directly registered to the fiducial grid on the substrate.

During this reporting period we have: (1) completed the development of a signal simulator, (2) produced a two-dimensional spatial-phase-locking algorithm, and (3) begun exploring new polymers for fabricating the fiducial grid. Additionally, minor progress has been made in assembling a table-top electron-beam test column, which will be used for future electron-beam dose-modulation experiments. Electron emission was obtained in the test column from a tungsten hairpin filament, and 40% dose modulation was observed during initial experiments. Presently, the column is being reconstructed to facilitate further experiments that will incorporate electron-optical lenses and beam-imaging equipment.

A numerical model was developed to simulate the scintillation signal derived from the interaction of the electron beam with the fiducial grid. This model incorporated parameters representative of the fabrication process for the scintillating fiducial grid, the noise in the electron-beam lithography system, and the electron-beam profile. Since the electron beam scans discretely over the substrate along X and Y axes, a two-dimensional image of the scintillating fiducial grid is acquired. The signal simulator generated the image shown in Fig. 2(a) for conditions corresponding to our experiment. An actual image recorded from our experiment is shown in Fig. 2(b). The real image shows more noise than expected and lower contrast. The additional noise is the result of random current spikes from our photodetector, and the reduced contrast is believed to be due to long-range scattered electrons. The model is being modified to include these effects. Once completed, the signal simulator will be used to test various spatial-phase-locking algorithms.

A two-dimensional spatial-phase-locking algorithm was successfully completed during the year. This algorithm processes an image like that shown in Fig. 2(b), to extract position, scale and rotation errors in the electron-beam lithography system. The image is acquired via a sparse-sampling process where  $512 \times 512$  discrete samples are taken over the entire e-beam field, i.e. the area in which patterns are to be written. The spatial period of these samples differs slightly from the period of the fiducial grid on the sample so that a spatial interference pattern, or moiré pattern, is recorded as the image. A careful analysis of the X and Y phases of the resulting moiré grid yields the necessary electron-beam position errors. The algorithm can detect position errors to 1 part in  $10^5$ , scale errors to 3 parts in  $10^5$ , and correct rotation errors to about 15 microradians for image qualities similar to that shown in Fig. 2(a). This algorithm has been used in a first two-dimensional demonstration of SPLEBL, and results from that experiment are currently being analyzed. Preliminary results indicate that the magnitude of placement errors is about 3% or less of the fiducial-grid period.

An effort began this year to improve the quality of the scintillating fiducial grid. Currently, a scintillating resist is used which was developed last year. In collaboration with Prof. Swager of the Chemistry department, we are attempting to identify scintillating polymers that can be used for fabricating the fiducial grid necessary for SPLEBL. There are several important criteria that the polymer must meet. It must provide an adequate scintillation signal, it must be easily applied and removed from the substrate, it must be easily patterned (ideally by an UV interference quenching process), and it must not damage easily when scanned with the electron beam. Eight polymers have been tested and one appears to meet most of the requirements. Further tests of this polymer and new polymers are required.

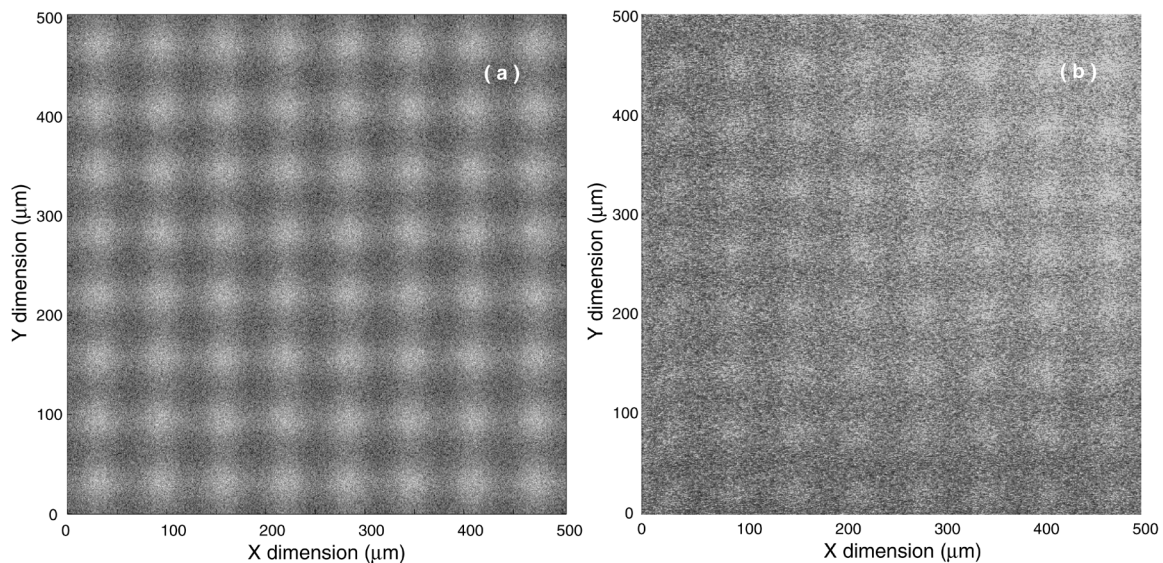


*Figure 2: (a) A simulated image of the fiducial grid, and (b) a real image of the fiducial grid. These images are processed with a two-dimensional spatial-phase-locking algorithm to determine electron-beam positioning errors. Once determined, corrections are fed back to the e-beam deflection control, so the patterns are written on the substrate with precise registration to the fiducial grid.*

## 4. X-Ray Nanolithography

### Sponsors

Defense Advanced Research Projects Agency/ U.S. Navy – Naval Air Systems Command,  
N00019-98-K-0110

### Project Staff

Dr. David C. Carter, James M. Daley, Michael H. Lim, Euclid E. Moon, and Professor Henry I. Smith

For several years, we have been developing the tools and methods of x-ray nanolithography. We have explored the theoretical and practical limitations, and endeavored to make its various components (*e.g.* mask-making, resists, electroplating, sources, alignment, etc.) reliable and “user-friendly.” Because of the critical importance of x-ray mask technology, we discuss this in a separate section.

Our sources for x-ray nanolithography are simple, low-cost electron-bombardment targets. We utilize the L line of copper at  $\lambda = 1.32$  nm. The sources are separated by a 1.5  $\mu\text{m}$ -thick  $\text{SiN}_x$  vacuum window from a helium-filled exposure chamber. In the future, we hope to replace the  $\text{Cu}_L$  sources with a higher-flux plasma-focus source.

In earlier research, we showed that for wavelengths longer than 0.8 nm, the important limit on resolution is diffraction in the gap between mask and substrate. With a  $\text{Cu}_L$  source, a 50 nm feature must be exposed at a mask-to-substrate gap of less than about 4  $\mu\text{m}$  in order to maintain good process latitude. A 25 nm feature would require a gap of 1  $\mu\text{m}$ . For very small features, we eliminate the gap and use contact between the substrate and the flexible membrane mask. This technique has enabled us to replicate features as small as 25 nm in a practical, reproducible way. Figure 3 shows scanning electron micrographs of device patterns with feature sizes less than 40 nm. The x-ray mask is shown on top and the lifted-off pattern is on the bottom.

To create the x-ray masks, the pattern is first written by electron-beam lithography onto an x-ray “mother” mask, using either our in-house e-beam system or a collaboration with the Naval Research Laboratory in Washington, DC. The e-beam written pattern is developed, and gold is electroplated into the resist mold. A negative replica, or “daughter” mask is created by exposing with the mother mask using soft-contact x-ray nanolithography. Finally, the daughter mask is exposed onto the device substrate.

Recent work has focused on investigating process latitude at these extremely fine feature sizes. Figure 4 shows how developed linewidth changes for up to 50% overdevelopment (*i.e.* developing for 50% longer than it takes for the feature to clear) as a function of linewidth. As can be seen from the plot, the measured feature on the substrate remains within a  $\pm 10\%$  process window (within the accuracy of the measurement) for isolated features as small as 30 nm and for dense features (greater than 1:3 line:space ratio) as small as 45 nm. This data indicates that soft-contact x-ray lithography is extremely robust and offers very wide process latitude.

## X-ray Mask

## X-ray Replication & Liftoff (Ti/Au)

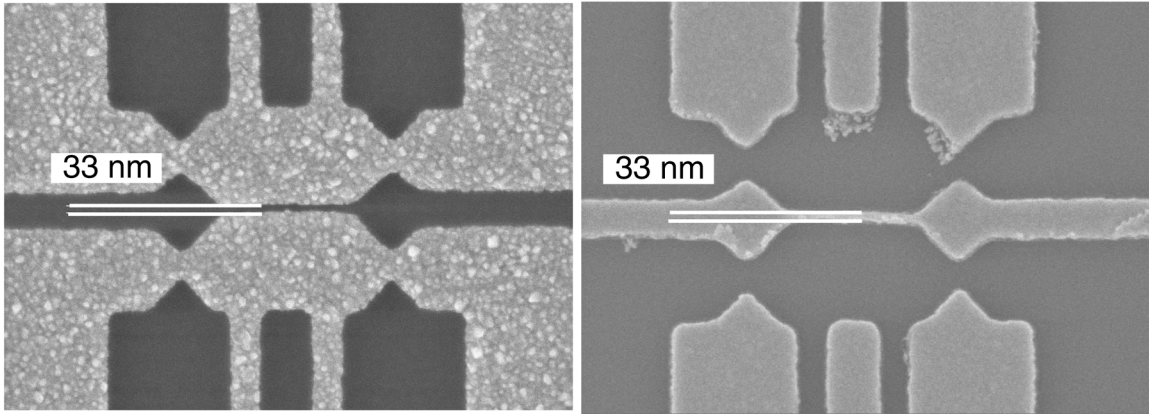


Figure 3. Scanning electron micrographs of device patterns with feature sizes less than 40 nm achieved by x-ray nanolithography followed by liftoff. The x-ray mask is shown at left and the lifted-off pattern is at right.

## Linewidth Change for 50% Overdevelopment

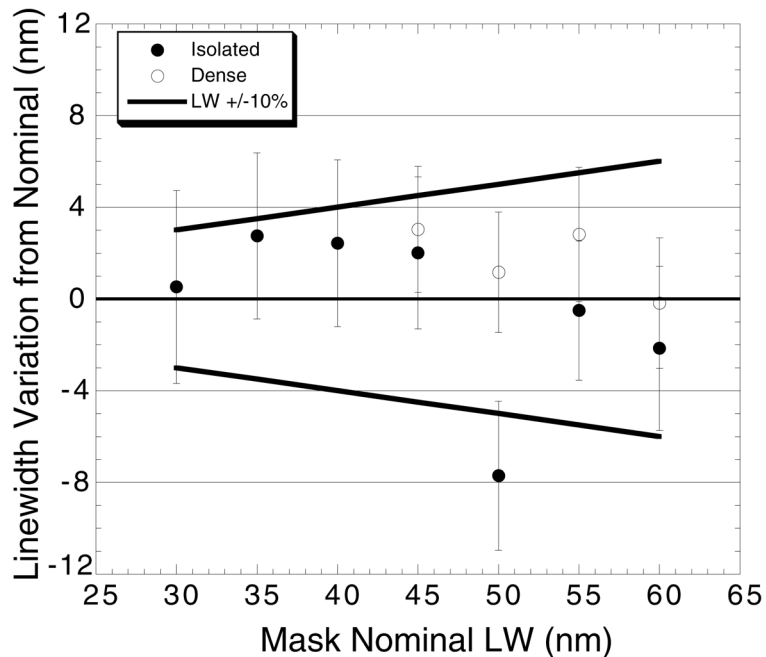


Figure 4. Plot of linewidth variation from nominal (i.e. developed for the time required to clear features) for up to 50% overdevelopment. Isolated features stay within a +/-10% process window for features as small as 30 nm. Dense (line:space ratio of 1:3 or greater) features remain in the process window for features as small as 45 nm.

## 5. Zone-Plate-Array Lithography (ZPAL)

### Sponsors

Defense Advanced Research Projects Agency; MDA972-97-1-000/  
Semiconductor Research Corporation; 96-LC-460 through  
U. C. Berkeley - SA1645-25508PG

### Project Staff

Dr. David J. D. Carter, Darío Gil, Rajesh Menon, and Professor Henry I. Smith

In semiconductor lithography, glass masks are illuminated with deep UV laser light and their image is reduced through a lens onto the substrate to define circuitry. As feature sizes are pushed toward 100 nm, lithography is becoming increasingly costly and difficult, and may soon limit the industry juggernaut.

At the MIT Nanostructures Laboratory, a considerably simpler approach is showing great promise. The new scheme, called zone-plate-array lithography (ZPAL) is made possible by inexpensive, high-speed computation and micromechanics. ZPAL replaces the "printing press" of traditional lithography with a technology more akin to that of a laser printer.

Instead of a single, massive lens, an array of hundreds of microfabricated Fresnel-zone-plate lenses is used, each focusing a beam of light onto the substrate. A computer-controlled array of micromechanical mirrors turns the light to each lens on or off as the stage is scanned under the array, thereby printing the desired pattern in a dot-matrix fashion. No mask is required, enabling designers to rapidly change circuit designs. A schematic of ZPAL is shown in Figure 5.

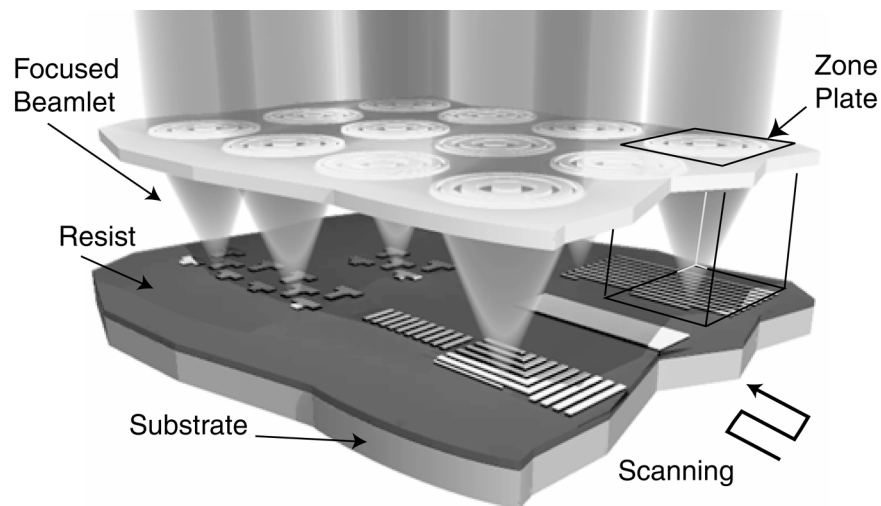


*Figure 5: Schematic of zone-plate-array lithography (ZPAL). An array of Fresnel zone plates focuses radiation beamlets onto a substrate. The individual beamlets are turned on and off by upstream micromechanics as the substrate is scanned under the array. In this way, patterns of arbitrary geometry can be created in a dot-matrix fashion. The minimum linewidth is equal to the minimum width of the outermost zone of the zone plates*

ZPAL leverages advances in nanofabrication, micromechanics, laser-controlled stages, and high-speed, low-cost computation to create a new form of lithography. We are developing ZPAL at UV, deep UV (DUV), EUV and x-ray wavelengths. Our experimental UV ZPAL system is currently operated at a wavelength of 442 nm. The system presently prints with an array of 9 zone plates, fabricated at MIT, in conjunction with a micromirror array made by Texas Instruments. Figure 6 shows an array of nine patterns exposed in parallel with this system.

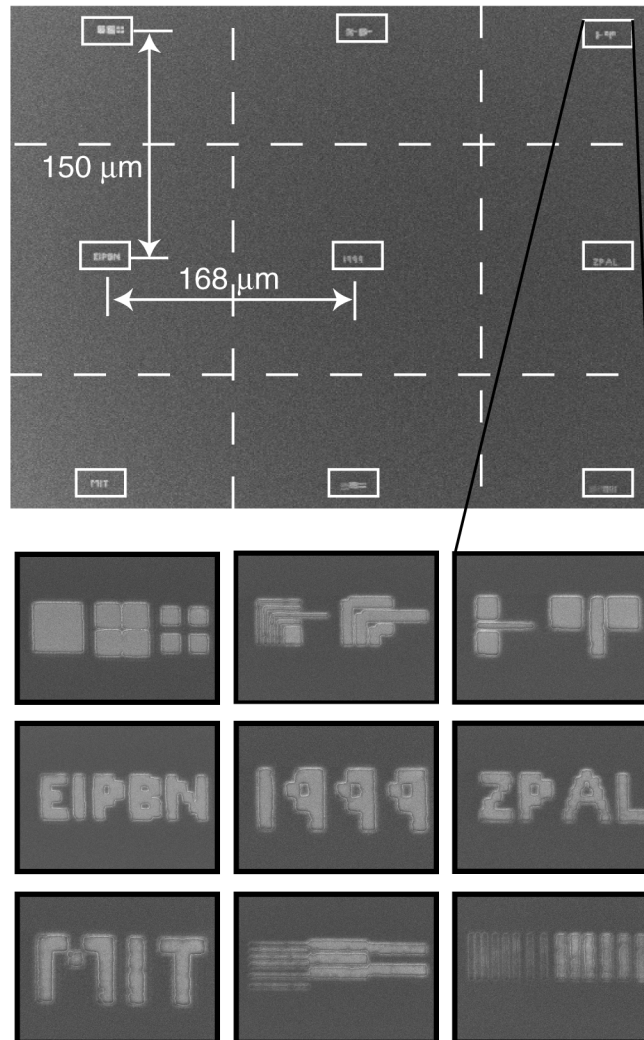
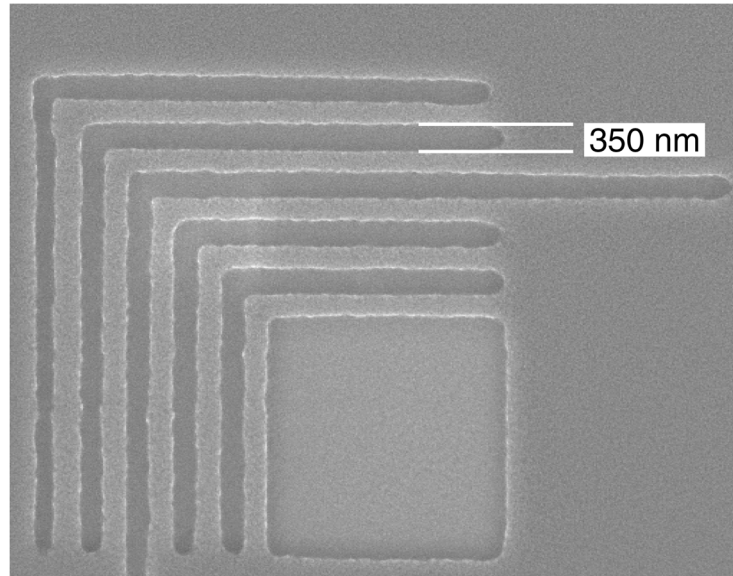


*Figure 6: Scanning-electron micrograph of nine different patterns exposed in parallel with a UV ZPAL system. A micromirror array, manufactured by Texas Instruments, was used to multiplex the laser light to each zone plate. As the wafer stage was scanned, the zone-plate illumination pattern was changed to write the patterns in a dot-matrix fashion.*

Figure 7 shows a closer view of a nested L pattern. The image quality is very good, showing dense 350 nm lines and spaces. Future research will push to lower wavelength (and therefore smaller feature size). For a DUV ZPAL system operating at  $\lambda=157$  nm, we expect to be able to produce 90 nm feature sizes.

# UV ZPAL Results

with  $\lambda = 442 \text{ nm}$



$$w_{\min} = k_1 \lambda / NA$$

- Demonstrated:  $k_1 = 0.53, NA = 0.67$
- Expect:  $k_1 = 0.45, NA = 0.75$

$$\lambda = 325 \text{ nm} \quad w_{\min} = 195 \text{ nm}$$

$$\lambda = 193 \text{ nm} \quad w_{\min} = 115 \text{ nm}$$

$$\lambda = 157 \text{ nm} \quad w_{\min} = 95 \text{ nm}$$

Extendibility – EUV or x-ray:  $w_{\min} = \sim 20 \text{ nm}$

*Figure 7: Scanning-electron micrograph of nested-L patterns produced with UV ( $\lambda=442\text{nm}$ ) ZPAL. The minimum feature size of an optical projection system can be described as  $w_{\min} = k_1 \lambda / NA$ . In this case the linewidth is 350 nm, the numerical aperture (NA) of the zone plates was 0.67, corresponding to a  $k_1$  factor of 0.55. With modest improvements to NA and  $k_1$ , and using DUV radiation ( $\lambda=157\text{nm}$ ). We expect to be able to print sub-100 nm features.*

Because zone plates are diffractive optical elements, ZPAL can operate at EUV wavelengths (13.4 nm) or even in the soft x-ray regime ( $\lambda \sim 1\text{-}5 \text{ nm}$ ). EUV or soft x-ray ZPAL should enable us to achieve feature sizes of about 20 nanometers at relatively low cost. We are developing a soft x-ray ZPAL system ( $\lambda=4.5 \text{ nm}$ ) to demonstrate the extendibility of ZPAL. Figure 8 shows a simulated pattern produced with such a system.

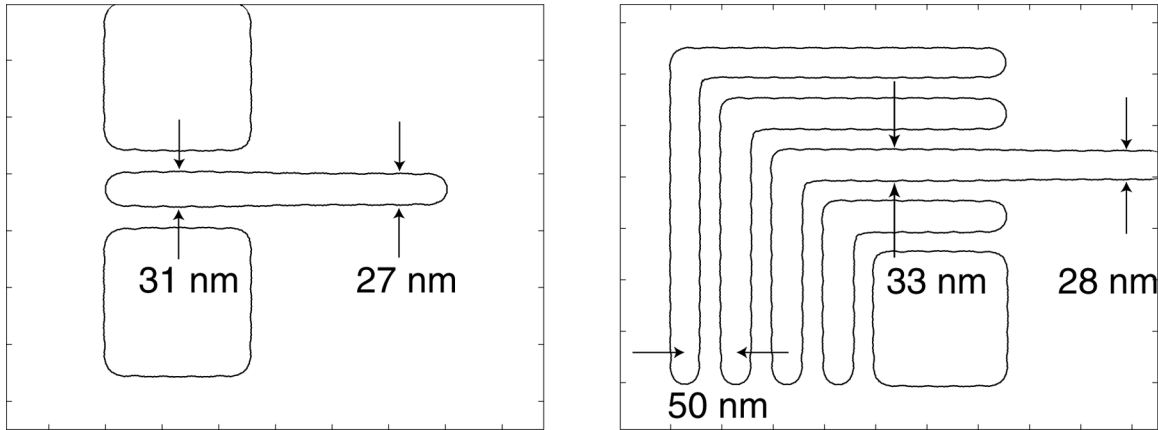


Figure 8: Simulated patterns assuming  $\lambda=4.5$  nm (from an electron-bombardment source) and an outer zone width of 25 nm. The slight proximity effect shown could be eliminated with a narrower-bandwidth source and/or by using an order-sorting aperture.

## 6. Improved Mask Technology for X-Ray Lithography

### Sponsors

Defense Advanced Research Projects Agency/Naval Air Systems Command  
Contract N00019-98-K-0110

### Project Staff

Michael H. Lim, James M. Daley, Juan Ferrera, Ken-ichi Murooka, Kevin P. Pipe, and Professor Henry I. Smith.

At feature sizes of 100 nm and below the mask-to-substrate gap in x-ray lithography,  $G$ , must be less than  $\sim 10$   $\mu\text{m}$ . Thus, for nanolithography the mask membrane should be considerably flatter than 1  $\mu\text{m}$ , preferably  $\sim 100$  nm. Our mask technology is based on low-stress, Si-rich silicon nitride,  $\text{SiN}_x$ . This material is produced in a vertical LPCVD reactor. Membranes of  $\text{SiN}_x$  can be cleaned and processed in conventional ways. For absorber patterns we electroplate gold onto the membrane, using a specially designed apparatus, after resist exposure and development. A Ti/Au plating base is deposited on the membrane prior to resist coating. To pattern periodic structures on the x-ray masks, we use interferometric lithography (IL), and for patterns of arbitrary geometry we use e-beam lithography. A high-resolution Leo SEM and a Digital Instruments STM/AFM are used to inspect x-ray masks for defects. Radiation hardness for  $\text{SiN}_x$  membranes remains a problem at dose levels corresponding to production (i.e., millions of exposures). For research purposes, however, the material is entirely acceptable. Currently we are investigating the problem of x-ray mask distortion, which is the most serious problem in x-ray lithography.

X-ray mask distortion is rooted in the flexibility of its membrane. The membrane responds to stress in the absorber patterns by flexing both in and out-of plane. Distortion caused by this motion, especially in-plane, must be overcome if x-ray lithography is to meet the overlay requirements of future electronics and optical devices. Thus far, the x-ray lithography community has attacked this problem by trying to achieve very low-stress absorbers and, when necessary, compensating for absorber induced stress by modifying the pattern written by the electron beam. We propose a new approach in which we first measure the membrane distortion and then correct it.

To measure distortion, we have developed a broadly applicable, nondestructive, global, membrane-distortion measurement technique called Holographic-Phase-Shifting Interferometry

(HPSI). The HPSI system is based on the interferometric lithography (IL) system we use to generate large-area, highly-coherent gratings. Figure 9 is a schematic of the IL apparatus, configured as a HPSI system. The IL system splits a laser beam ( $\lambda=351\text{nm}$ ) and forms two mutually coherent spherical waves, which interfere at the substrate at a half-angle  $\theta$ . The standing wave created at the substrate surface is used to expose photoresist. After development, the grating is present on the substrate surface or can be etched into it. The IL system is used as a holographic interferometer by mounting the IL-generated grating on the substrate platform, and placing a fluorescent screen in front of one of the spatial filters, as depicted in Figure 9. A fringe pattern appears on the screen, which is due to the superposition of two wave fronts: one reflected from the substrate surface and the other back-diffracted from the grating. If the grating has suffered no distortion between exposure and reinsertion, the reflected and back-diffracted beams will be identical and no fringes will be observed on the screen. Any in-plane distortion of the grating will result in a fringe pattern. A CCD camera is used to capture the fringes. To increase the precision, a phase-shifting measurement is implemented, by changing the phase of one of the arms and acquiring several images Fig. 10. In order to use this apparatus to measure the in-plane distortion, we etch shallow IL-generated gratings into the membrane.

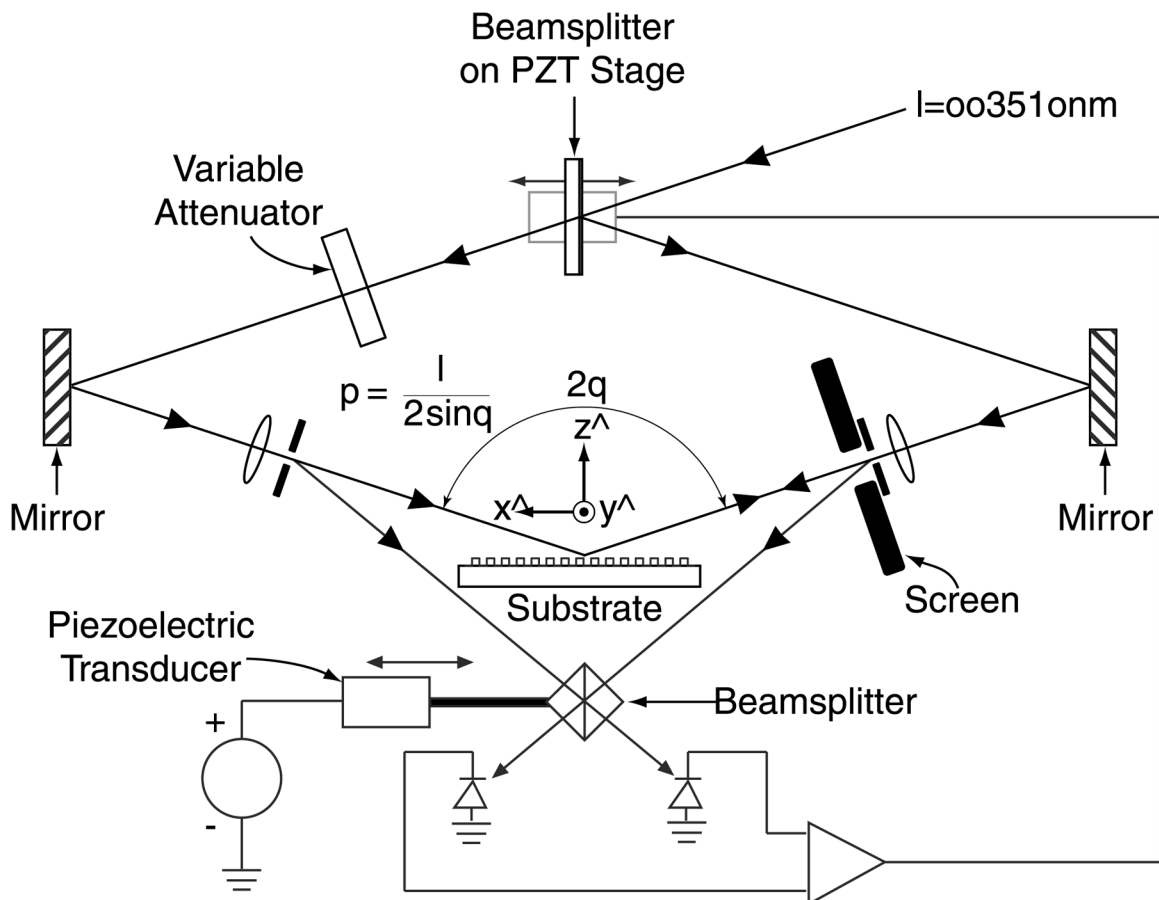


Figure 9: A schematic of the Holographic Phase-Shifting Interferometer (HPSI) based on the interferometric lithography system that we use to generate highly-coherent gratings.

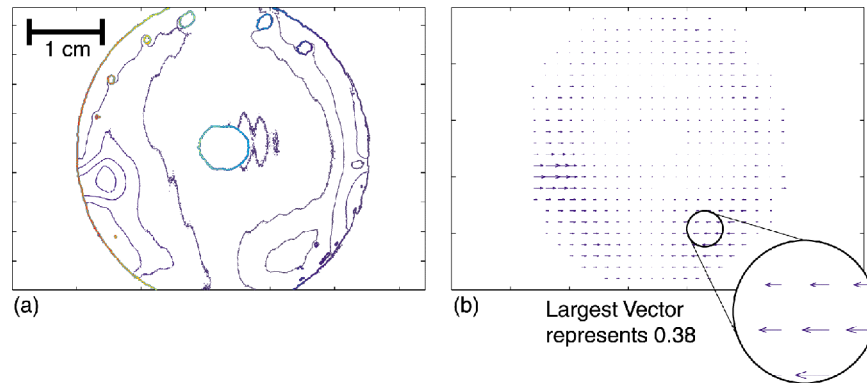


Figure 10: The HPSI uses diffractive metrology to make a rapid, global measurement of the distortion of a membrane. (a) Contour plot of phase distortion (nonlinear component) obtained by the HPSI. Successive contours are separated by  $\pi/2$  radians., (b) conversion of the phase map of (a) into a distortion map.

We have developed an analytical technique that predicts both in-plane distortion (IPD) and out-of-plane distortion (OPD) arising from arbitrary stress distributions in 2D. Moreover, we can also solve the inverse problem; *i.e.*, we can predict the stress distribution which, when applied to any existing distortion, eliminates it. The calculational techniques are based on the variational method. It is relatively straightforward to formulate the total energy due to membrane distortion, even for a very complicated stress distribution. We calculate the true distortion by minimizing the total membrane energy due to the placement of the stressed absorber; the total energy is straightforward to formulate for even complicated absorber distributions. Figure 11 shows the results of a calculation where half the SiNx membrane is covered with an absorber under tensile stress.

Following a suggestion by Feldman *et al*, a correcting stress distribution can be introduced by means of local heating. Figure 12 shows the analytical result of a 7.5 mm spot, with a 1°C elevation in temperature, centered on a 50 mm square SiNx membrane that is 1 μm thick. There is a peak displacement of 6.3 nm that occurs around the edges of the spot. This is equivalent to a circularly shaped absorber with 1.3 MPa of stress. The analysis indicates the time constant of the heating is less than one second. Moreover the calculational process also requires less than one second to complete.

We hope to build on this work by developing a system that can actively introduce a heat distribution into the x-ray mask in order to correct for membrane distortion in real-time. If successful, this should enable x-ray nanolithography to be used in applications such as integrated optics which demand the highest accuracy, precision and coherence in the placement of pattern elements.

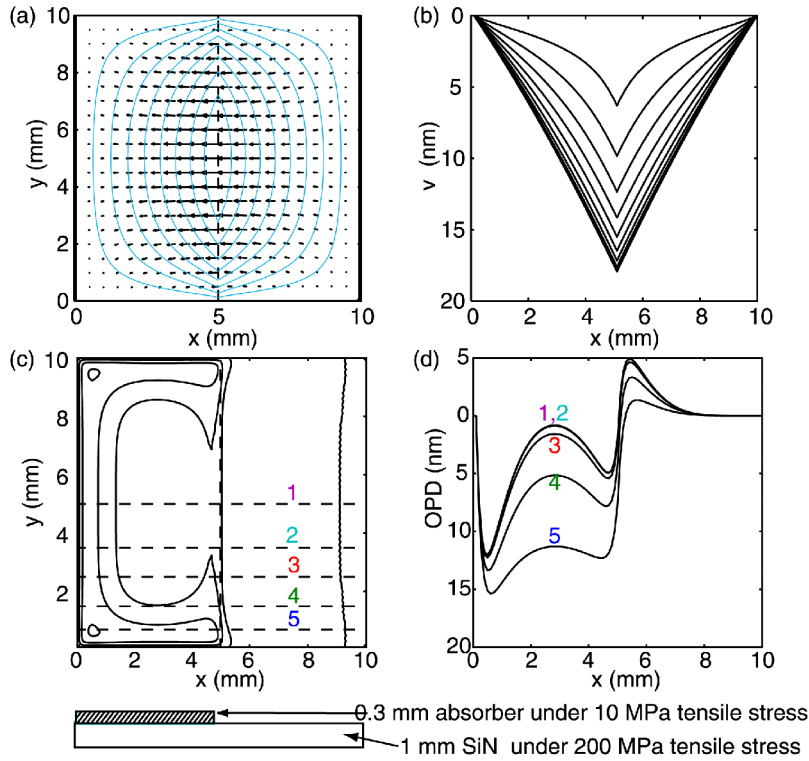


Figure 11: Our calculational technique can solve both in-plane and out-of plane membrane distortions in 2-dimensions. For example, covering half-plane of a 10 mm square SiNx membrane with an absorber results in both IPD and OPD displacements. (a) shows a 2-dimensional map of the IPD, which clearly indicates that a 1-D approximation would be inadequate. This is more clearly shown in (b), as the cross-sectional slices of the x component of the distortion along the x-axis vary as one moves closer to the boundary of the membrane. (c) and (d) show that the OPD also has a significant 2-D component.

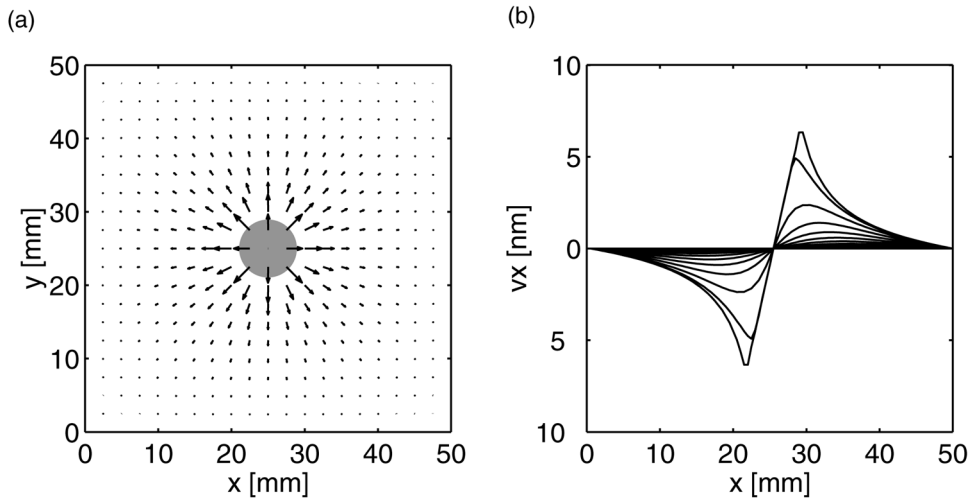


Figure 12: The calculated distortion of a 50 mm square SiN membrane, with a thickness of  $1 \mu\text{m}$ , in the presence of a 7.5 mm spot with  $1^\circ\text{C}$  rise in temperature. (a) The vector map showing the 2D distortion; (b) the cross-section of the x-component along the x-axis.

## 7. Nanometer-level Feedback-Stabilized Interferometric Aligning and Gapping X-ray Exposure System

### Sponsors

Naval Air System Command, N00019-98-K-0110

### Project Staff

Euclid E. Moon, Dr. Patrick N. Everett, and Professor Henry I. Smith

An experimental high-precision, x-ray exposure system has been constructed that employs Interferometric Broad-Band Imaging (IBBI) for alignment (Fig. 13(a)). The IBBI scheme utilizes grating and checkerboard type alignment marks on mask and substrate, respectively, which are viewed through the mask from outside the x-ray beam at a Littrow angle of 20 degrees with f/10 optics and a 110 mm working distance (Fig. 13(b)). Each mark consists of two gratings (or checkerboards) of slightly different periods,  $p_1$  and  $p_2$ , arranged so that  $p_1$  is superimposed over  $p_2$ , and  $p_2$  over  $p_1$  during alignment. Alignment is measured from two identical sets of moiré fringes, imaged onto a CCD, that move in opposite directions as the mask is moved relative to the substrate. Alignment is determined from the relative spatial phase of the two fringe sets, measured with a high-sensitivity frequency-domain algorithm.

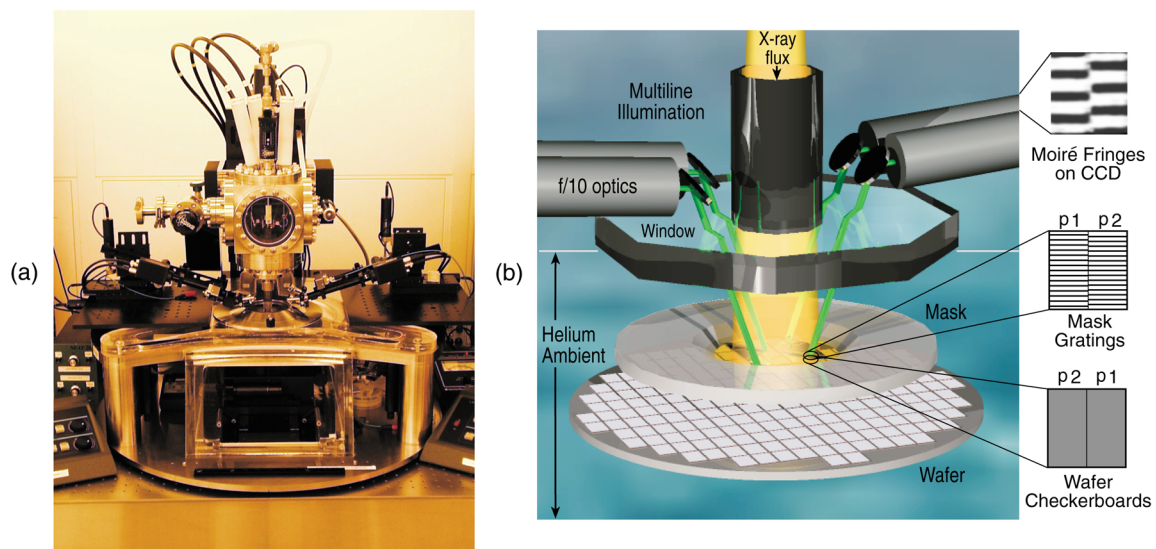


**Figure 13:** (a) X-ray exposure and alignment system. Mask and wafer are located in a helium ambient and exposed to x-rays. (b) Schematic of IBBI scheme which enables an alignment beam to enter at a 20 deg. angle through a viewport before and during exposure. Fringes result from interference between mask gratings and wafer checkerboards of similar periods. The fringes are imaged onto a CCD camera and analyzed in the frequency domain. The relative mask-wafer position is controlled by piezos with integral capacitive sensors.

It was discovered that the spatial phase of fringes from marks on the mask alone could be made sensitive to gap. Gap sensitivity is achieved by monotonically varying (i.e., chirping) the checkerboard period in the transverse direction, and maintaining a constant period in the viewing direction, Fig. 14(a). The fringes are produced from interference of beams diffracted over a range of angles by the chirped checkerboard, Fig. 14(b). The constant period (Fig. 14(c)) is selected to backdiffract this sweep of beams to the microscope after reflection from the substrate. We refer to this scheme as Transverse Chirp Gapping (TCG).

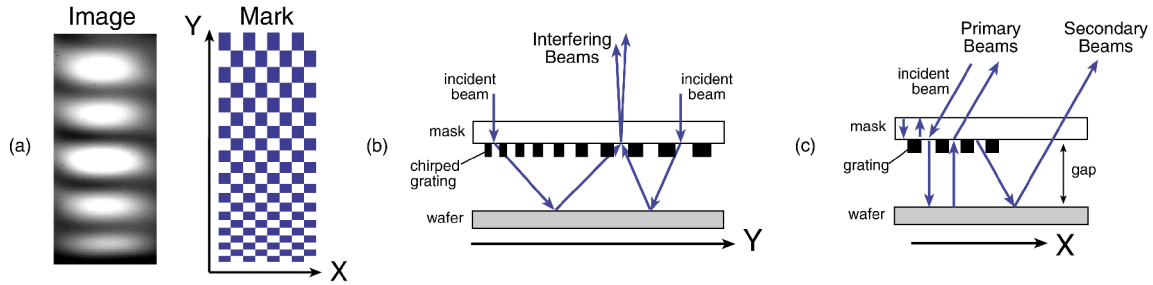


Figure 14: Transverse-Chirp-Gapping (TCG) scheme. The gapping mark on the mask is a checkerboard pattern with uniform period along  $X$  and a chirped period along  $Y$ . This gives rise to a fringe pattern, as shown. (a) Cross-sectional schematic along the  $Y$  direction, depicting the diffracted beams that produce the fringe pattern. (b) Cross-sectional schematic along the  $X$  direction, depicting diffracted beams that traverse the gap and the membrane, and are rediffracted back along the input direction. Also shown are the secondary beams, which traverse the gap a second time at an inclined angle.

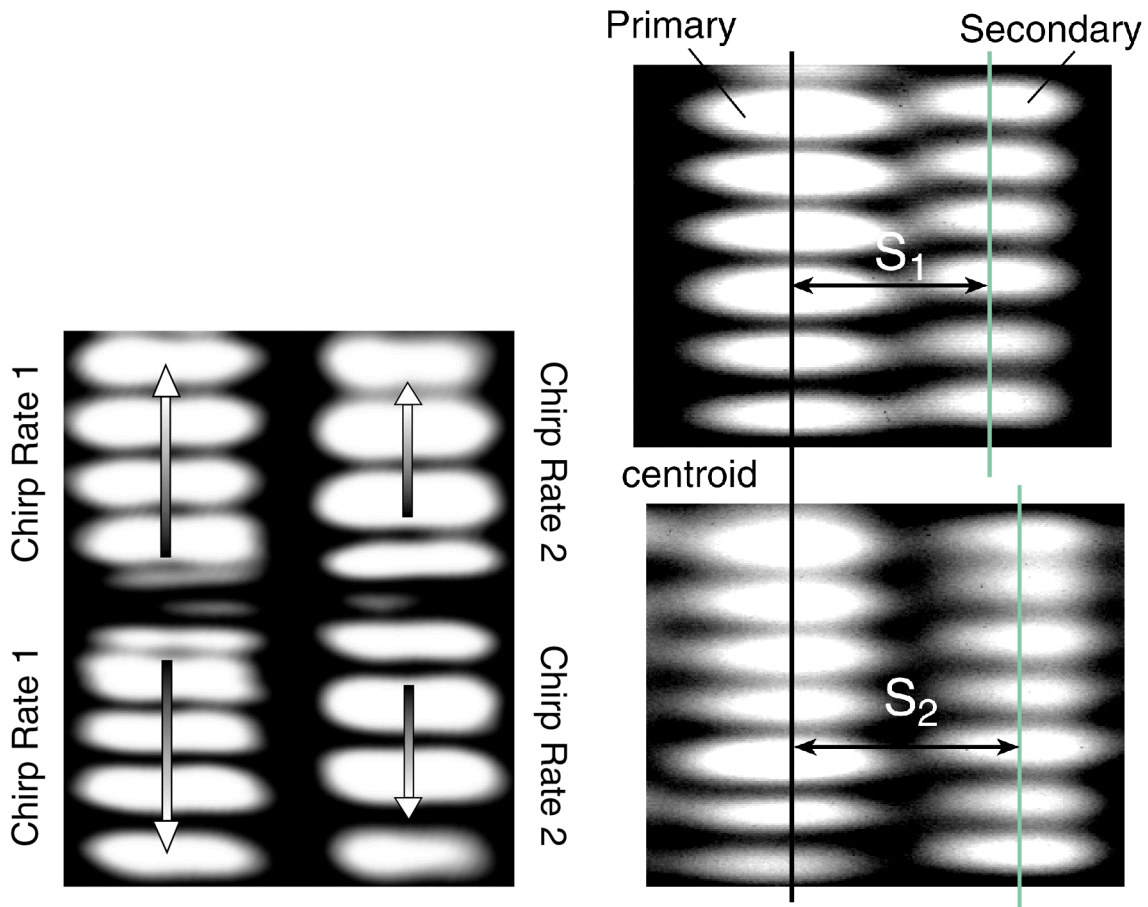
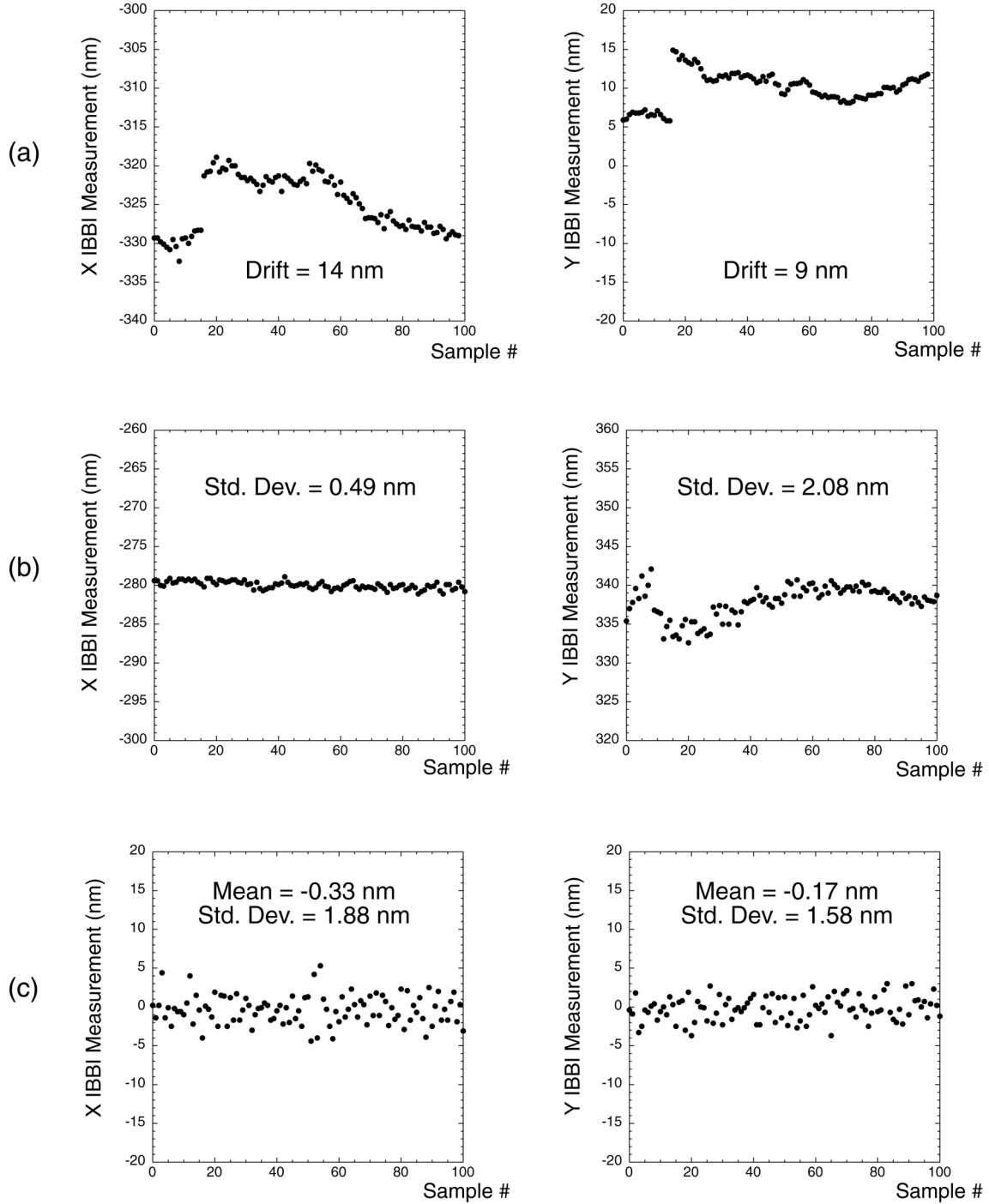


Figure 15 (left): Photograph of the fringe patterns from checkerboard marks having oppositely directed chirps and chirps of different rates.

Figure 16 (right): Photographs of the primary and secondary fringe sets at two different gaps greater than  $30\ \mu\text{m}$ . The schematic illustrating the origin of the secondary fringes is shown in Fig. 17(c).

The relative phase of two such TCG fringe sets is taken to determine the gap in a manner analogous to IBBI alignment. Since the phase of the gapping fringes goes through one cycle in less than 1 micron, the phase ambiguity over larger gap changes is resolved with a second pair of fringes which cycle at a different rate. The differential rate fringes, depicted in Fig. 15, permit unambiguous gapping over a range of gaps from 2 to 30 microns. The gap sensitivity is better than 50 nm.



1 Sample = 1.2 sec

Figure 17: Plots of IBBI measurements in X and Y for (a) no feedback, (b) no feedback, but mask studs resting on substrate, and (c) mask free of studs, with feedback.

Gaps larger than 30 microns are beyond the range required for x-ray lithography, but are useful for the safe approach of mask and wafer. For gaps from 30 to 400 microns we utilize the spatial separation of a primary and secondary set of fringes originating from the same TCG marks, as shown in Fig. 16. The fringe separation is linearly related to the gap. The primary set originates from the normal reflection of beams from the wafer surface and backdiffraction to the microscope. The secondary set arises from another set of beams, which forward diffract from the mask, and reflect off the wafer back to the microscope.

We are integrating TCG with IBBI in a three-dimensional feedback configuration. The ability of IBBI to control the X and Y position of the mask at the nanometer level is illustrated in Fig. 17.

The unique collection of capabilities of IBBI alignment and TCG gapping are being employed in the fabrication of a variety of electronic and optical devices, including 25 nm effective-channel-length n-MOS transistors.

## **8. Interference Lithography**

### **Sponsors**

Air Force Office of Scientific Research – F49620-96-1-0126  
U.S. Army Research Office – DAAD19-99-1-0280  
University of Wisconsin – R137605  
Naval Air System Command – N00019-98-K-0110  
National Science Foundation – DMR9871539

### **Project Staff**

James M. Carter, Maya Farhoud, Juan Ferrera, Robert C. Fleming, Ken-ichi Murooka, Timothy A. Savas, Michael Walsh, Dr. Mark L. Schattenburg, and Professor Henry I. Smith

Interference lithography is the preferred method for fabricating periodic and quasi-periodic patterns that must be spatially coherent over large areas. For spatial periods down to 200 nm, an argon ion laser is generally used in a Mach-Zehnder configuration, with a fringe-locking feedback system, as illustrated in Fig. 18. This scheme produces large area (10-cm-diameter) gratings with long-range spatial-phase coherence. Fringe locking ensures reproducibility of exposure.

During this year, a second, experimental interference-lithography system was assembled which uses the 325 nm line of a He Cd laser. Lithographic exposures are carried out both with a Lloyd's mirror configuration and one similar to that shown in Fig. 18. This system will soon be equipped with collimating lenses obtained by donation from Ultratech Corp.

The gratings and grids produced by interference lithography have found a wide range of applications. The Chandra x-ray astronomy satellite launched in August of 1999 included hundreds of matched, high-precision gratings. Other applications being pursued include: ultra-high-density magnetic information storage, atom-beam interferometry, and the use of interferometrically-produced grids as fiducials in spatial-phase-locked electron-beam lithography and in a new approach to metrology for the sub-100 nm domain. These applications are described elsewhere in this report.

For spatial periods of 100 nm, a source wavelength below 200 nm must be used. Since such sources have limited temporal coherence, one is forced to employ an achromatic scheme, as shown in Fig. 19. The source is an ArF laser (193 nm wavelength). A collimating lens, polarizer and scanning system are interposed between the source and the interferometer in order to achieve reasonable depth-of-focus and large exposure areas. We also use a white light interference principle to insure equal path lengths in the two interferometer arms. Using this system, gratings and grids of 100 nm period (nominally 50 nm lines or posts) are obtained in

PMMA on top of an antireflection coating. Fig.20 shows a 100 nm-period grid etched into Si following achromatic interferometric lithography. Grids of Si posts are being used to investigate photo-and electroluminescence which may result from charge-carrier quantum confinement.

To obtain spatial periods of 50 nm, a source wavelength below 100 nm and an achromatic scheme must be employed. We have established a collaboration with the University of Wisconsin, in which we will utilize an undulator light source (13 nm wavelength) incorporated on their synchrotron. An achromatic interferometer, currently being designed and built, will be capable of exposing 50-nm period gratings and grids in resist.

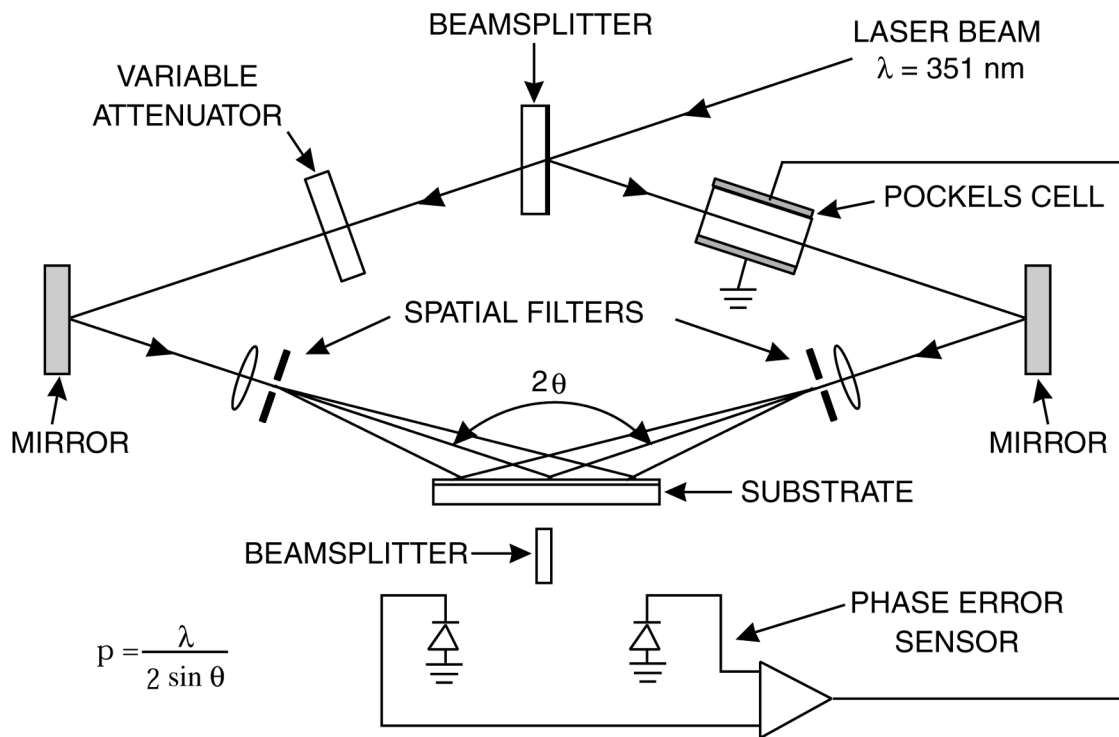


Figure 18. Schematic of the MIT interferometric lithography system. The system occupies a 2x3m optical bench in a class 100 clean environment. The beamsplitter directs portions of the two interfering spherical beams to photodiodes. A feedback locking is achieved by differentially amplifying the photodiode signals and applying a correction to the Pockels cell which phase shifts one of the beams.

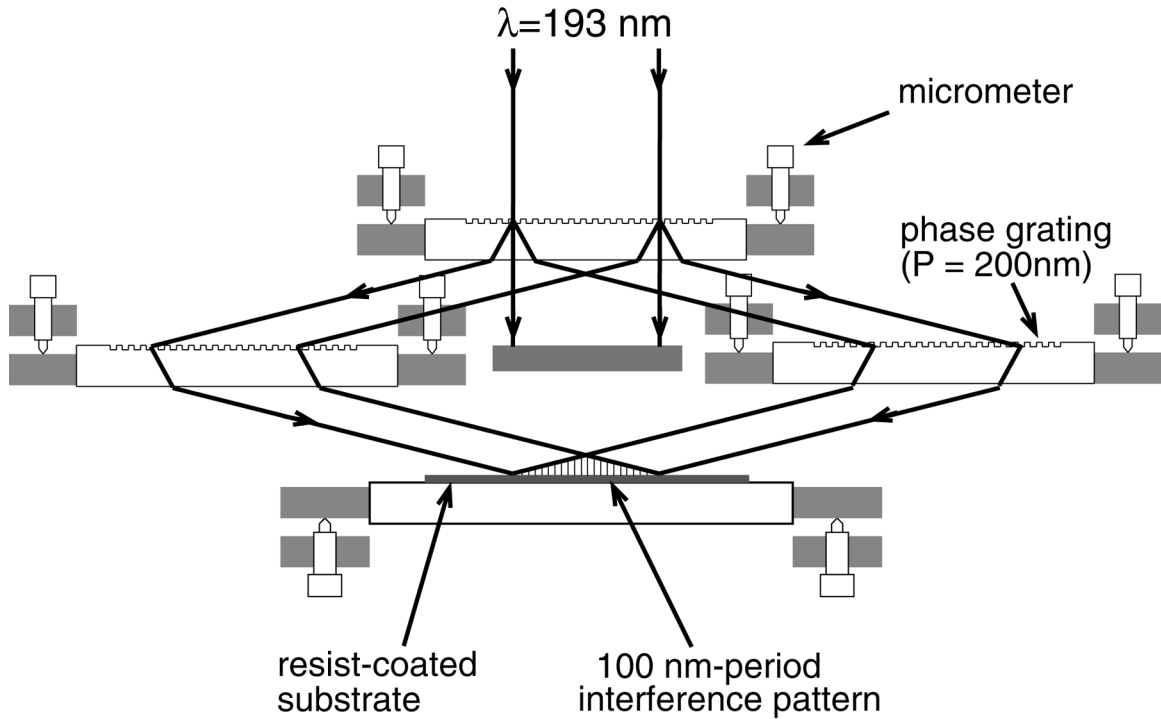
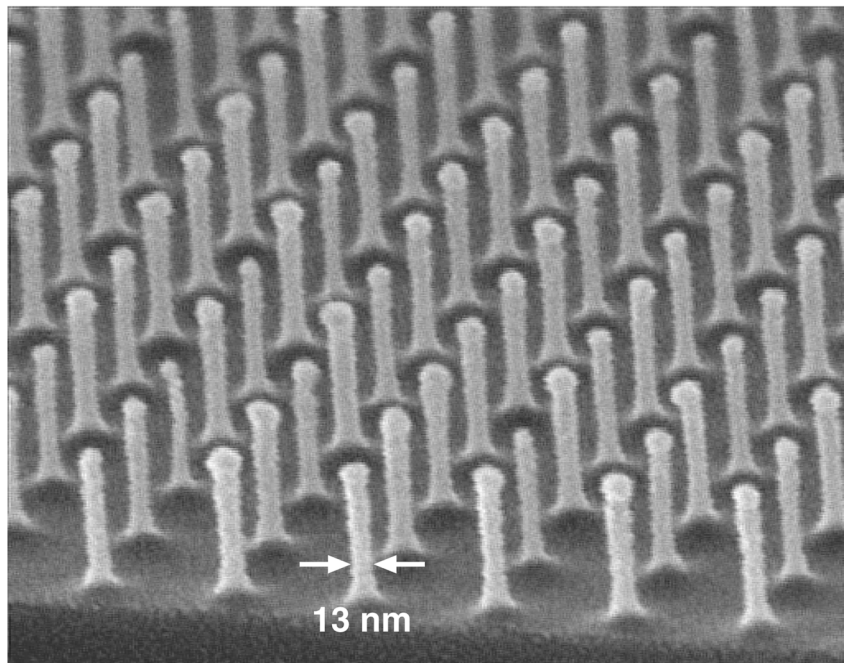


Figure 19. Achromatic interferometric lithography (AIL) configuration employed to produce 100 nm-period gratings and grids.



### 100nm-period posts in Si

Figure 20 Scanning electron micrograph of a 100 nm-period grid, exposed in PMMA on top of an antireflection coating, and transferred into Si by reactive ion etching.

## 9. Fabrication of Optical Sources in III-V Materials Using Photonic Crystals

### Sponsors

National Science Foundation - #DMR-9400334  
Army Research Office - #DAAG-55-98-1-0474  
Army Research Office - #DAAG55-98-1-0080

### Project Staff

Alexei A. Erchak, D. J Rippen, Dr. S. Fan, Dr. Gale Petrich, M. Mondol, Professor Erich P. Ippen, Professor John D. Joanopoulos, Professor Leslie A. Kolodziejski, and Professor Henry I. Smith

### A Two-Dimensional Photonic Band Gap Light-Emitting Diode

A photonic band gap (PBG) is the optical analog of an electronic band gap in a semiconductor. A periodic variation in the dielectric constant forbids certain photon energies within the PBG structure. Specifically, a two dimensional PBG inhibits the propagation of light within a certain range of frequencies in any direction in a plane. In this work, a two dimensional PBG is fabricated in the top cladding layer of an InGaP/InGaAs quantum well structure emitting at  $\lambda = 980$  nm. The photonic crystal is designed such that the emission wavelength lies inside the photonic band gap and hence does not couple to guided modes within the semiconductor. Coupling to the guided modes is a major source of loss in conventional light-emitting diodes. In the structure being fabricated, this problem is greatly reduced and the amount of light radiated from the device is enhanced.

The two-dimensional PBG LED consists of an InGaP/InGaAs active region, a low refractive index  $\text{Al}_x\text{O}_y$  spacer layer, and an  $\text{Al}_x\text{O}_y/\text{GaAs}$  distributed bragg reflector (DBR) with a wide stop band. The fabrication of the 2D PBG LED utilizes gas source molecular beam epitaxy, direct-write electron beam lithography, reactive-ion etching, and oxidation processes. Figure 21a shows a schematic of the structure. The 2-D photonic crystal consists of a triangular lattice of holes etched within the upper InGaP cladding layer with a hole-to-hole spacing of 315 nm, and a hole diameter of 220 nm (figure 21b). To minimize carrier recombination at the etched surfaces, the holes do not penetrate the InGaAs quantum well; however, the depth of the holes is sufficient to create a PBG (figure 21c). The active quantum well region lies on top of a DBR designed to reflect the 980 nm light; the spacer layer is used to minimize coupling to lateral guided modes in the DBR. Each 2-D PBG LED is a  $12.5 \mu\text{m} \times 12.5 \mu\text{m}$  region within the  $50 \mu\text{m} \times 50 \mu\text{m}$  LED mesa (figure 21d).

The device structure is grown using gas-source molecular beam epitaxy. The separation layer is initially grown as  $\text{Al}_{.98}\text{Ga}_{.02}\text{As}$  and the DBR consists of AlAs and GaAs layers. A  $\text{SiO}_2$  layer is deposited on the grown structure using plasma enhanced chemical vapor deposition. The holes are defined in PMMA by direct-write electron-beam lithography. The electron beam writes a square pattern in the PMMA to represent each hole. The beam size, however, is larger than the step size for translating the electron beam. This leads to the desired circular pattern following development.

The PMMA is used as a mask in transferring the hexagonal pattern to the  $\text{SiO}_2$  layer using RIE. This is accomplished by RIE with a  $\text{CHF}_3$  plasma using 15 second steps in between 1 minute cool-down steps, during which the electrode is back-cooled with He gas flow. The purpose of the cool-down step is to prevent flowing of the PMMA mask. The  $\text{SiO}_2$  mask is subsequently used in the RIE of the holes into the upper InGaP cladding layer using RIE with a  $\text{CH}_4/\text{H}_2$  plasma in a 1:4 gas flow ratio. The mesas are next defined using photolithography followed by RIE with a  $\text{BCl}_3/\text{SiCl}_4$  plasma in a 3:2 gas ratio. The final step in the device fabrication is the wet thermal oxidation of the  $\text{Al}_{.98}\text{Ga}_{.02}\text{As}$  separation layer and the AlAs DBR layers.

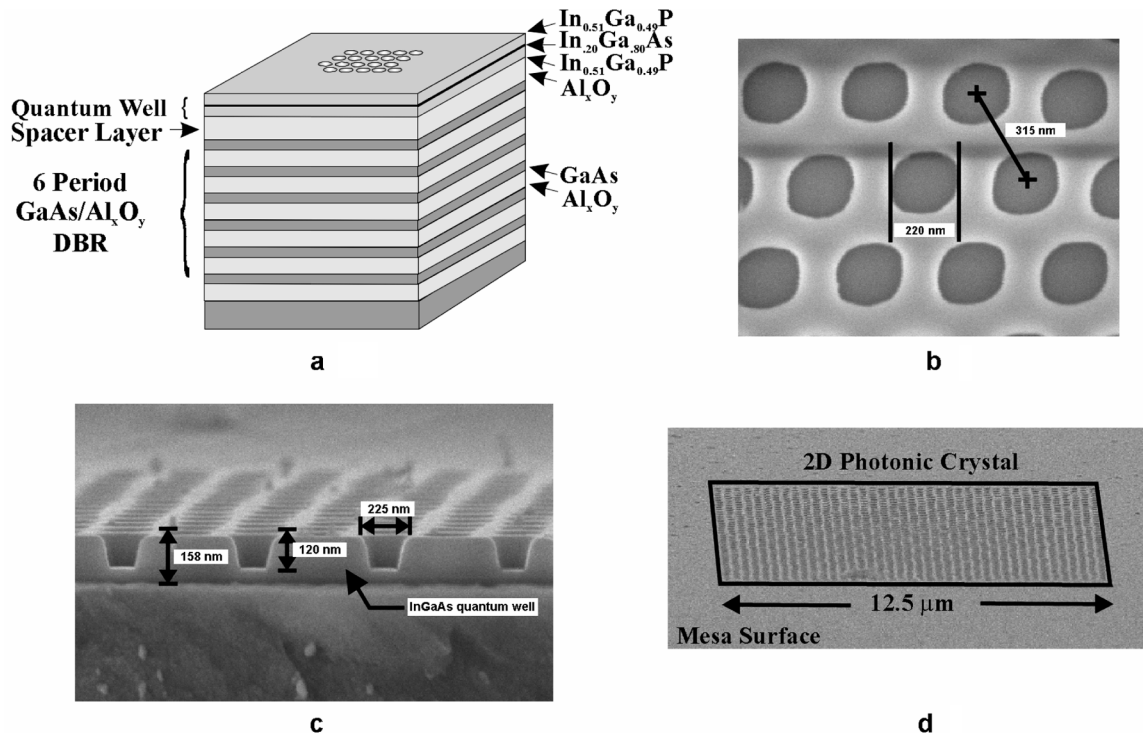


Fig 21. a) Schematic of 2-D PBG LED structure. The InGaP/InGaAs quantum well structure emits at  $\lambda = 980 \text{ nm}$ . The active region is separated from the DBR by a low refractive index  $\text{Al}_x\text{O}_y$  separation layer. A triangular lattice of holes in the top layer of the device eliminates coupling of emitted light to planar guided modes. b) An SEM micrograph showing the dimensions of the triangular array of holes forming the photonic crystal. c) Cross-sectional view of 2-D PBG LED structure. The holes do not penetrate the InGaAs quantum well to avoid surface recombination. d) SEM micrograph of the 2D photonic crystal.

### A Photonic Band Gap Microcavity Laser Embedded in a Strip Waveguide

A one-dimensional photonic crystal is fabricated within a strip waveguide to provide strong optical confinement and a small modal volume on the order of a half-cubic wavelength. The microcavity is formed by a defect in the one-dimensional periodic photonic crystal. Optical confinement is achieved in the lateral and vertical directions by a high refractive index contrast. A high-efficiency, low-threshold, microcavity laser results with light output coupling to the strip waveguide. The structure is designed to be integratable with other optoelectronic devices.

The one-dimensional PBG microcavity laser consists of an InGaP/InGaAs multiple quantum well active region emitting at  $\lambda=980 \text{ nm}$ , on top of a low refractive index  $\text{Al}_x\text{O}_y$  spacer layer. Figure 22a shows a schematic of the structure. The 1D photonic crystal consists of a periodic line of holes etched within the active region, with a hole-to-hole spacing of 256 nm and a hole diameter of 113 nm. The strip waveguide width is 320 nm and the waveguide depth is 112 nm. The length of the defect region is 426 nm. The active quantum well region lies on top of a low index spacer layer to separate the waveguide mode from the high index substrate. The laser output will occur on the side of the defect with the least number of holes.

The device structure is grown using gas-source molecular beam epitaxy. The separation layer is initially grown as  $\text{Al}_9\text{Ga}_1\text{As}$  and graded up to higher Al composition by dropping the Al cell temperature by  $20^\circ\text{C}$  and raising the Ga cell temperature by  $20^\circ\text{C}$  for 2 minutes. The composition is graded to stabilize the interface with the active region upon oxidation of the spacer layer. A  $\text{SiO}_2$  layer is deposited on the grown structure using plasma enhanced chemical vapor deposition. The holes and strip waveguide are defined in PMMA by direct-write electron-beam

lithography. The pattern is then reversed using a Ni liftoff process. The pattern is transferred from the Ni to the SiO<sub>2</sub> by RIE with a CHF<sub>3</sub> plasma. The Ni mask is then removed using a wet Ni etchant. Figure 22b shows an SEM micrograph of a portion of a fabricated SiO<sub>2</sub> etch mask.

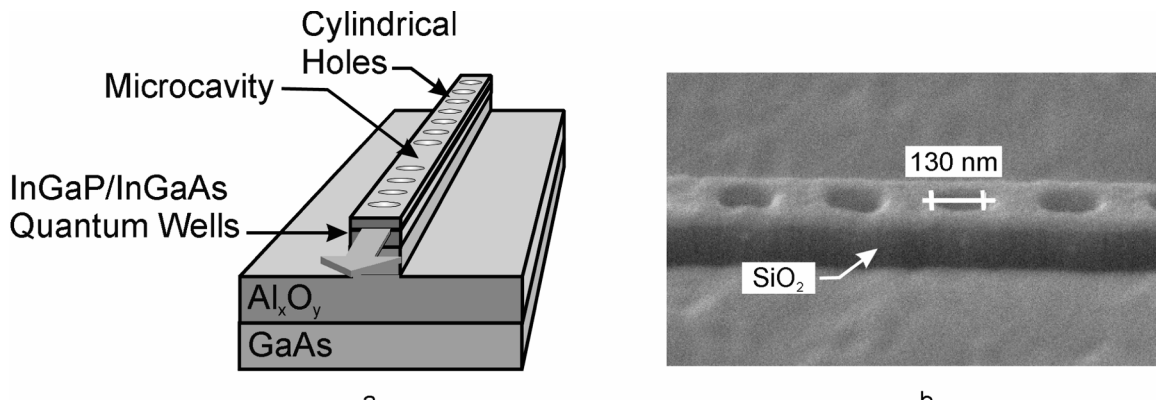


Fig 22. a) Schematic of 1-D PBG microcavity laser structure. The InGaP/InGaAs quantum well structure emits at  $\lambda = 980 \text{ nm}$ . The active region is separated from the GaAs substrate by a low refractive index Al<sub>x</sub>O<sub>y</sub> separation layer. The line of cylindrical holes forming the photonic crystal provide strong optical confinement along the waveguide while a high index contrast provides confinement in the lateral and vertical directions. b) An SEM micrograph showing an SiO<sub>2</sub> etch mask used in the RIE pattern transfer to the quantum well active region.

The SiO<sub>2</sub> mask will be used in the RIE of the holes into the InGaP/InGaAs active region using RIE with a CH<sub>4</sub>/H<sub>2</sub> plasma in a 1:4 gas flow ratio. The CH<sub>4</sub>/H<sub>2</sub> plasma etching slows at the Al<sub>0.9</sub>Ga<sub>0.1</sub>As spacer layer. RIE of the spacer layer will be accomplished using a BCl<sub>3</sub>/SiCl<sub>4</sub> plasma in a 3:2 gas ratio. The SiO<sub>2</sub> mask will then be removed by RIE with a CHF<sub>3</sub> plasma. The next step in the fabrication is the wet thermal oxidation of the Al<sub>0.9</sub>Ga<sub>0.1</sub>As separation layer. Finally, the device will be cleaved on the output side of the laser to allow for device testing.

## 10. Patterned Magnetic Materials for Data Storage

### Sponsors

National Science Foundation DMR9871539; IBM Graduate Fellowship

### Project Staff

Maya Farhoud, M. Abraham, Y. Hao, M. Hwang, Timothy Savas, Michael Walsh, Professor Caroline A. Ross, Professor Rajeev Ram, and Professor Henry I. Smith

As hard disk recording densities increase, the grain size of the magnetic layer is being reduced in order to maintain a good signal/noise ratio when reading data from the disk. However, if the grains become too small then a 'superparamagnetic' limit is reached in which the magnetization direction in the magnetic grains can be reversed by thermal energy, leading to loss of recorded data. One method for reducing media noise is to store data in periodic arrays of 'nanomagnets', lithographically defined magnetic particles, each of which has dimensions of less than 100 nm. Each particle is magnetised in one of two possible directions, representing a 1 or a 0.

We are using interferometric lithography in the NanoStructures Laboratory to produce arrays of nanomagnets of period 100 to 200nm. The particles are formed by electrodeposition, by evaporation and liftoff, or by etching of a previously deposited film, as shown in Fig. 23. We are exploring the switching mechanisms of the particles, the thermal stability of their magnetization, and interparticle interactions, and assessing their suitability for various data-storage schemes. In particular, we can investigate the collective behavior of the arrays using magnetometry (Fig. 24c),

and compare this with the behavior of individual particles using magnetic force microscopy (Fig. 24b) in order to understand how the behavior of one magnet is affected by its neighbors. We are also performing micromagnetic simulations to explore the mechanisms for magnetization reversal in these structures.

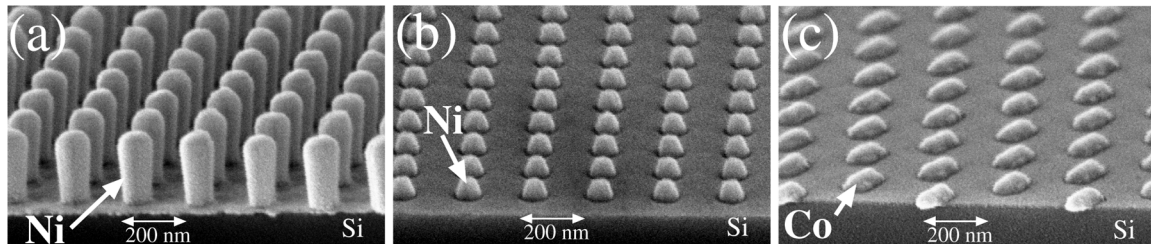


Fig. 23. Scanning electron micrographs of nanomagnet arrays fabricated by (a) electroplating, (b) evaporation and (c) lift-off. The posts in Fig 1a are 220 nm-tall nickel nanomagnets with a 90 nm diameter. In Fig. 1b, Ni nanomagnets were formed by evaporation and lift-off. Fig. 1c reveals elongated Co nanomagnets with an in-plane magnetic easy axis. These nanomagnets were formed by ion-milling a thin film of Co.

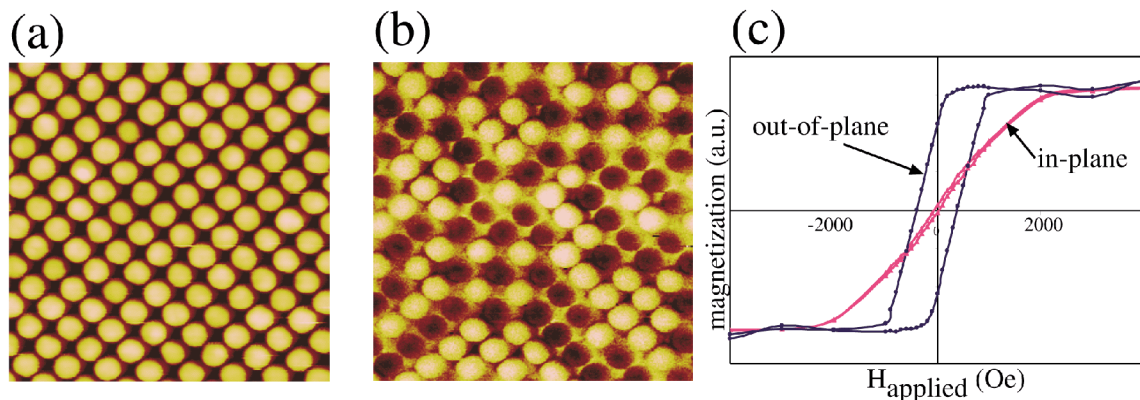


Fig. 24. Corresponding topographic (a) and magnetic (b) images of the array of electroplated Ni posts of Fig 1a. Dark circles in the magnetic image imply a particle magnetization pointing up and a light circle implies a magnetization pointing down. Up magnetization may be interpreted as a binary '1' and down magnetization as a binary '0'. In (c), the hysteresis loops of the same array of nanomagnets confirm that the sample's easy axis is perpendicular to the plane of the substrate.

## 11. Magnetic Random Access Memories (MRAMs)

### Sponsors

DARPA subcontract to MDA972-97-1-003 through University of New Orleans, National Science Foundation DMR9871539

### Project Staff

Michael Walsh, Y. Hao, Professor Caroline A. Ross, and Professor Henry I. Smith.

MRAMs are solid-state non-volatile magnetic storage devices in which each bit is stored on a small, elongated magnetoresistive sandwich element. A typical magnetoresistive (MR) sandwich consists of two magnetic layers of different coercivity, one hard and one soft, as shown in Figure 25. The direction of magnetization of the hard layer is used to represent the data bit. To write data, a magnetic field is applied by passing a current through a conductor line (word line) adjacent to the element, such that the field is large enough to change the magnetization of the hard layer. To read, a smaller current is passed, which can change the magnetization of the soft

layer only. The resistance of the element depends on whether the hard and soft layers are magnetized parallel or antiparallel, hence changes in the resistance resulting from the reversal of the soft layer can be used to probe the magnetic state of the hard layer. Elements are arranged in a rectangular array and connected with conductor lines, allowing individual elements to be selected. We have used interference lithography to produce arrays of spin-valve elements as illustrated in Fig. 26, made from Co/Cu/Co sandwich films, in order to investigate the behavior of these elements at sizes which are much smaller than those used in present-day MRAM devices. In the 175 nm long elements shown in Fig. 26, there is evidence of the two magnetic layers being antiferromagnetically coupled but switching separately. Future work will integrate these elements into an MRAM device. To fabricate such devices we will use electron-beam lithography to write x-ray masks, and then use x-ray lithography to transfer patterns to the substrate. Interferometric broad band imaging (IBBI) will be used to ensure precision alignment at the nanometer level. Because the MR sandwich layers cannot be etched by reactive-ion etching methods we will employ novel ion milling techniques that minimize redeposition effects.

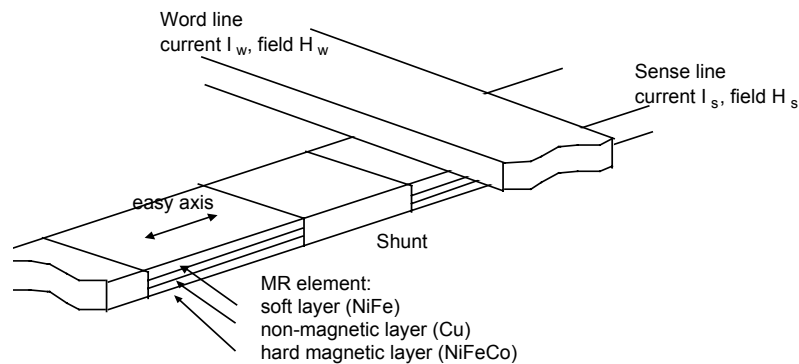


Figure 25: Schematic of MRAM structure, which consists of an array of parallel sense lines and parallel word lines. The MR elements are connected in series. Magnetic fields generated by currents passed simultaneously through a sense line and a word line write the element at the intersection of the two lines. To read, resistance changes in the sense line caused by a smaller wordline current are measured.

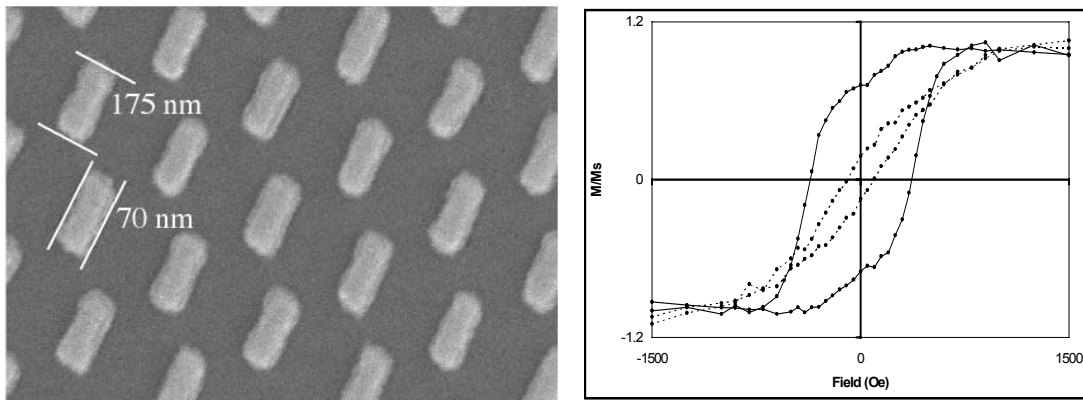


Figure 26. Micrograph of ion-milled ellipses of sputtered spin-valve films, 70 x 170 nm, made from a 5 nm Co/3 nm Cu/2 nm Co sandwich supplied by J. Wang, U. New Orleans. Right: Hysteresis loops parallel to long axis of ellipses (solid lines) and perpendicular (dotted lines)

## 12. 50 nm Low-Threshold-Voltage MOSFETs: Questions of Ultimate MOSFET Performance

### Sponsors

Navy – N66001-97-1-8909, DARPA, IBM, Intel, Intel Graduate Fellowship

### Project Staff

K. M. Jackson, Professor Dimitri A. Antoniadis and Professor Henry I. Smith

As MOSFETs in industry scale past the 0.1  $\mu\text{m}$  mark, questions of the ultimate limit of MOSFET performance continue to be debated. By examining devices in a little-explored design space and comparing the data to predictions from simulators and current metrics of performance, this project is investigating our ability to understand and predict the performance of MOSFETs in design spaces far from current devices.

The central goal of this project is to experimentally investigate the behavior of very low threshold voltage, 50 nm N&P MOSFETs at room and low temperatures. Significant effort is being put into designing and fabricating short channel MOSFETs that use novel processing techniques to push towards the limits of scaled devices. In the process, three specific issues are being addressed.

First, this work is examining the optimization of 50 nm  $L_{\text{eff}}$  devices for low-temperature operation. Specifically, the issues of doping profile design and the role of temperature scaling in the overall scaling of MOSFETs are being investigated through simulations and measurements of fabricated devices.

Second, a variety of processing approaches to fabricating devices with sub 100 mV threshold voltages and good electrostatic integrity are being implemented. Significant processing challenges exist in the creation of abrupt halos that create lateral non-uniformity in the channel doping, and in the control of the source and drain depths. Inverse modeling will be used to extract doping profiles from the fabricated devices, allowing a comparison of simulations to device data.

Third, these fabricated devices will be used to analyze the limits that carrier transport may place on the ultimate MOSFET performance. Two major viewpoints, a drift-diffusion approach or a scattering theory approach, suggest intrinsic current drive limits coming from either the mobility in the channel or the injection of carriers over the source barrier. Measurements of these very low threshold voltage devices at lower temperatures and across the range of halo dopings used, will provide data to examine the validity of these theories at very short channels.

Current efforts on this project are focused on fabricating a set of devices. Significant progress has been made on developing the process modules. Capacitors with 20 Å gate oxides have been fabricated and show well behaved capacitance-voltage characteristics. In addition, well behaved 100-150nm deep source and drain diodes have been fabricated with a 1050 °C spike anneal for both NMOS and PMOS devices.

One of the biggest challenges in the fabrication of these devices is to create profiles of dopants that change abruptly on the nanometer scale. Creating low  $V_{\text{th}}$  devices that have controlled short-channel effects requires both shallow source and drain junctions, as well as halos, which add dopants around the source and drain, but leave the rest of the channel with much fewer dopants. To achieve these halos, this work is using a combination of very reduced thermal budgets and unconventional dopants, including indium and carbon. Detailed simulations of implants and annealing cycles using UT-TOMCAT and TSUPREM4 have been performed to design the halos for the current devices.

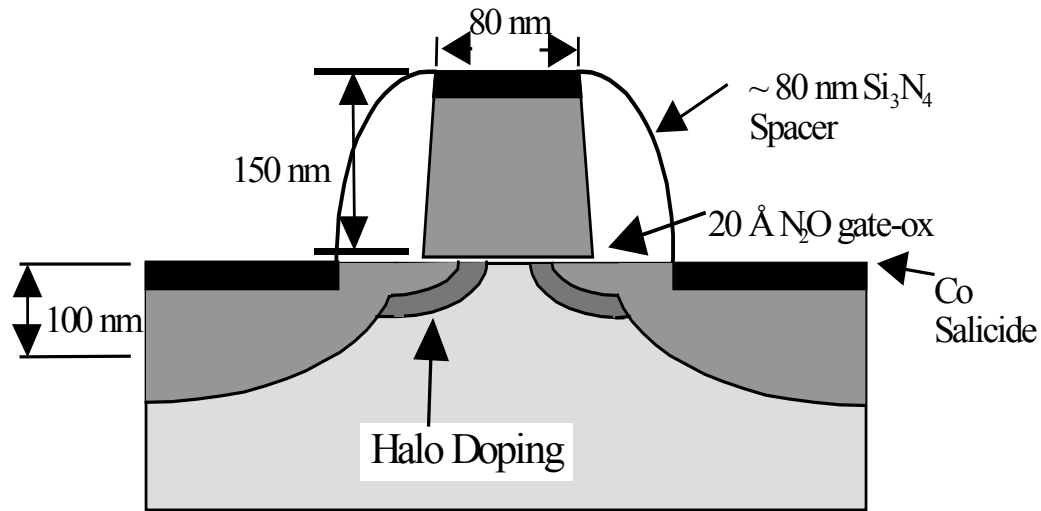


Figure 27: Schematic of  $L_{\text{eff}} = 50 \text{ nm}$  MOSFET

### 13 CMOS Technology for 25 nm Channel Length

#### Sponsors

NAVY SPARWAR  
Contract Number 66001-97-1-8909

#### Project Staff

Anthony Lochtefeld, Mitchell Meinhold and Thomas Langdo, Professor Dimitri. A. Antoniadis, Professor Henry I. Smith and Professor Eugene A. Fitzgerald

The double-gate (DG) MOSFET (Fig. 28) is considered a promising device for CMOS scaling to deep sub-100 nm gate lengths. However, realization of the ideal DG-MOS structure involves significant technological challenges: formation and alignment of gates above and below a thin single-crystalline silicon layer, and achieving low source/drain resistance for this thin layer. We are addressing these issues through integration of three primary technologies: wafer bonding with pre-patterned features, interferometric alignment, and selective epitaxy.

Monte-Carlo modeling predicts that double-gated devices that are scaled to  $L_{\text{eff}} = 25 \text{ nm}$  will have transconductances  $G_m$  in excess of 2000 mS/ $\mu\text{m}$ , while maintaining almost perfect sub-threshold slope. However, models also predict that the tolerance in aligning front and back gates has to be within  $L_g/4$  in order to avoid performance deterioration due to overlap capacitance. The  $L_g/4$  requirement translates into 6 nm alignment tolerance for a 25 nm channel. In order to meet this alignment challenge we will use the IBBI (Interferometric Broad-Band Imaging) alignment technique which achieves sub-nanometer misalignment detectivity. The planar double-gate devices will be fabricated starting with a SIMOX wafer. First the gate stack for the back-gate will be deposited and patterned by x-ray lithography. The structure will then be covered by a layer of CVD oxide, planarized, and bonded to a "handle wafer". The bulk of the SIMOX wafer will then be chemically etched using the back-oxide of the SIMOX wafer as the etch-stop. The fabrication will then follow a conventional SOI (Silicon on Insulator) process, with front gate precisely aligned to back-gate layer using the IBBI alignment scheme. The final structure is depicted in Fig. 28.

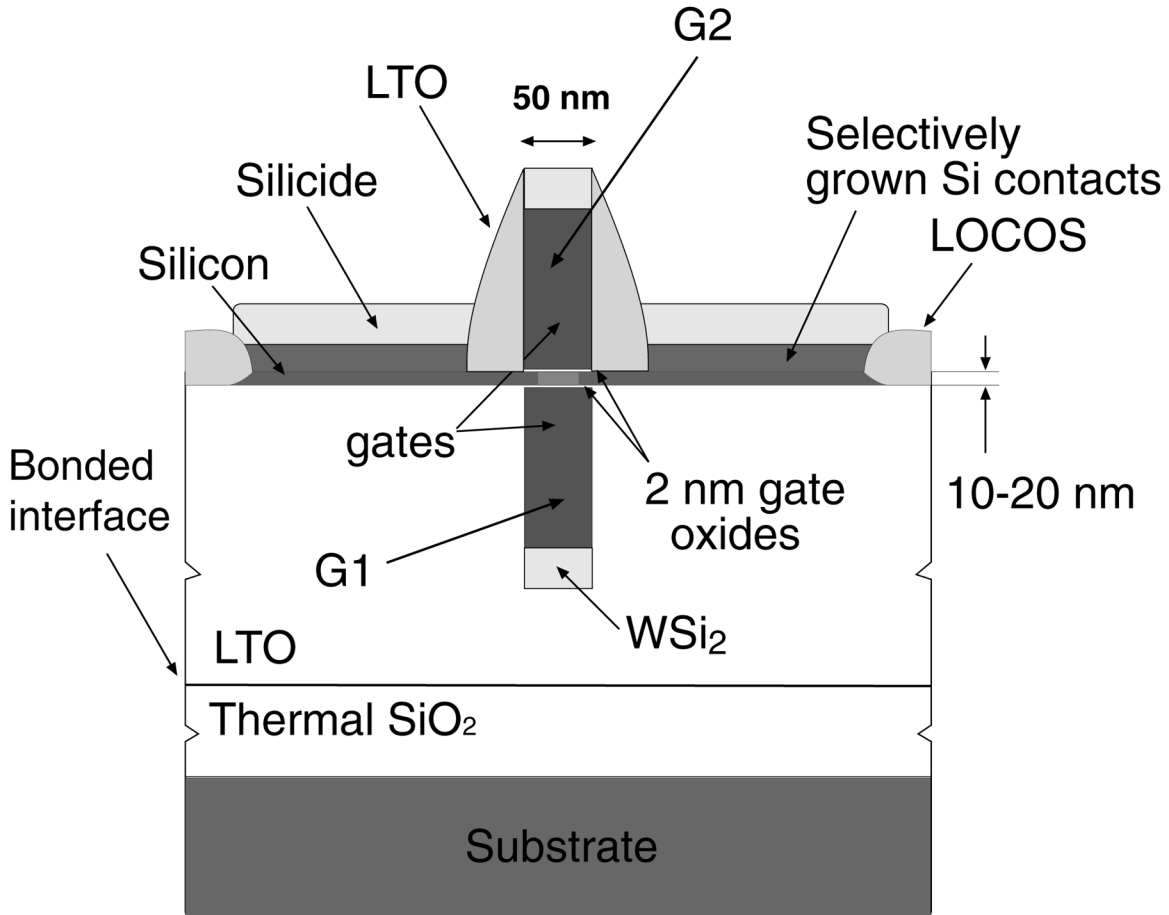


Figure 28: Double-gate (DG) NMOS transistor with 25 nm effective channel length. Gate-to-gate alignment is via x-ray lithography and interferometric-broad-band imaging (IBBI).

We employ a direct alignment approach to form top-gates with correct relative placement to the bottom-gates. We have demonstrated the functionality of this alignment system, used to process a number of device wafers. Fig. 29 shows a DG-MOS device after top-gate x-ray lithography, with buried n+ poly gate visible beneath a 25 nm silicon layer. Although we have attained alignment detectivity on the order of several nanometers, final alignment results are equally a function of precise pattern placement between the upper-and lower-gate x-ray masks. We are now developing a process to obtain this precision through close proximity x-ray mask replication. In this scheme, gate patterns from the upper-gate mask are transferred to the lower-gate mask using x-ray lithography. This is done while the alignment marks of the two masks are aligned. Lithography of this sort is challenging primarily for two reasons: 1) the resist image on the replicated mask must be inverse to that of the source mask, 2) it is necessary to maintain sub-100 nm resolution. We are working with new negative resists in order to develop a bi-layer resist process compatible with these constraints.

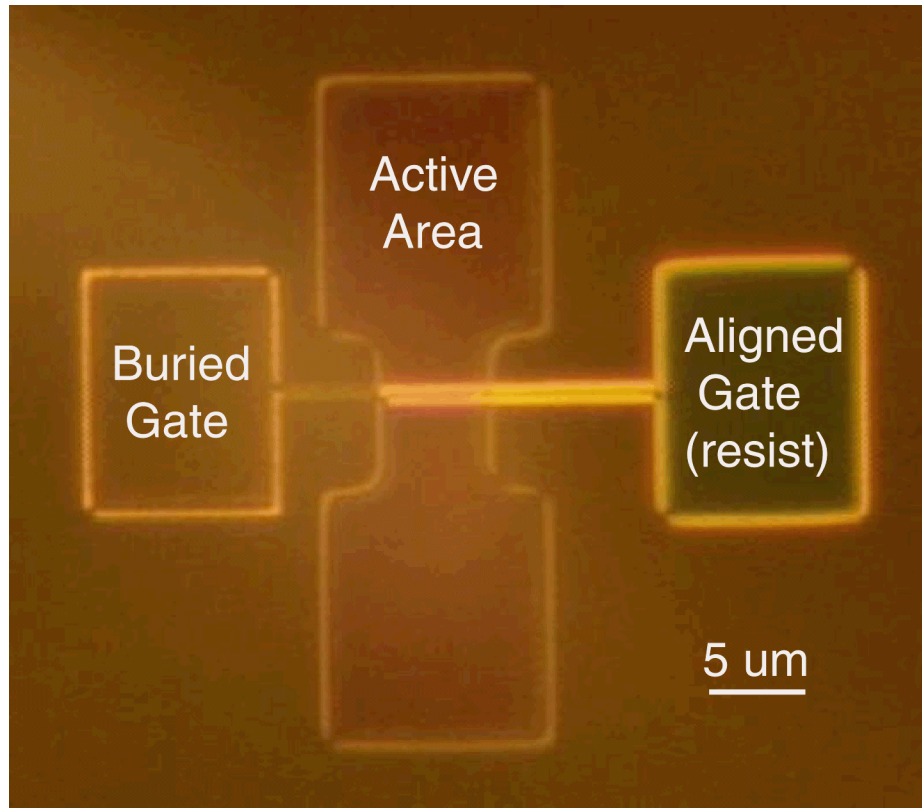


Figure 29: DG-NMOS device after top-gate x-ray lithography. Alignment of gates is via IBBI.

For ultimate scalability, the silicon channel must be of the order of 10-15 nm thick—too thin for silicidation of source/drain regions. We employ selective epitaxy to thicken the source and drain by ~50 nm, allowing easy silicidation and low series resistance. A TEM image (Fig. 30) of a raised source/drain test shows selective growth, without the undesirable faceting at the LTO/Si interface that typically occurs during selective growth. Selectivity is easier to achieve with LTO spacers, versus traditional Si<sub>3</sub>N<sub>4</sub>-on-LTO spacers. A current focus is integration of LTO spacers into our thin-film SOI -MOS process.

We are also investigating performance of deeply scaled DG vs. bulk MOS. It has been projected that with aggressive channel dopant profile engineering, bulk may scale down to ~25 nm  $L_{eff}$ <sup>1</sup>, which may be near the practical DG-MOS limit. However, to achieve this the bulk MOSFET must have very heavy (~1e19 cm<sup>-3</sup>) peak body doping to suppress punch-through, which results in a very high transverse electric field at the inversion layer. According to the well-verified universal mobility relationship, this should result in a low-field effective NMOS mobility approximately one-quarter of that for a DG-MOS device, for which the thin silicon channel and gate oxides allow deep scaling without significant body doping (Fig. 31). Although modern devices operate in or near the velocity saturation regime, models that account for non-local transport effects predict significant benefits for superior low-field mobility. This relation—between low-field mobility and high-field transport—has not been thoroughly explored experimentally. This is one of our goals in fabricating short MOS devices with thin undoped films.

<sup>1</sup> Y. Taur, et.al., IEDM Tech Dig. 1998, p.789

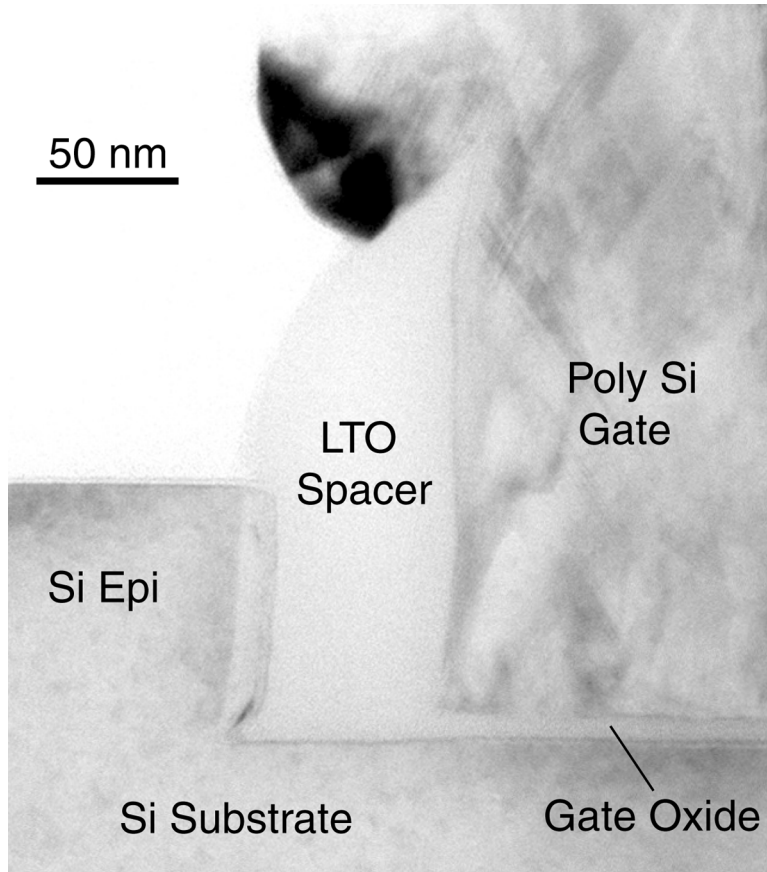


Figure 30: TEM image of a raised source/drain test, on bulk Si

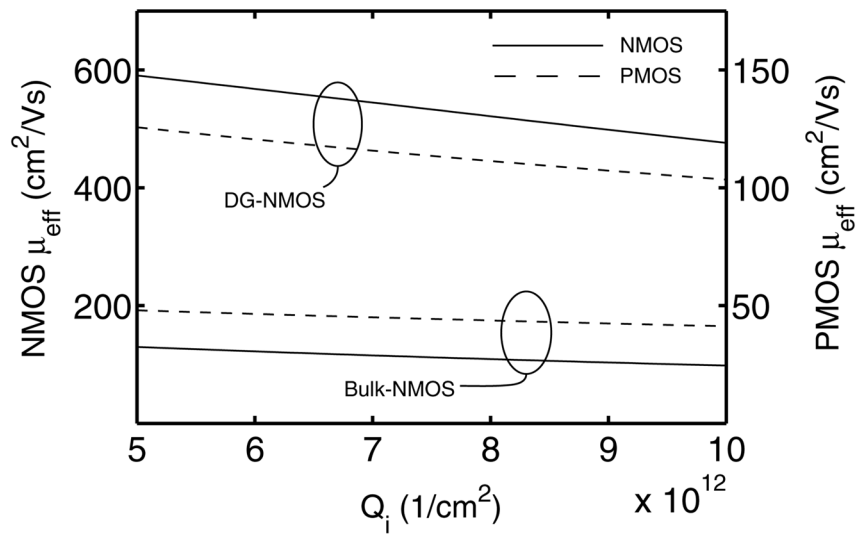


Figure 31: Low-field effective MOSFET mobility advantage predicted for deeply scaled DG- vs. bulk MOSFETs, based on the universal mobility dependence on transverse field. For bulk MOS, uniform body doping of  $5e18 \text{ cm}^{-3}$  is assumed. Shown for range of inversion layer densities ( $Q_i$ ) of interest in modern and future MOSFETs.

## 14. Deep-Ultraviolet Contact Photolithography

### Sponsor

Defense Advanced Research Projects Agency/NCCOSC Navy Grant N66001-98-1-8921

### Project Staff

Dr. James G. Goodberlet, James M. Daley, Mark K. Mondol and Professor Henry I. Smith

Deep-ultraviolet contact photolithography (DUVCP) is in its second year of development at MIT. The goal of this project is to demonstrate a lithography process capable of patterning sub-100-nm features at high rates ( $> 3 \text{ cm}^2/\text{sec}$ ) on spherical surfaces (radius of curvature as low as 8 cm). The lithography scheme must also be amenable to precise multilevel alignment, i.e. subsequently patterned levels must be aligned to previous levels to within a small fraction of the minimum feature size. A successful lithography scheme meeting these criteria will be used to fabricate a smart, wide-field-of-view camera. This camera will have detectors and high-speed signal-processing hardware on its curved focal plane. DUVCP best fulfills these demanding requirements.

Contact photolithography enables simple patterning with a 1x, absorber-on-glass, optical mask which is brought into intimate contact with a resist-coated substrate, and subsequently exposed. The process for DUVCP is similar, except that the mask is very thin, i.e.  $< 150 \mu\text{m}$  thick, and a tri-layer resist stack is used on the substrate. The thin mask assures truly intimate contact between the mask and substrate, and the thin resist minimizes deleterious diffraction effects of the transmitted image. An additional modification has been made to the mask design: the absorber has been embedded into the mask substrate. By embedding the absorber, the patterning resolution is improved. The practical resolution limit for pattern replication using DUVCP has been found to be  $\kappa \frac{\lambda}{2}$ , where the value of  $\kappa$  depends upon materials used for the embedded-amplitude mask (EAM) and resist properties, but is in the range of 0.6 to 0.8.<sup>2</sup> An illustration of the EAM and a scanning-electron micrograph of the embedded absorber are shown in Figure 32.

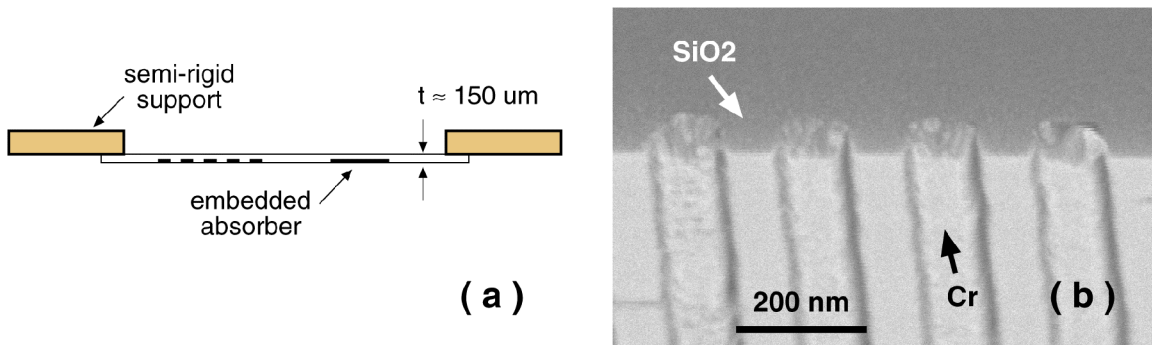


Figure 32: (a) The embedded-amplitude mask consists of a DUV-transparent, 150- $\mu\text{m}$ -thick substrate bonded to a semi-rigid plastic annulus for improved durability and handling. In the drawing, the thickness of the mask's substrate has been exaggerated to depict the embedded absorber. (b) An example of the embedded, patterned chrome absorber is shown in this scanning-electron micrograph.

Several experiments were carried out to evaluate the resolution, process latitude repeatability, robustness, and pattern-placement precision of DUVCP. The SEM images of Figure 33 highlight

<sup>2</sup> James G. Goodberlet, "Patterning 100-nm features using deep-ultraviolet contact photolithography", accepted for publication in Appl. Phys. Lett., Vol. 76, No. 6 (2000).

the results of these patterning experiments. These chrome-on-silicon features were created using a deep-ultraviolet contact exposure (220-nm wavelength, Hg(Xe) arc lamp source), resist development, reactive-ion etching of a tri-layer resist stack, and a chrome lift-off. The pitch of the nested L's, Fig. 33(a) and grating, Fig. 33(d) are 200 nm. In addition, uniform isolated lines (not shown) with widths down to 100 nm have been patterned with broad exposure latitude:  $\pm 18\%$  dose latitude for  $\pm 9\%$  linewidth control at 116 nm. The 140-nm-wide lines beside the 19- $\mu\text{m}$ -wide box, Fig. 33(c) shows that large and small features can be patterned simultaneously. Excellent reproducibility was observed for the finest nested-L patterns, which were patterned on different days with different batches of substrates. Reliable, sub-100-nm-resolution pattern transfer is possible with DUVCP.

An experiment was carried out to evaluate the magnitude of in-plane pattern-placement errors which might result from the thin mask and the contact-printing process. To evaluate these errors, two successive prints were made on one substrate, i.e. a double exposure. Between prints, the mask was removed, cleaned and realigned to the substrate. After the second exposure, the patterns, each a 5 x 5 array of crosses on 3.3 mm spacing, were transferred to the substrate with the standard processing steps. The position of each cross was then measured using the laser-interferometer stage of an electron-beam-lithography system, and the positions for each array compared to determine the extent of pattern-placement errors. The average placement error was measure to be about 60 nm, however this was the measurement uncertainty of the EBL system. The true placement errors are expected to be much smaller, and further experiments are being carried out to determine more accurately the placement uncertainty.

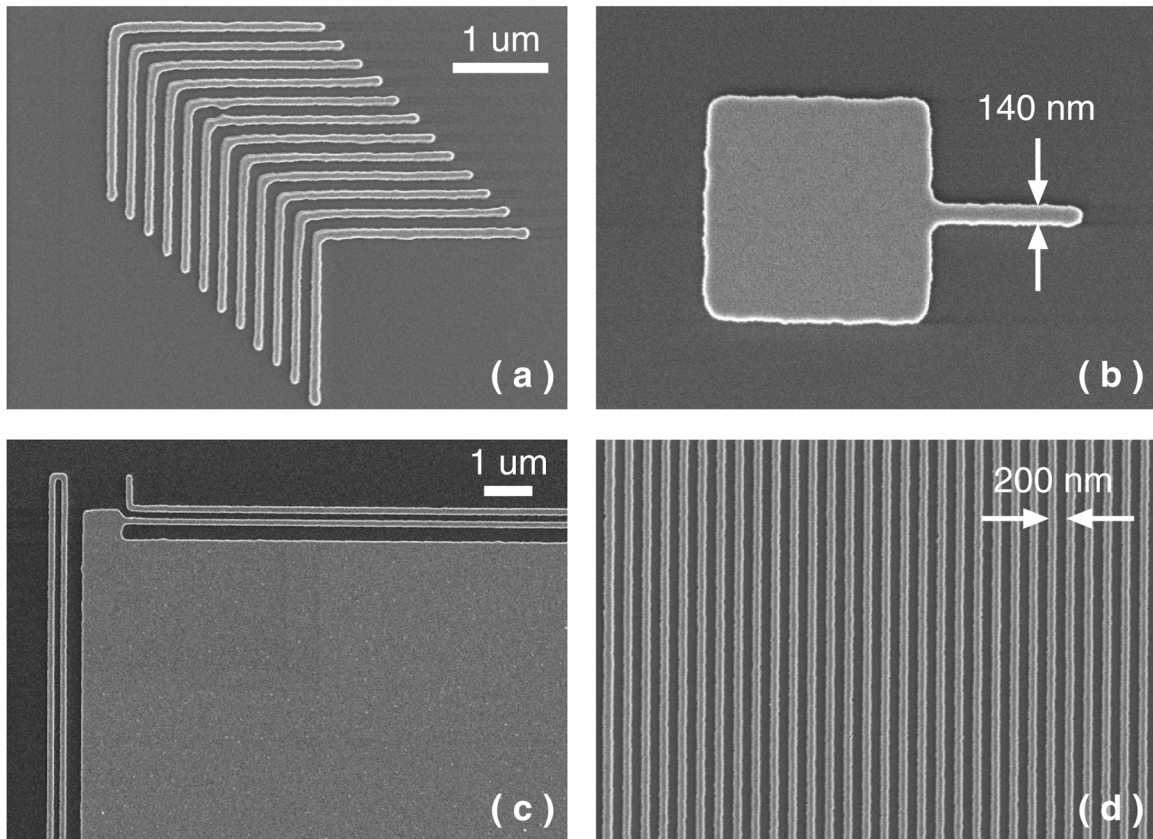


*Figure 33: These patterns were all fabricated using deep-ultraviolet contact photolithography. The chrome-on-silicon patterns include (a) 77-nm-wide nested L's on 200-nm pitch, (b) a pad-and-gate structure with 140-nm gate length, (c) coarse-and-fine features patterned simultaneously, and (d) a 200-nm-pitch grating.*

The next objective for DUVCP is to demonstrate precise multilevel alignment. Presently, a contact nanoaligner is being developed. This aligner will position the EAM precisely over the substrate before contact is made. Advanced mask-to-substrate alignment marks will be used to achieve sub-20-nm positioning accuracy. The aligner has been designed to print on flat or curved substrates using a range of mask sizes.

## 15. Fabrication of 3-D Photonic Bandgap Structures

### Sponsors

National Science Foundation  
Contract DMR-9808941

### Project Staff

Minghao Qi, J. Joannopoulos, Professor Henry I. Smith

Photonic Bandgap Structures (PBG) offer opportunities for miniaturizing a variety of conventional optical devices. 3-D PBG structures have advantage over 2-D structures in that they eliminate the loss of light through substrates or air. Fig. 34 illustrates the 3D structure we are attempting to fabricate using planar fabrication techniques. Modeling indicates that it has a large, complete bandgap. Our fabrication process allows defects to be introduced in a controlled manner.

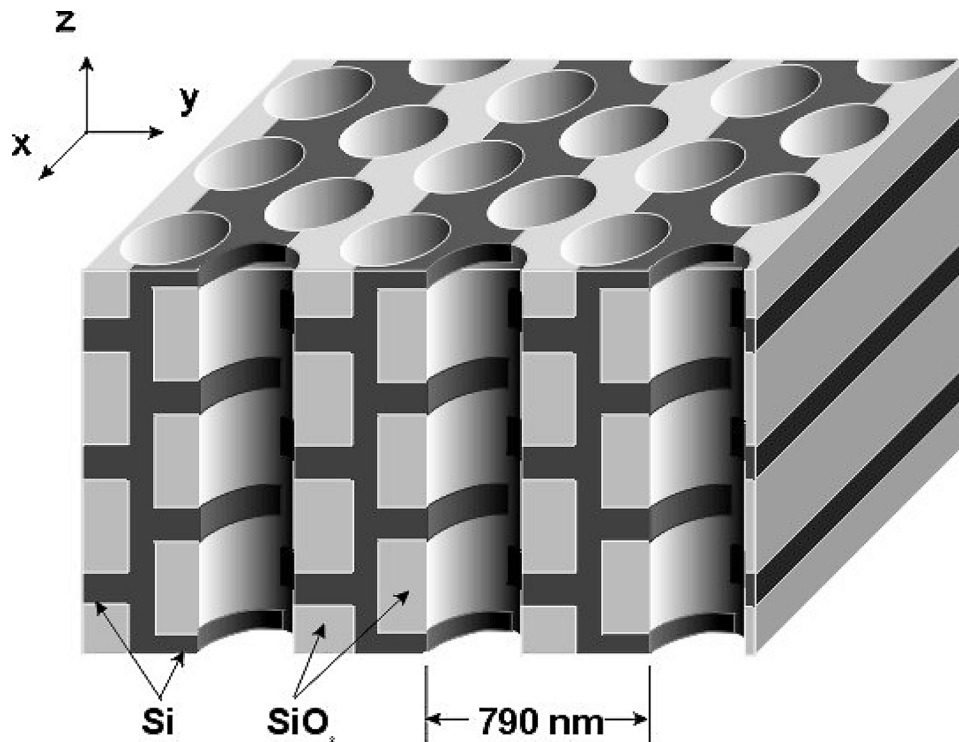


Figure 34. Depiction of a 3D photonic-bandgap (PBG) crystal to be fabricated at a 790 nm period. The dark gray and light gray regions correspond to Si, with a high index (3.4), and SiO<sub>2</sub>, with low index (1.4), respectively. The SiO<sub>2</sub> can be removed after the structure is formed, and that will increase the ideal bandgap from 14% to 21 % of the midgap frequency, which corresponds to a wavelength of 1.53  $\mu$ m. The design enables planar fabrication techniques to be applied.

In last year's report we showed successful completion of two layers of the PBG structures. Our recent effort has been focused on improving the process windows and yield. In the electron-beam-lithography, dummy structures are added to achieve a uniform dose across the die. A thin conducting film is applied over the PMMA to eliminate the charging effect during alignment and exposure. To achieve planarization, a small-scale Chemical-Mechanical Polisher (CMP) has been set up, and a process has been developed to achieve better planarization as well as control over the etch-back process. Due to the smaller polishing wheel, a higher wheel rotation rate of 80 rpm can be used along with hand polishing to achieve higher planarity with a reasonable removal rate of 10nm/min. Fig. 35 shows the results of a planarized one layer structure. Finally, a comprehensive process flow with many cross-checking capabilities was developed.

We believe that the refinements made this year will enable us to succeed in fabricating the 7-layer structure, suitable for optical testing.

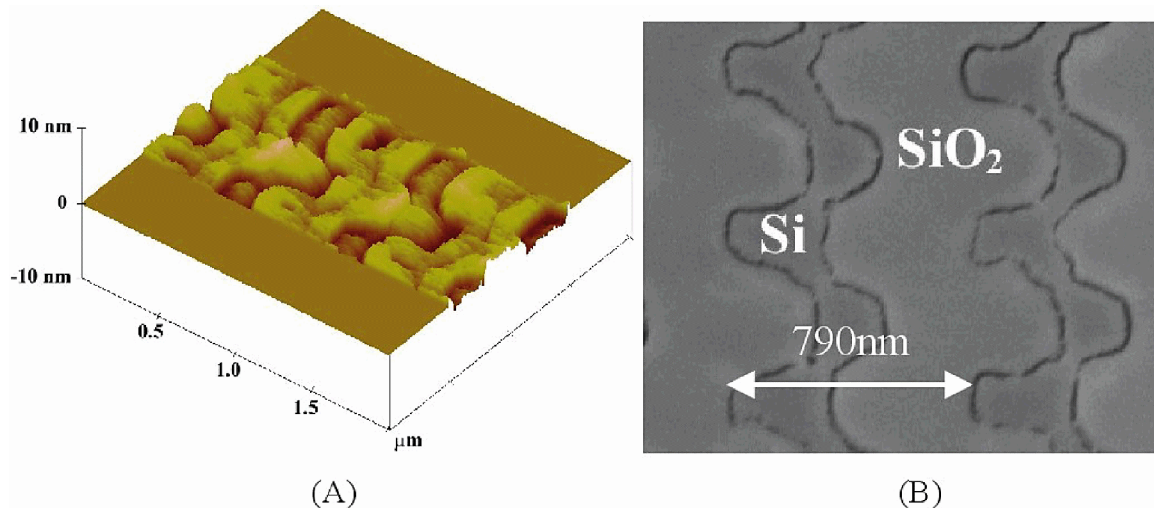


Figure 35. (A) The AFM topography of a fully-planarized one-layer PBG structure. The peak-to-peak value is within 10nm and the root-mean-square (RMS) is less than 3nm. (B) top-view SEM micrograph of the similar structure.

## 16. Development of Fabrication Techniques for Building Integrated-Optical Grating-Based Filters

### Sponsors

Air Force Office of Scientific Research  
Contract: F49620-96-1-0126

### Project Staff

Thomas E. Murphy, Juan Ferrera, J. Todd Hastings, M. Jalal Khan, Elisabeth M. Koontz, Michael H. Lim, Professor Hermann Haus, Professor Leslie A. Kolodziejski, and Professor Henry I. Smith.

Bragg gratings have widespread application in the rapidly growing field of optical telecommunications. A Bragg grating is formed by creating a periodic corrugation or refractive index modulation in an optical waveguide. Such a structure behaves as a wavelength-selective filter, reflecting a narrow band of wavelengths while transmitting all other wavelengths. Fiber Bragg gratings, in which a periodic index modulation is induced in the core of a photosensitive optical fiber, are now manufactured and used for a variety of applications, including dispersion compensation and wavelength add/drop filters. As optical networks spread deeper into the

consumer market, it will become important to have low-cost, manufacturable Bragg grating devices which can be integrated on a chip with other electrical and optical components. The transition from fiber-optic devices to integrated-optical devices may be likened to the development of integrated circuits as a replacement for discrete components. This project seeks to develop the technology for building Bragg grating devices in planar optical waveguides.

Fig. 36 illustrates the general structure of an integrated Bragg grating. Integrated Bragg gratings offer several advantages over fiber Bragg gratings. First, the integrated Bragg grating is formed by physically corrugating a waveguide, therefore it does not rely upon a photorefractive index change. This enables one to build Bragg gratings in materials that are not photorefractive (e.g. Si or InP), and allows stronger gratings to be constructed since the grating strength is not limited by the photorefractive effect. Second, integrated Bragg gratings can be made smaller, and packed closer together than fiber-optic devices. Third, the planar fabrication process gives better control over the device dimensions. For example, the beginning and end of the Bragg grating can be sharply delineated rather than continuously tapered. Abrupt phase shifts can be introduced at any point in a grating, and precise period control can be achieved. In essence, the integrated Bragg grating can be engineered on a tooth-by-tooth basis. Fourth, multiple levels of lithography can be combined, with precise nano-alignment between them, allowing the Bragg gratings to be integrated with couplers, splitters, and other electronic or photonic components. For this reason, relatively sophisticated optical filters can be constructed using integrated Bragg gratings, as described in related reports.

Despite the flexibility afforded by Bragg gratings, their application in integrated-optical devices has been limited to relatively simple components, largely because the required fabrication techniques have not been adequately developed.

The fabrication of integrated Bragg gratings involves two lithography steps: one which defines the relatively coarse waveguide features, and one which defines the fine-period grating features. While the waveguides can be patterned using conventional optical photolithography, high-resolution nanolithography must be used to print the Bragg gratings. Moreover, these two lithography levels must be precisely aligned relative to one another.

We use a combination of many different lithographies to generate the Bragg grating patterns for our devices. Interference lithography is a cornerstone of our Bragg grating work. In interference lithography, two coherent laser beams are crossed, generating a standing wave interference pattern. This standing wave pattern is used to expose photoresist, yielding a coherent deep-submicron-period grating. Which serves as a fiducial reference for subsequent steps.

For devices which require long Bragg gratings with engineered phase shifts, we use a technique called spatially-phase-locked e-beam lithography (SPLEBL), which combines the long-range spatial coherence of interference lithography with the flexibility of e-beam lithography. Using an interferometrically-generated grating as a guide, we are able to write long grating patterns with our e-beam tool, avoiding the inter-field stitching errors which would otherwise spoil the device.

In order to allow precise alignment between the gratings and the waveguides, we have developed a technique of adding alignment marks to interferometrically-generated patterns. In this technique, we use our e-beam lithography system to place alignment marks on an interferometrically-generated pattern. Before writing the alignment marks, the e-beam system samples the existing grating in order to ensure that the marks are precisely aligned to the submicron gratings.

In most cases, the techniques mentioned above are not applied directly to a device, but instead to an x-ray mask. Once the mask is generated, with the appropriate gratings and alignment marks, the patterns can be repeatedly transferred to optical substrates using x-ray lithography.

One of the critical challenges faced by integrated Bragg gratings is that they require submicron grating structures patterned over relatively tall optical waveguides. In order to address this topography problem, we have developed a novel dual-hardmask process, depicted in Fig. 37. This allows both lithography steps to be performed over essentially planar surfaces. The process is quite general, in that it can be applied to almost any waveguide structure. For example, Fig. 38 illustrates how we have used this approach to pattern a quarter-wave-shifted Bragg grating on top of a 1.1 micron-high InGaAsP waveguide. This micrograph illustrates the power and flexibility of our fabrication scheme: we can engineer complex submicron-period Bragg-grating structures with precisely positioned, abrupt phase shifts, placed atop relatively tall waveguide structures. Fig. 39 illustrates how the same technique can be applied to SiO<sub>2</sub> waveguides. Here we see a shallow, 511-nm-period Bragg-grating etched into the top surface of a 4 micron-high waveguide. We are also in the process of applying the dual hard mask process to silicon-on-insulator ridge waveguides.

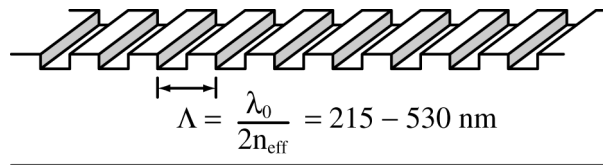


Figure 36: Schematic of an integrated Bragg grating. A shallow corrugation is etched into the top surface of a waveguide. Depending on the index of refraction, the Bragg grating period should be between 215 nm and 540 nm.

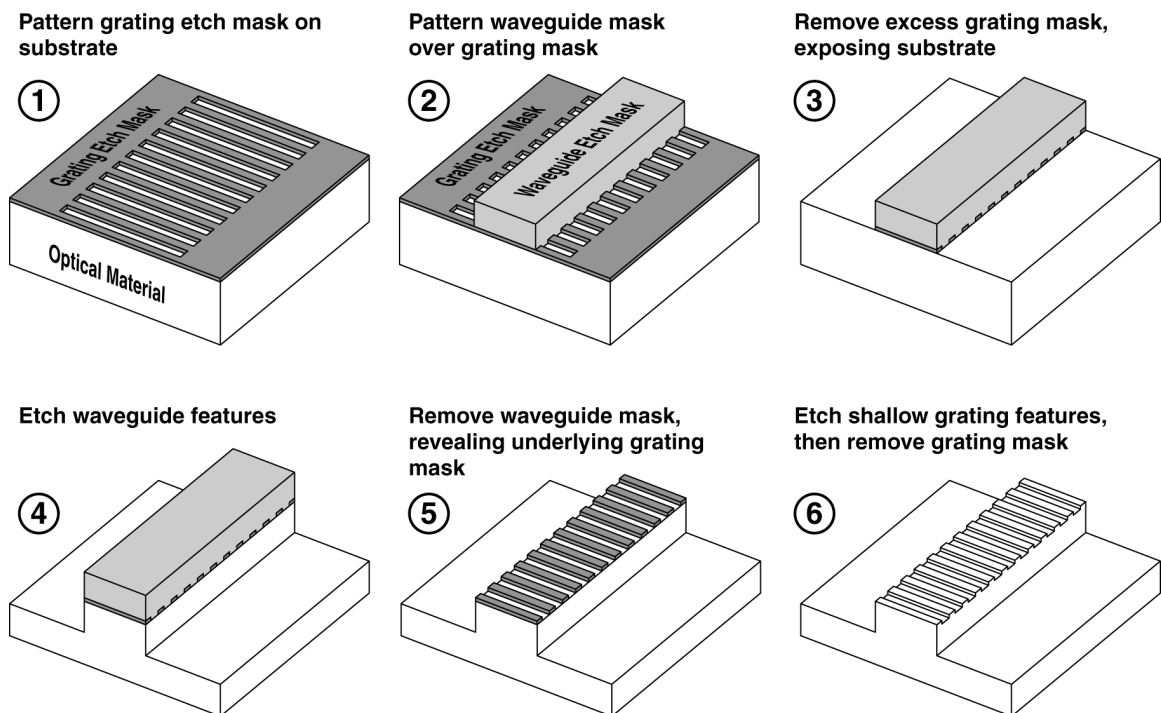


Figure 37: Dual hardmask process used to pattern fine-period Bragg gratings atop relatively tall waveguide structures. The process is designed such that all lithography steps are performed over essentially planar topography.

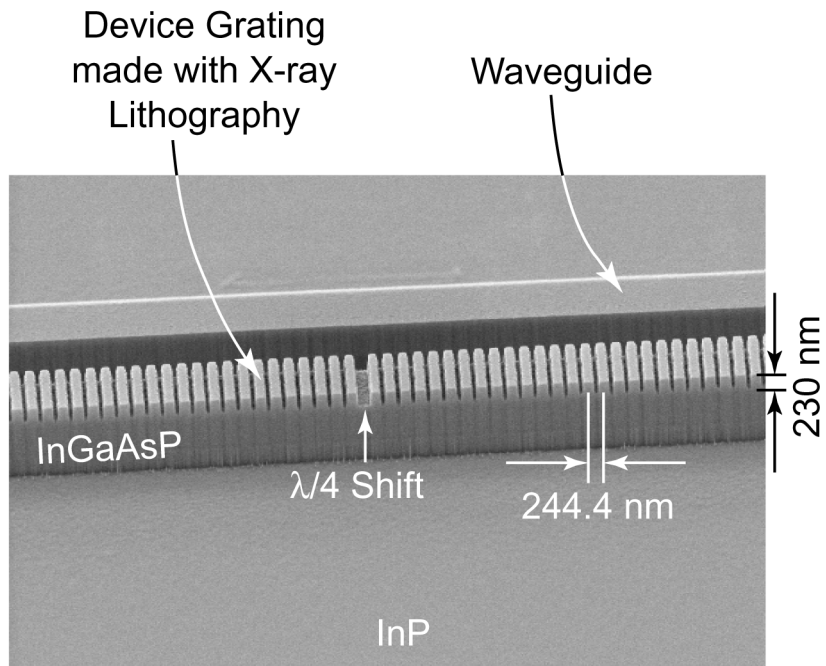


Figure 38: Scanning electron micrograph depicting a quarter wave shifted 245-nm-period Bragg grating etched into the top surface of an InGaAsP waveguide.

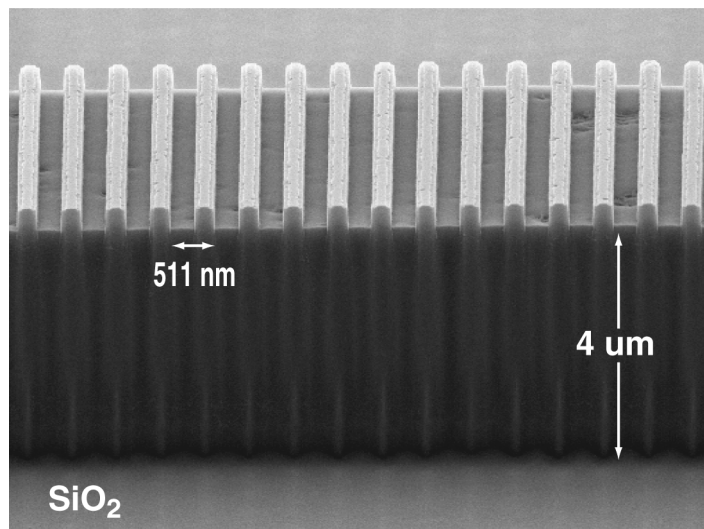


Figure 39: Scanning electron micrograph depicting a 511-nm-period Bragg grating etched into the top surface of a 4-micron-high SiO<sub>2</sub> waveguide.

## **17. Design of Integrated Bragg Grating-Based Filters for Optical Communications**

### **Sponsors**

Air Force Office of Scientific Research

Contract F49620-96-1-0126

### **Project Staff**

Thomas Murphy, Juan Ferrera, J. Todd Hastings, M. Jalal Khan, Michael H. Lim, Professor Hermann Haus, and Professor Henry I. Smith.

As described in related reports, we have developed many new lithographic techniques specifically tailored to meet the needs of integrated Bragg gratings. As a vehicle for demonstrating these techniques, we are in the process of developing two novel devices which could play an important role in future optical networks.

The first device we are developing, depicted in Fig. 40, is based upon quarter-wave-shifted Bragg gratings. When a quarter-wave shift is introduced in an otherwise uniform Bragg grating, the resultant structure behaves as an optical resonator, similar to a Fabry-Perot cavity or a ring resonator. The structure is designed such that only one wavelength channel from a multi-wavelength system will excite the resonator. The device therefore acts as an add/drop filter, enabling the addition or extraction of a channel from the bus waveguide, while leaving all other channels unaffected. The second resonator, located below the bus, ensures that there is no appreciable reflection of the resident channel into the input port of the device.

The device depicted in Fig. 40 is a first-order filter, which has the characteristic Lorentzian bandpass response expected for a single-pole resonator. By cascading multiple resonators, it is possible to achieve more complicated higher-order filters. To address the complex design challenges of these filters, we have developed an equivalent-circuit model that maps the Bragg grating based waveguides onto equivalent electrical circuits consisting of resistors, inductors, and capacitors. Once this association has been made, the spectral response of the filter may be engineered using standard circuit tables. For example, we have used the equivalent circuit technique to design third-order Butterworth filters. Once we have mapped the electrical parameters to their corresponding optical parameters, we use computer simulations to calculate the physical dimensions of the waveguides and gratings that yield the desired values for these optical parameters. This dual approach of using analytic techniques and computer simulations to design devices enables us to generate detailed design tables which take into account, and allow for, unpredictable variations in the manufacturing sequence.

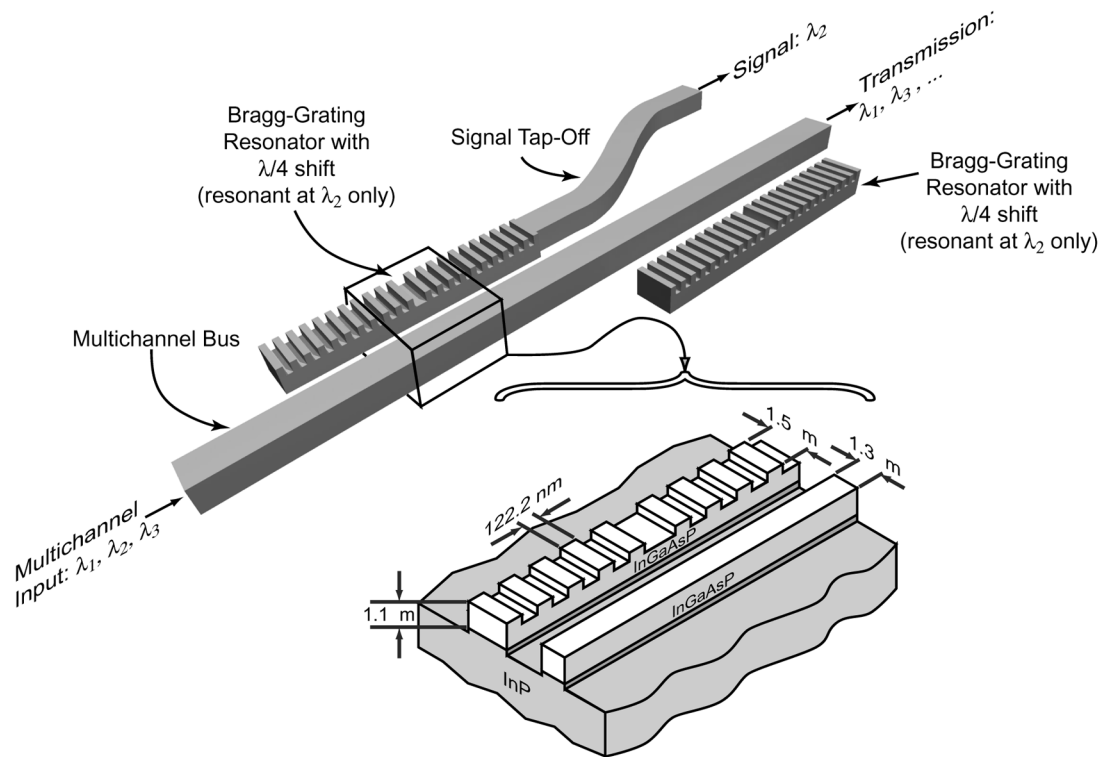


Figure 40: A schematic diagram of the resonator-based add/drop filter. Several independent data channels, each at a different wavelength, travel along the bus waveguide. One channel excites the quarter-wave-shifted Bragg resonator, and is tapped off in the upper port of the device. This device may be operated in reverse, allowing one to selectively add a channel to the bus.

The second device that we are developing, depicted in Fig. 41, is a simpler Bragg-grating filter. The gratings in this device are long, uniform structures without quarter-wave shifts. In this implementation, each of the Bragg gratings acts like a wavelength-selective reflector. The two identical Bragg gratings are integrated in a Mach-Zehnder interferometer, which separates the signals reflected from the gratings from the input signal. Light is launched in the upper left port of the device, and split equally by the coupler. A portion of the light is reflected by the identical Bragg gratings located in the arms of the interferometer. Provided the arm lengths are matched, these reflected signals recombine and emerge in the lower left port of the device.

Depending upon the characteristics of the Bragg grating, the filter can be configured to perform many different functions. For example, by appropriately selecting the length and depth of the Bragg grating, the reflection spectral response can be made to have a bandpass shape. With this configuration, the device performs as an add/drop filter: one wavelength channel is reflected by the gratings, while all other channels pass-through unaffected. The same channel may be simultaneously added by launching it in the upper right port.

Another useful device may be realized by making the Bragg grating very shallow, such that peak reflectivity is small. In this regime, the reflection spectral response of the Bragg grating is well approximated by the Fourier transform of the grating shape. Thus, for a Bragg grating of length  $L$ , the resultant spectral response has the characteristic "sinc" response, with a bandwidth inversely proportional to  $L$ . This device is an ideal pre-detection filter, since it can be engineered to have a spectral response which is matched to that of an on-off modulated data signal. Such a "matched filter" is predicted to yield the optimal signal-to-noise ratio when it is used to filter white

noise from a binary data signal. Theoretical predictions indicate that such a matched filter can yield a twofold increase in the sensitivity of a communications system, when compared with commonly used (nonmatched) filters. This means that the same error-rate performance can be achieved with only half the optical power currently used.

The devices described here illustrate the rich variety of optical filters that can be constructed using integrated Bragg gratings. We are currently in the process of building these devices, using the fabrication techniques described in the prior section.

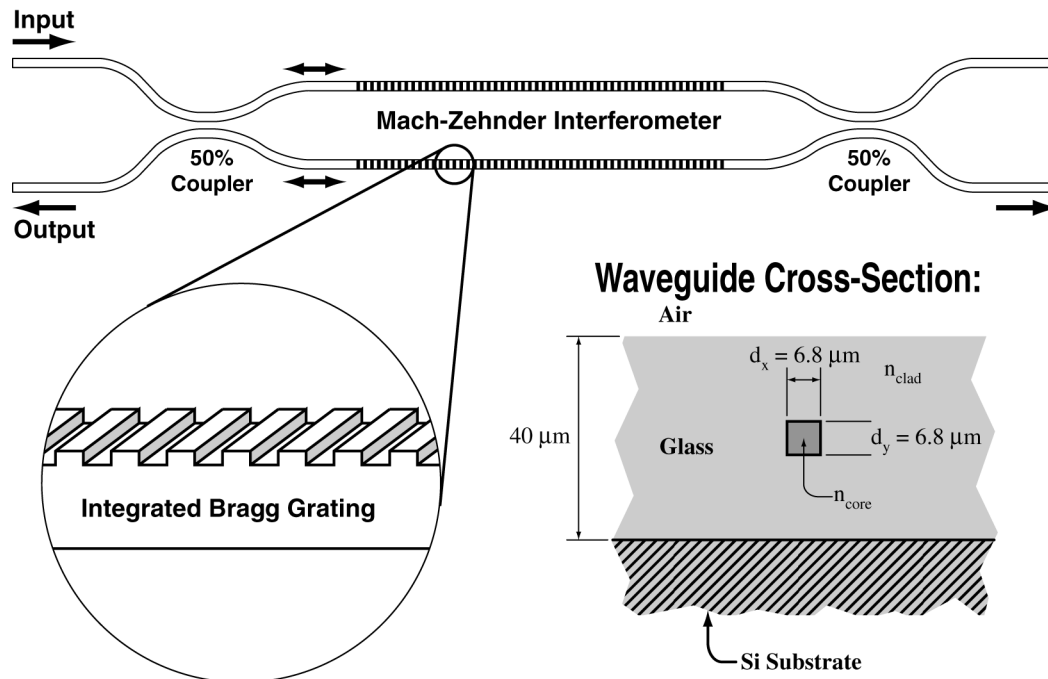


Figure 41: A schematic diagram of Bragg gratings integrated in a Mach-Zehnder interferometer. The identical gratings located in the opposite arms are designed to reflect a portion of the incident light. The filtered signal emerges in the lower left port.

## 18. High-Dispersion X-ray Transmission Gratings for Space Research

### Sponsors

NASA (Contract NAS8-38249), NOAA (through XOPT Inc.)

### Project Staff

Dr. Mark L. Schattenburg, J. Carter, R. C. Fleming, E. Murphy, Professor Claude R. Canizares and Professor Henry I. Smith

High-dispersion x-ray transmission gratings are fabricated for space missions including the NASA *Chandra* x-ray telescope, which was launched in August 1999, and the NOAA Geostationary Operational Environmental Satellites (GOES N, O, P, Q) missions. The *Chandra* telescope provides high-resolution imaging and spectroscopy of x-ray-emitting astrophysical objects, with unprecedented power and clarity, which is significantly widening our view of the Universe. The GOES satellite series will perform solar x-ray monitoring which provides early warning of solar flare events that could imperil satellite and astronaut operations.

Many hundreds of large-area, gold transmission gratings, with 200 nm and 400 nm periods, were required for the High-Energy-Transmission-Grating Spectrometer (HETGS) on *Chandra*, which provides high-resolution x-ray spectroscopy in the 100 eV to 10 keV band (see Fig. 42). In order

to achieve spectrometer performance goals, the gratings need to have very low distortion (<200 ppm), and high-aspect-ratio structures, significantly pushing the state-of-the-art of nanofabrication (see Fig. 43). While the *Chandra* gratings were fabricated on thin (<1.0  $\mu\text{m}$ ) polymer membranes, the GOES gratings need to be freestanding to transmit the softer solar spectrum, and are supported instead by a lithographically-patterned nickel mesh.

The need for high grating quality, and tight production deadlines, demand a robust, high-yield manufacturing process. Gratings are fabricated by interference lithography with a tri-level resist, followed by cryogenic reactive-ion etching and gold electroplating. Additional masking steps followed by nickel plating fabricate the mesh support structure, and a chemical etching step yields mesh or membrane-supported gratings suitable for space use. Additional processing is required to align and bond the gratings to frames suitable for space use. The Space Microstructures Laboratory (SML) has extensive facilities for high-yield volume production of transmission gratings. Gratings undergo extensive testing before assembly into space instrumentation.

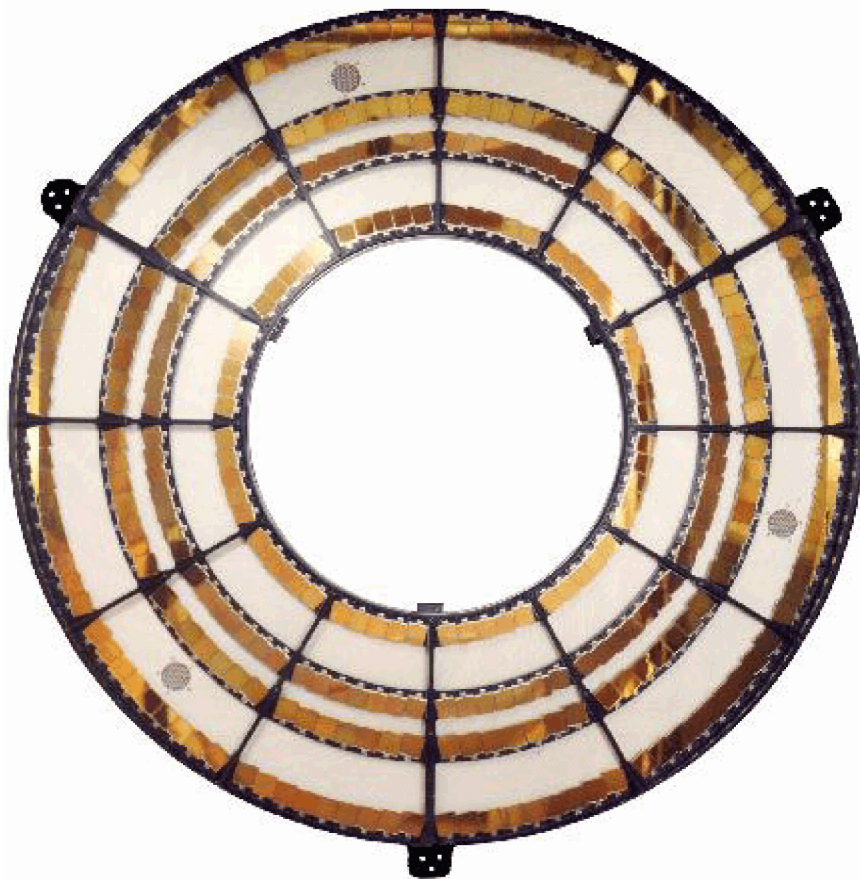


*Figure 42. Photograph of the HETGS flight instrument on the Chandra x-ray telescope, which consists a 1.0 meter-diameter aluminum wheel populated with hundreds of 200 nm and 400 nm-period gold x-ray transmission gratings (340 total).*

# AXAF Gold Transmission Grating

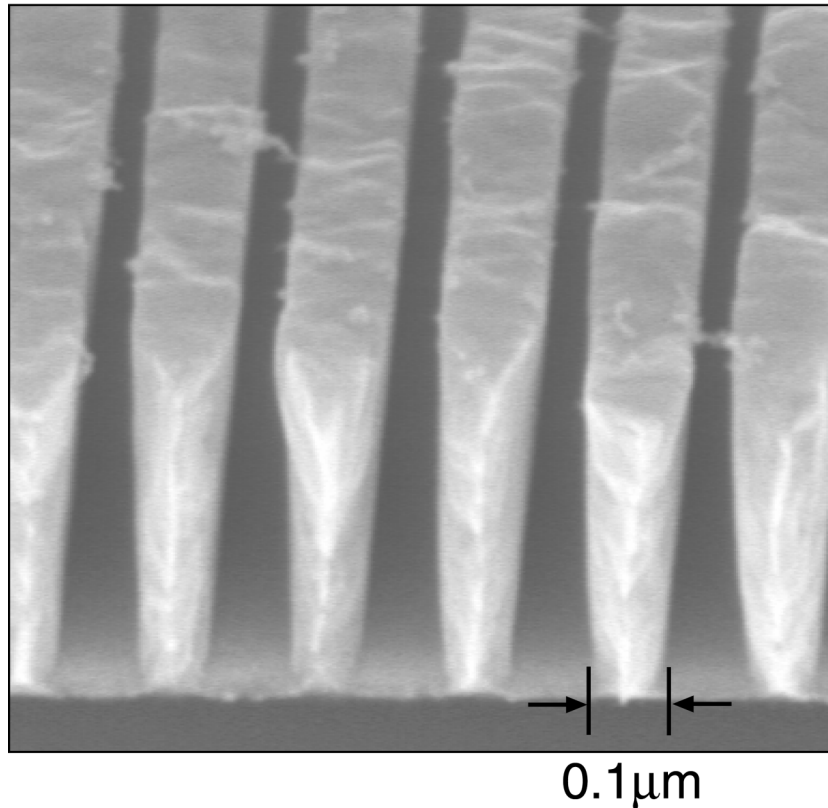


Figure 43. Scanning-electron micrograph of a 200 nm-period gold x-ray transmission grating, cleaved to show the sidewalls of 100 nm wide lines.

## 19. Super-smooth X-ray Reflection Gratings

### Project Staff

Dr. Mark L. Schattenburg, Robert C. Fleming, Ralf Heilmann, Edward Murphy, Professor Claude R. Canizares and Professor Henry I. Smith.

### Sponsors

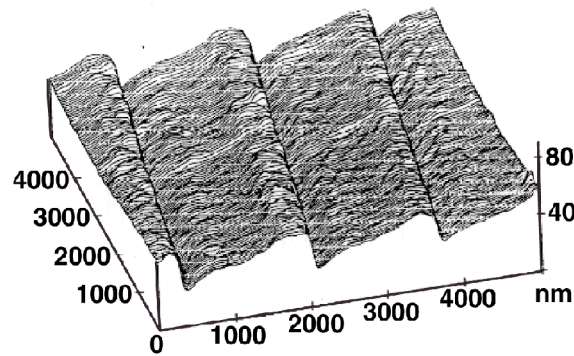
NASA (Grant NAG5-5105), Columbia University (NASA Contract NAS5-98037)

Grazing-incidence x-ray reflection gratings are an important component of modern high-resolution spectrometers and related x-ray optics. These have traditionally been fabricated by diamond scribing with a ruling engine, or more recently, by interference lithography followed by ion etching. These methods result in gratings which suffer from a number of deficiencies, including high surface roughness and poor groove profile control, leading to poor diffraction efficiency and large amounts of scattered light.

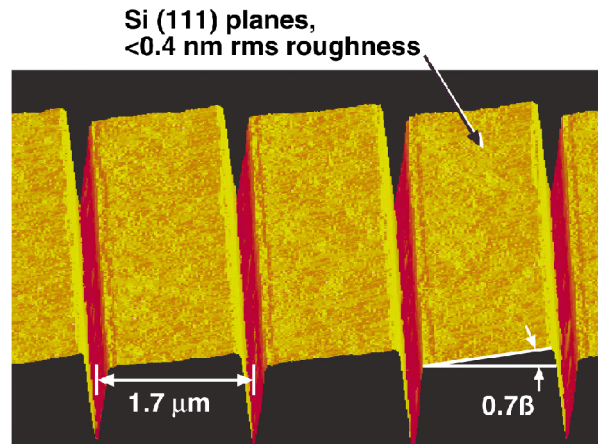
We are developing improved methods for fabricating blazed x-ray reflection gratings which utilize special (111) silicon wafers, cut  $\sim 1$  degree off the (111) plane. Silicon anisotropic etching solutions, such as potassium hydroxide (KOH), etch (111) planes extremely slowly compared to other crystallographic planes, resulting in the desired super-smooth blaze surface. Previous work

used similar off-cut (111) silicon substrates to fabricate blazed diffraction gratings. However, that method utilized a second KOH etch step that compromised the grating facet flatness and is unsuitable for small grazing-angle x-ray diffraction.

Our gratings are patterned using interference lithography with the 351.1 nm wavelength, and transferred into the substrate using tri-level resist processing, reactive-ion etching (RIE), and silicon-nitride masking during the KOH etch. The narrow (~100 nm) ridge of silicon which supports the nitride mask is removed using a novel chromium lift-off step followed by a CF<sub>4</sub> RIE trench etch. The result is extremely-smooth sawtooth patterns, which, after applying a thin evaporative coating of Cr/Au, are suitable for x-ray reflection (see Figure 44). Gratings have been tested with special x-ray spectrometers in the laboratories of our collaborators at Columbia University and the Lawrence Berkeley National Laboratory. Peak gratings efficiencies achieved are ~35% greater than those of the best available ruled masters of comparable design (see Figure 45).



**(a) Mechanically Ruled**



**(b) Anisotropically Etched**

Figure 44: (a) An AFM image of a traditional mechanically-ruled and replicated x-ray reflection grating (Bixler et al., Proc. SPIE 1549, 420-428 [1991]). Note the rough, wavy grating surfaces that lead to poor diffraction performance. (b) An AFM image of a blazed x-ray reflection grating fabricated by anisotropic etching of special off-cut (111) silicon wafers. Note the improvement of grating surface flatness and smoothness, leading to significantly improved performance.

Potential applications of these improved gratings are for synchrotron studies and satellite-based high-resolution x-ray spectroscopy for planned NASA missions such as *Constellation X*. The current phase of the work involves patterning gratings on super-flat wafers, and trimming the substrates into the desired rectangular format.

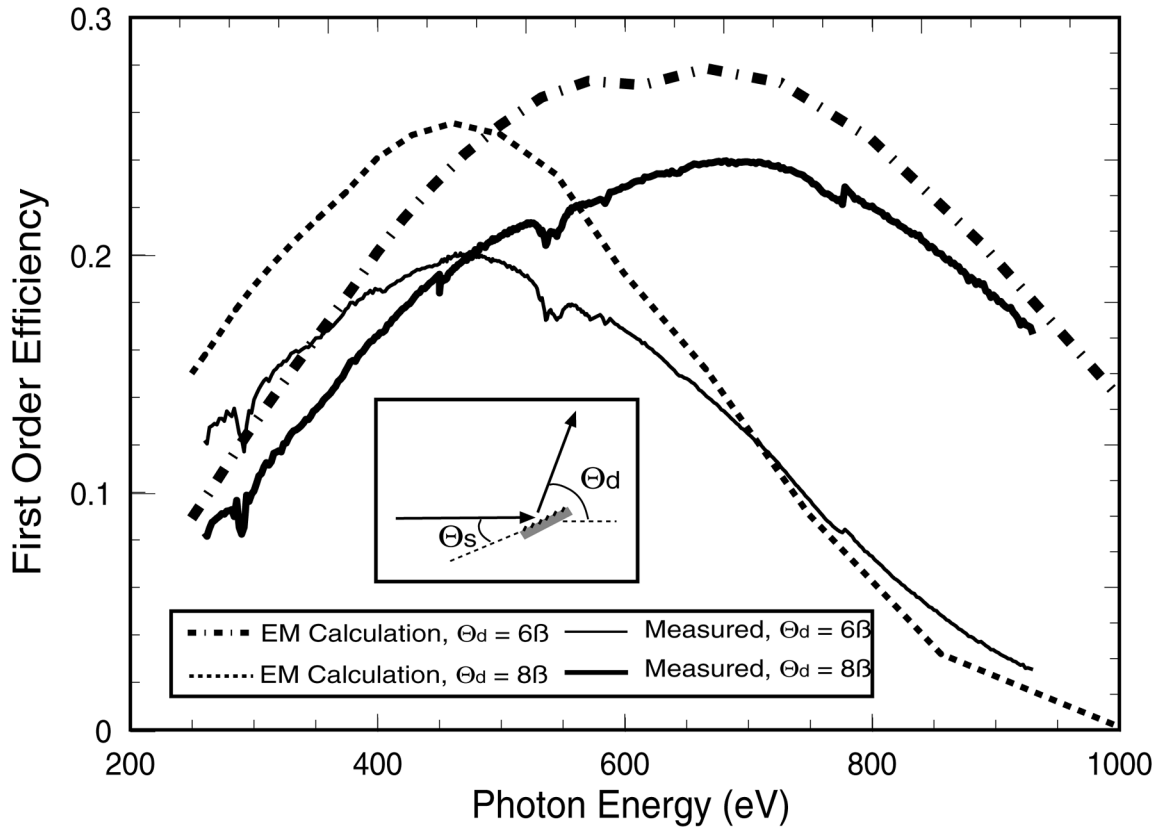


Figure 45: Comparison of x-ray diffraction efficiency measured at Lawrence Berkeley Laboratory and electromagnetic finite-element calculations performed at Columbia University. Peak gratings efficiencies achieved are ~35% greater than those of the best available ruled masters of comparable design.

## 20. UV-blocking Transmission Gratings Filters for Neutral Atom Imaging

### Project Staff

Dr. Mark L. Schattenburg, James Carter, Robert C. Fleming, Edward Murphy, Professor Claude R. Canizares and Professor Henry I. Smith.

### Sponsors

LANL (Contract G3630019-97), SwRI (Contract 83832)

Neutral-atom-beam imaging detectors are used to study dilute plasmas in astrophysical environments such as the magnetospheric regions of the Earth and other planets, and laboratory systems such as Tokamaks. Neutral atom emission can be a particularly useful probe of plasmas since neutrals travel in straight lines-of-sight, unperturbed by electromagnetic fields.

Charge-exchange interactions between Solar-wind particles and atoms in the Earth's tenuous outer atmosphere are predicted to form strong currents of neutral atoms (mostly oxygen and helium) emanating from the Earth, which, if they could be imaged, would provide unprecedented real-time mapping of this complicated magnetohydrodynamic environment. This information

would be valuable in order to safeguard the health of orbiting satellites, and ensure the stability of our nation's electric power grid.

Unfortunately, sensitive orbiting neutral-beam detectors are easily overwhelmed by the bright flux of UV photons typically emitted from astrophysical plasmas (mostly the 121.6 nm emission from hydrogen and the 58.4 nm emission from helium). Filters that allow the passage of low-energy neutral atoms but block UV light are essential for the performance of this instrumentation. Through several years of collaboration with the Los Alamos National Laboratory (LANL), the University of West Virginia, the University of Southern California, and the Southwest Research Institute (SwRI), we have developed neutral beam filters which consist of mesh-supported, 200 nm-period, gold transmission gratings with 30-60 nm wide slots. The tall, narrow slots in the gratings behave as lossy waveguides at or below cutoff, providing UV discrimination to particles on the order of millions.

The Space Microstructures Laboratory has been awarded contracts by SwRI and LANL to deliver a quantity of flight grating filters for the Medium Energy Neutral Atom (MENA) instrument on the NASA Magnetospheric Imaging Medium-Class Explorer (IMAGE) mission, scheduled for launch in February 2000, and improved gratings for the NASA Two Wide-Angle Imaging Neutral-atom Spectrometers (TWINS A, B) Missions.

Gratings are fabricated by interference lithography with tri-level resist, followed by cryogenic reactive-ion etching and gold electroplating. Additional masking steps followed by nickel plating fabricate the mesh support structure, and a chemical etching step yields mesh-supported gratings suitable for space use. Additional processing is required to align and bond the gratings to frames suitable for space use.

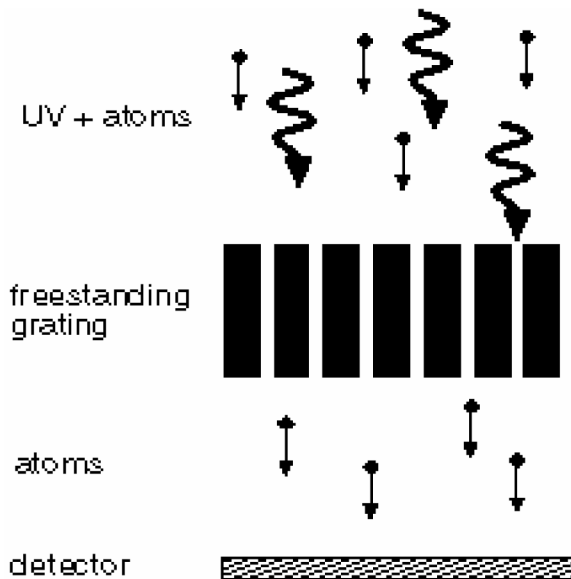


*Figure 46. Concept of UV filtering by means of a metal freestanding grating. As a result of polarization and waveguide effects, UV is blocked while allowing the passage of atoms. In this way, UV background counts on the atom detector are avoided.*

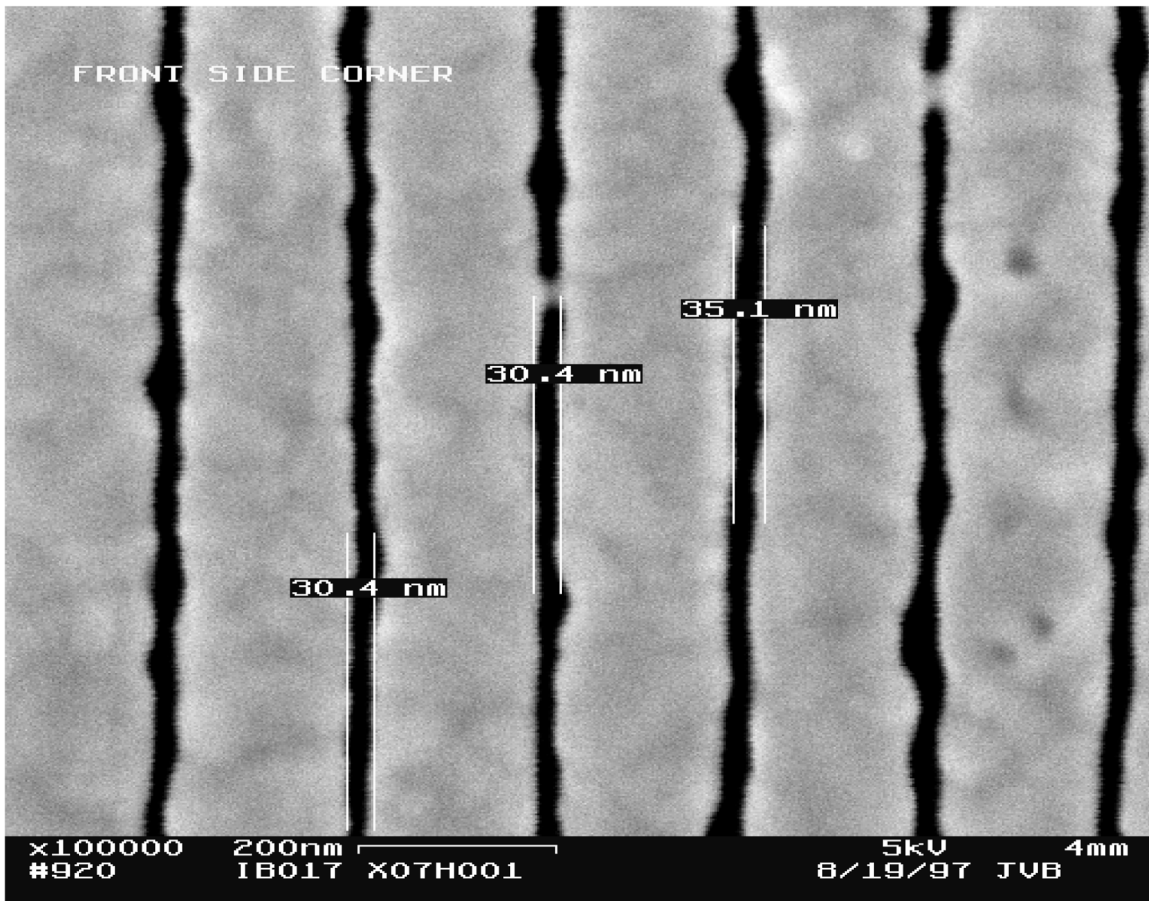


Figure 47. Scanning-electron micrograph image of a UV blocking grating. Due to the narrow slot width of 30-35 nm, and the large slot depth (~500 nm), the UV transmission is extremely low ( $10^{-6}$  to  $10^{-7}$  at 121.6 nm), while decreasing the transmitted atomic flux by only a factor of 10.

## 21. Transmission Gratings for X-ray and Atom-Beam Spectroscopy and Interferometry

### Sponsors

X-OPT, Inc.

### Project Staff

Timothy A. Savas, James M. Carter, Edward Murphy, Dr. Mark L. Schattenburg, and Professor Henry I. Smith

Transmission gratings with periods of 100 to 1000 nm are finding increasing utility in applications such as x-ray, vacuum-ultraviolet, and atom-beam spectroscopy and interferometry. Over 30 laboratories around the world depend on MIT-supplied gratings in their work. For x-ray and VUV spectroscopy, gratings are made of gold and have periods of 100 to 1000 nm, and thicknesses ranging from 100 to 1000 nm. The gratings are most commonly used for spectroscopy of the x-ray emission from high-temperature plasmas. Transmission gratings are supported on thin (1 micron) polyimide membranes, or made self supporting ("free standing") by the addition of crossing struts (mesh). (For short x-ray wavelengths, membrane support is desired, while for the long wavelengths, a mesh support is preferred in order to increase efficiency.) Fabrication is performed by interference lithography combined with reactive-ion etching and electroplating.

Progress in this area tends to focus on improving the yield and flexibility of the fabrication procedures.

Another application is the diffraction of neutral-atom and molecular beams by mesh supported gratings. Lithographic and etching procedures have been developed for fabricating free-standing gratings and grids in thin silicon nitride (SiN<sub>x</sub>) membranes supported in a Si frame. Figure 48 shows a free-standing 100 nm period grating in 100 nm-thick silicon nitride. Figure 49 shows a 100 nm-period grid in a 100 nm-thick SiN<sub>x</sub> membrane. Such a grid is used in experiments as a "molecular sieve."

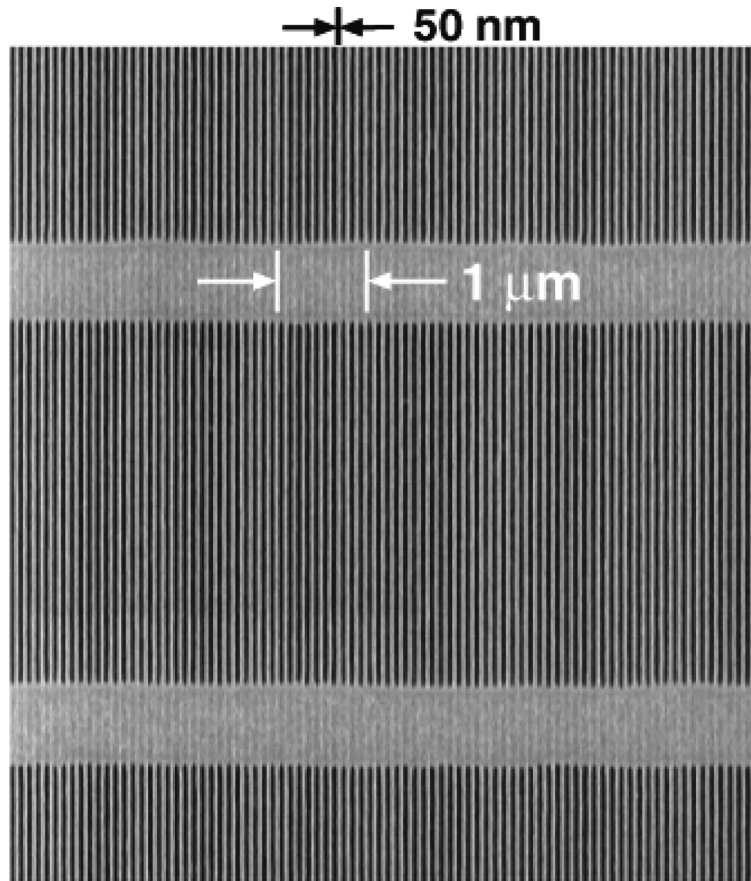


*Figure 48. Scanning electron micrograph of a free-standing 100 nm-period grating (50 nm-wide bars) in a silicon nitride membrane of area 500 microns by 5 mm.*

We have established a collaboration with the Max-Planck Institute in Goettingen, Germany, in which they utilize our gratings and grids of 100 nm period in diffraction experiments using He atom beams. Figure 50 shows a spectrum obtained by diffracting a He beam through a 100 nm-period transmission grating. Figure 51 shows the transmission of a grating as a function of helium-beam incident angles. Data obtained by He diffraction at large incident angles showed Lyman ghosts in the spectrum. This data led to the development of new fabrication techniques to improve the quality of the free-standing gratings in silicon nitride. Diffraction spectra from gratings made with the improved process show no Lyman ghosts, illustrating the important synergy between applications and nanofabrication.

Highly successful diffraction experiments with beams of buckyballs (C<sub>60</sub>) have been carried out with our 100 nm-period, free-standing SiN<sub>x</sub> gratings by Dr. Markus Arndt of the University of Vienna.

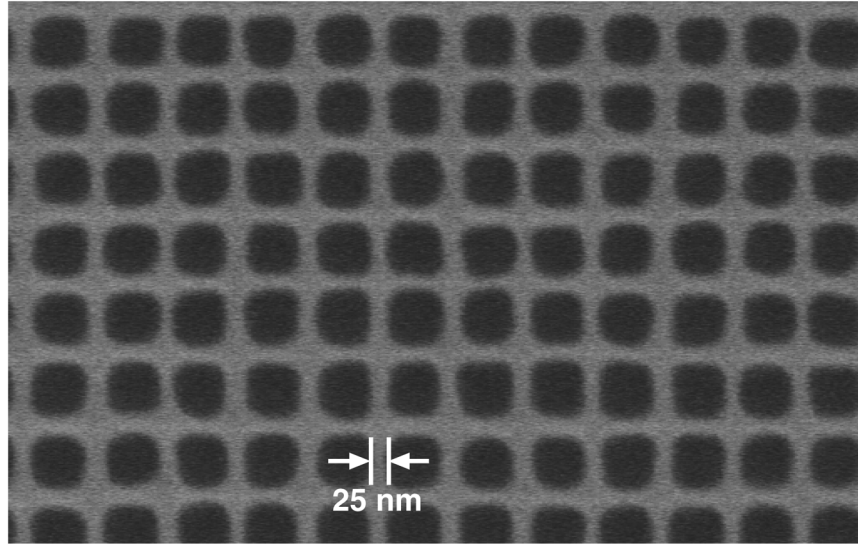


Figure 49. Scanning electron micrograph of a free-standing 100 nm period grid in a silicon nitride membrane of area 500 micron by 5 mm. Such grids are used in experiments to separate out Helium trimers from other clusters.

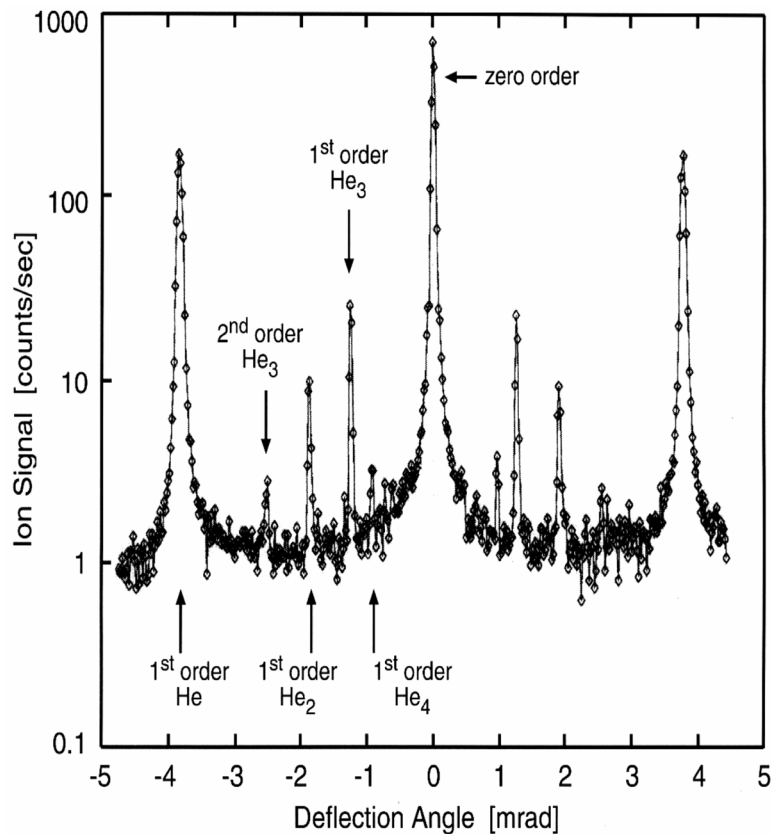


Figure 50. Helium beam diffraction spectrum. These results were obtained by Wieland Schoellkopf and Peter Toennies at the Max-Planck Institute in Goettingen, Germany, using a free-standing, 100nm period grating.

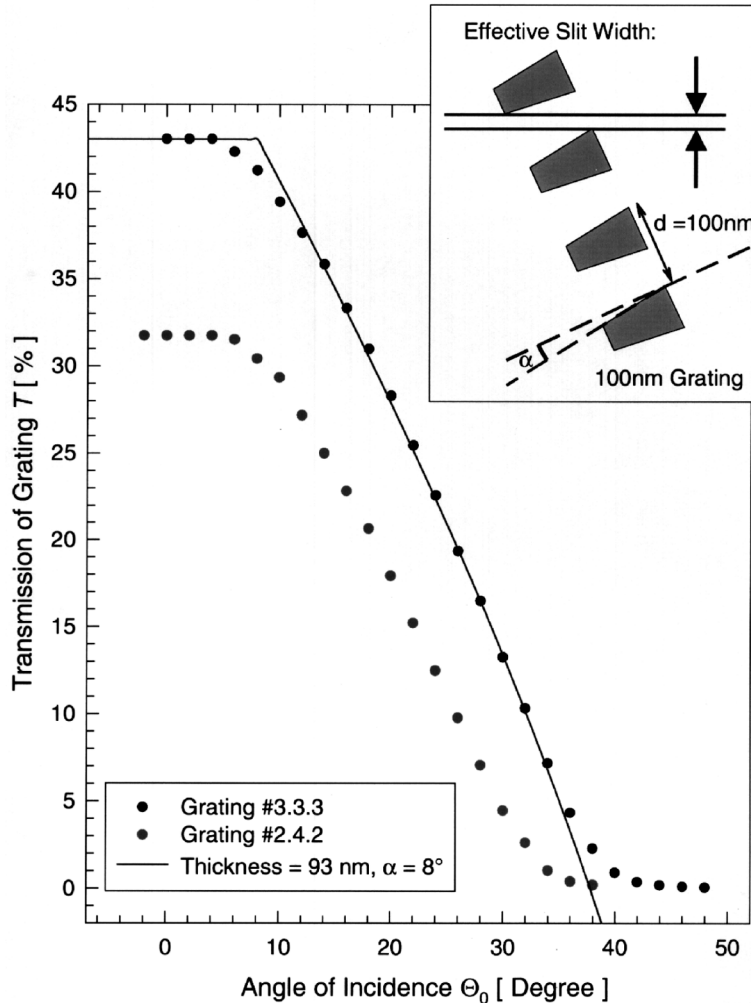


Figure 51. Measured total transmitted intensity through a 100 nm-period free-standing grating as a function of incident angle for a He atom beam. The line is a fit assuming a truncated wedge shape for the cross section of the grating bars, as depicted in the inset. Analysis indicated a grating thickness of 93 nm and a wedge angle of 8 degrees.

Our 100 nm-period free-standing SiNx gratings are also used for atom interferometry by two groups: those of Prof. David Pritchard of MIT and Prof. Bruce Doak of the State University of Arizona. Pritchard's group interferes neutral beams of sodium atoms while Doak's group interferes helium beams (performed at the Max Planck Institute in Goettingen, Germany in collaboration with P. Toeneis).

## 22. Sub-100 nm Metrology Using Interferometrically Produced Fiducial Grids

### Project Staff

C. Chen, P. Konkola, R. Heilmann, Dr. Mark L. Schattenburg and Professor Henry I. Smith

### Sponsor

DARPA/ARO (Grant DAAG55-98-1-0130)

The ability to see and measure the results of a process is critical to advancing fabrication technology. Historically, the development of improved microscopy techniques led to rapid progress in microfabrication. Thus, the scanning-electron microscope was essential to the

microelectronics revolution. Similarly, the scanning-tunnelling microscope is creating a revolution in the study of interfaces and nanostructures.

In the past, metrology of microstructures and the measurement of workpiece distortion (e.g., a photolithographic reticle or x-ray mask) has been based on point-by-point measurement through an optical microscope using an X-Y table monitored by a laser interferometer. Although this approach enables relative distances in a plane to be measured with 1 nm-level detectivity, it is expensive, tedious, and subject to a number of shortcomings, including the necessity of placing rather perturbative marks on a workpiece. We have initiated a new approach to metrology for the sub-100 nm domain that is based on large-area fiducial grids produced by interference lithography. This new approach is complementary to the point-by-point approach in much the same way that aerial photogrammetry is complementary to ground-based land surveying for the mapping of terrain.

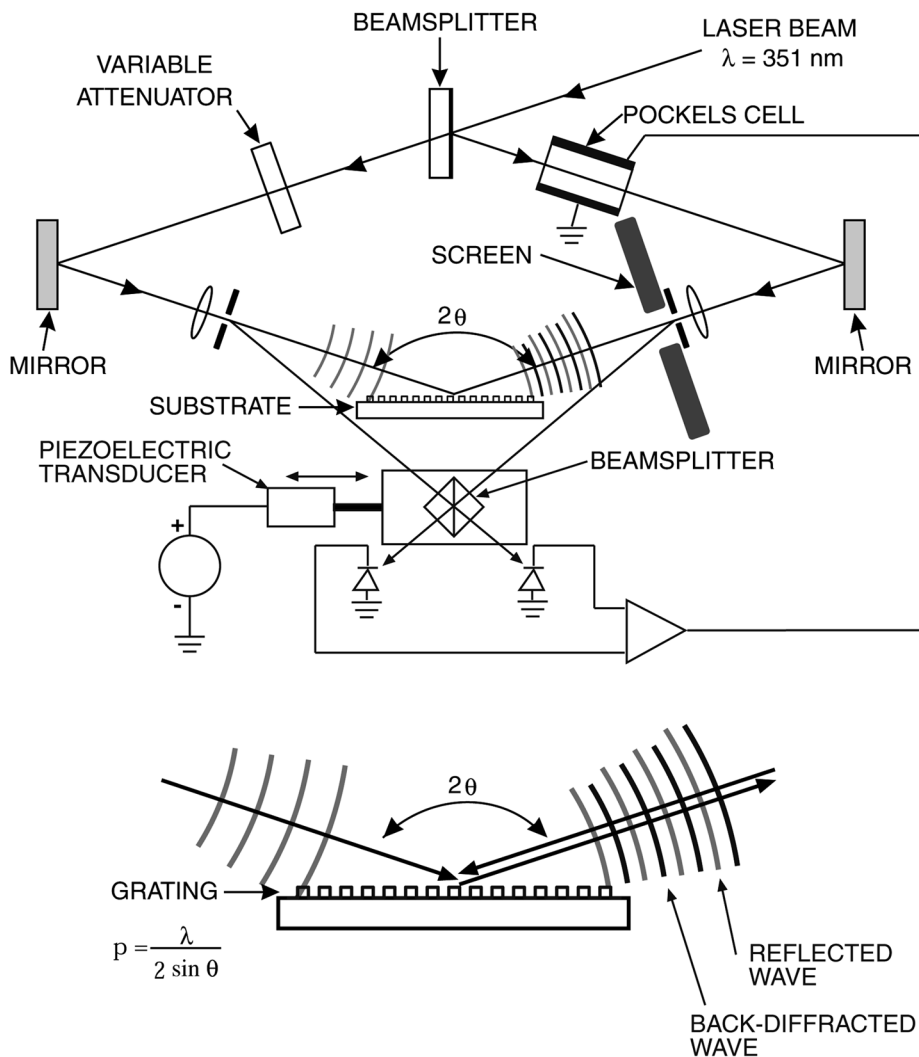
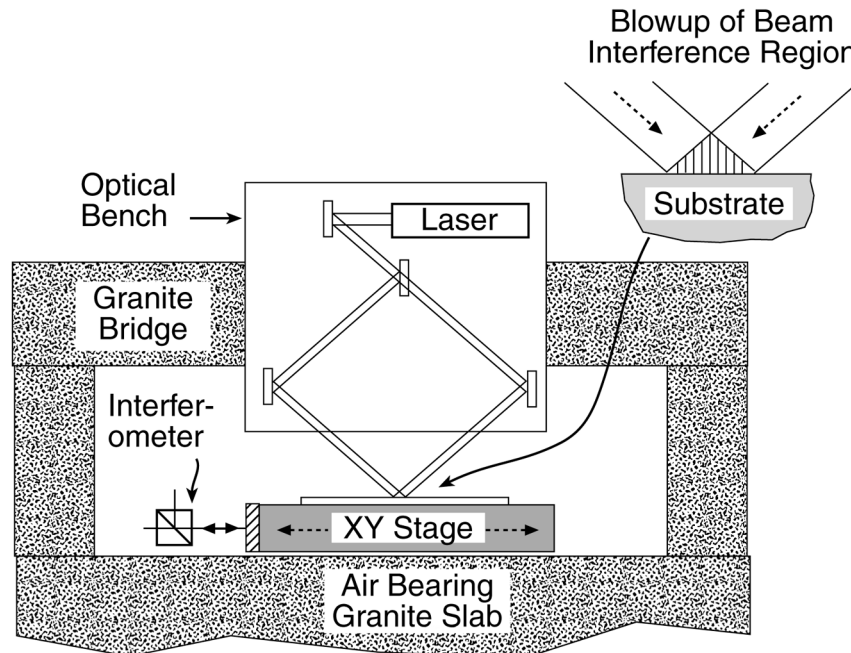
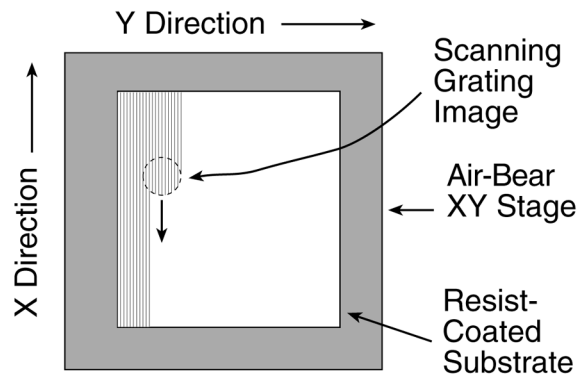


Figure 52: Schematic of the holographic phase-shifting interferometer (HPSI). A spherical wave back-diffracted from a shallow substrate grid, and a second wave specularly reflected, interfere on a fluorescent screen at the spatial filter. The fringes are imaged onto a CCD. By shifting the beam splitter with a piezo, a computer generates an X-Y map of phase error.

A key element in this new initiative is the holographic phase shifting interferometer (HPSI), illustrated in Figure 52. This system, once it is fully developed, will enable us to measure in a global manner the in-plane distortion of a workpiece, provided one of its surfaces contains a shallow fiducial grid. Ideally, the grid on the workpiece will be created by interference lithography or a derivative thereof, such as near-field holography.



a) Scanning beam interferometer.



b) Grating scanning method.

Figure 53: Schematic of the scanning-beam-interference lithography (SBIL) system. A pair of narrow, distortion-free beams overlap and interfere at the substrate, producing a small grating patch. The substrate is moved under the beams, writing a large area grating. Sophisticated electro-optical components (not shown) ensure phase locking of the grating during writing.

As part of this new initiative in sub-100 nm metrology, we are pursuing a variety of approaches to eliminating the distortion in interferometrically produced grids, decreasing the coefficient of the hyperbolic phase progression (a consequence of creating a grid by interfering spherical wavefronts), and increasing the useful area of fiducial grids. One such approach is scanning-

beam interferometric lithography (SBIL), depicted schematically in Figure 53. The concept here is to combine the sub-1nm displacement measuring capability of laser interferometry with the interference of narrow coherent beams to produce coherent, large-area, linear gratings and grids. Our ultimate goal is to produce such gratings over areas many tens of centimeters in diameter.

### **23. Field Emitter Array Flat Panel Displays for Head-Mounted Applications**

#### **Sponsorship**

Lincoln Laboratory - #BX-5956

#### **Project Staff**

David Pflug, Dr. Mark Schattenburg, Professor Akintunde I. Akinwande, Professor Henry I. Smith, Dr. Carl Bozler

Advances in nanostructure technology have made feasible small, high-resolution, high-brightness and high-luminous-efficiency field-emitter-array sources for Head-Mounted Displays (HMDs). HMDs are expected to have a variety of applications in military, medical, commercial and entertainment fields. The technology most commonly used in deployed HMD systems is the CRT which is bulky, because of the use of a single electron gun to generate images on a cathodoluminescent screen, but has the most desirable attributes of high luminous efficiency, high brightness and easy image rendition. However, the relay optics required for see-through HMDs become complicated because of the bulky nature of the CRT. For other applications, such as entertainment virtual reality, the most commonly used image source is the backlit Active-Matrix-Liquid-Crystal Display (AMLCD), which is thin and has high resolution. Furthermore, the addressing electronics are integrated on the same substrate as the image source. However, the backlit AMLCD image source does not have sufficient brightness nor luminous efficiency to make it suitable for application to see-through HMDs.

Our approach to demonstrating a small, high-resolution, high-luminous-efficiency and high-brightness display is the field-emitter-array Flat-Panel Display (FED) which incorporates a high-density, high-performance array of low-voltage field emitters, as shown in Figure 54. CMOS-controlled electron emission from the tips impinges on a cathodoluminescent screen. It is thus possible to integrate the addressing and signal conditioning electronics on the same substrate as the Field Emitter Arrays (FEAs). The main advantage of this approach is the reduction of the number of wires and bond pads from about 2,000 to about 50. For example, it will be difficult to attach > 2,000 wires to bond pads in an area of 1.5" x 1.5" and obtain ultra-high vacuum in the display envelope. High resolution (>1000 dpi) FEDs are only possible if the addressing/driver and other signal conditioning electronics are integrated on the same substrate as the field emitter arrays.

Our initial objective is to demonstrate the integration of Si CMOS technology with low-voltage field-emitter arrays fabricated using interferometric lithography. This project requires the fabrication of Si CMOS wafers with one or two levels of metal interconnect, followed by surface planarization using CMP technology. Interferometric lithography is then used to define Mo-cone field emitter arrays that are spaced 200 nm tip-to-tip and have <50 nm gate-to-emitter separation. Fabricated cone-field-emitter arrays with a 320 nm period have demonstrated emission currents of 1 mA at a gate voltage of 20V from 900 cones in a 10  $\mu\text{m}$  x 10  $\mu\text{m}$  area. This current is more than adequate for a brightness of 1000 fL at a screen voltage of 500V.

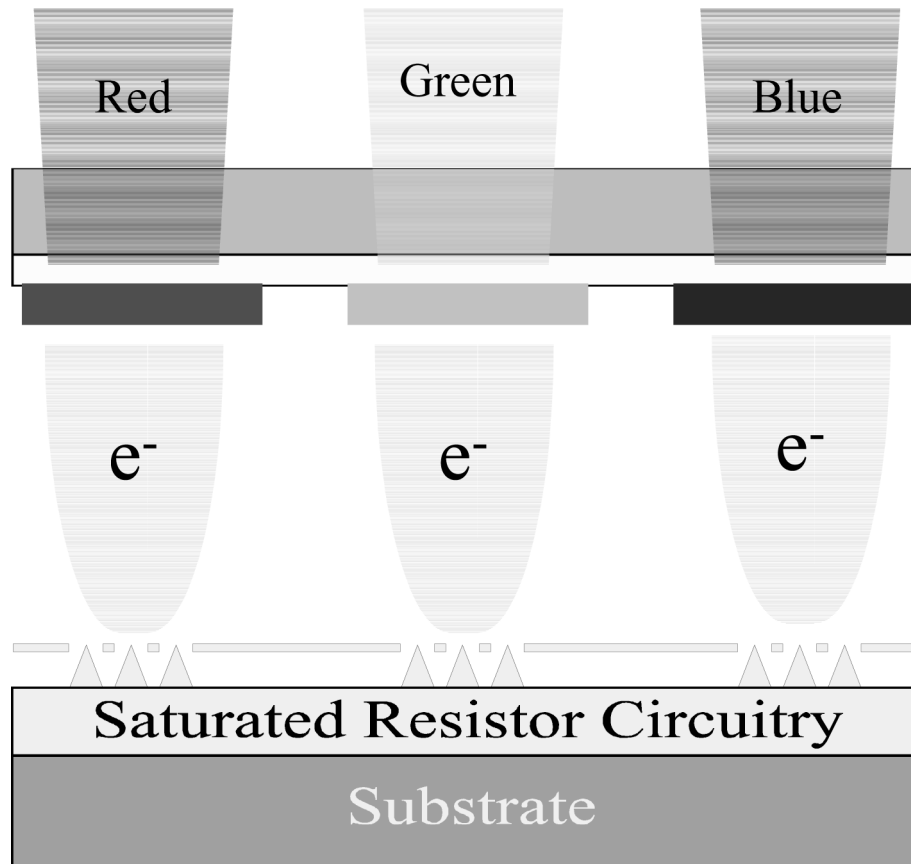


Figure 54: Concept of a field emission display pixel. The display would use a 2D matrix addressable electron source allowing temporal and spatial modulation.

Our initial efforts focused on modeling the scaling behavior of FEA devices. Numerical simulation and computer models to predict FEA performance have been developed and continue to be refined. These models allow us to obtain a correlation between different device geometries (cone tip radius or curvature, gate aperture, etc.) and the emitter's output characteristics. The results of this study have directed our fabrication efforts toward devices whose performance will not only be better, but more dependent on geometries that can be well controlled in the manufacturing process. Simulation results indicate that we will be able to increase the current density and reduce the operating voltage, by decreasing the tip-to-tip separation to 200 nm.

FEAs of 200 nm period have been fabricated by using interferometric lithography and standard processing techniques. Additional metallization layers and conventional lithography were used to create discrete Molybdenum Spindt arrays for electrical characterization. The fabricated cones have similar size and structure to those simulated, Figure 55. Standard CMOS processing techniques have been also been combined with the interferometric lithography to form 200 nm-period arrays of Si etched cones, Figure 56.

A semi-automated Ultra High Vacuum (UHV) probe chamber has been developed for the electrical characterization of FEAs. This test bed allows the performance of the arrays to be evaluated without the lengthy overhead of vacuum packaging devices. Device performance has been shown to be not only dependent on the device physical structure, but also on surface contamination that may have resulted during fabrication and MEMS processing. The UHV probe chamber has the capability to do device conditioning including ECR plasma cleans and wafer bake-out. The system is designed to allow the future expansion to include surface analysis chambers including a Kelvin Probe, Scanning Maxwell Microscope and Auger.

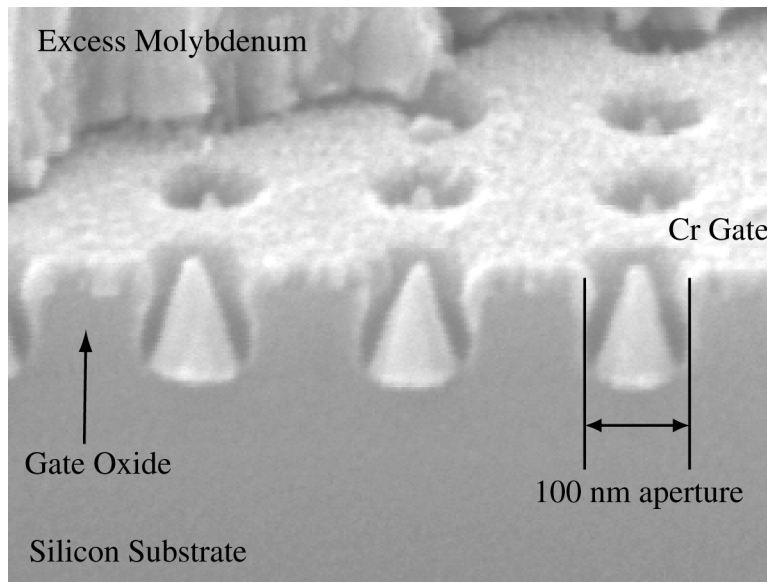


Figure 55: 100 nm gate aperture molybdenum field-emitter cones with chromium gate formed using a vertical evaporation

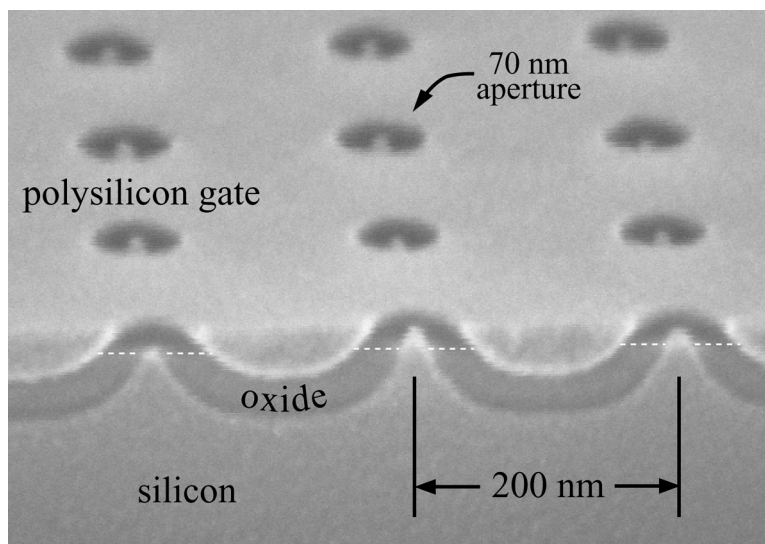


Figure 56: 200 nm-period, 70 nm-aperture Silicon arrays with polysilicon gate. Array was formed by a rough cone formation, oxidation sharpening and CMP planarization.

Electrical characterization of the 100 nm-aperture Molybdenum arrays (200 nm tip-to-tip spacing) has shown that arrays can operate at voltages as low as 16 volts and provide adequate current to support flat panel display applications, as illustrated in Figure 57. We have demonstrated initial testing of low-gate-voltage FEAs with discrete solid state devices. We replace the resistor that previous approaches have used to limit and control emission current with a MOSFET. Current control is critical to the uniformity of brightness across the display because Fowler-Nordheim emission depends exponentially on the ratio of the gate voltage to the tip radius-of-curvature ( $V_g/r$ ). It is therefore very sensitive to small changes in the radius-of-curvature. It was possible to control the emitted current density using the gate voltage of the transistor load. This may enable analog voltage gray scale or temporal gray scale, Figure 58.

The above demonstration has gone a long way to show the feasibility of high brightness, high-resolution FEA image sources for head-mounted displays.

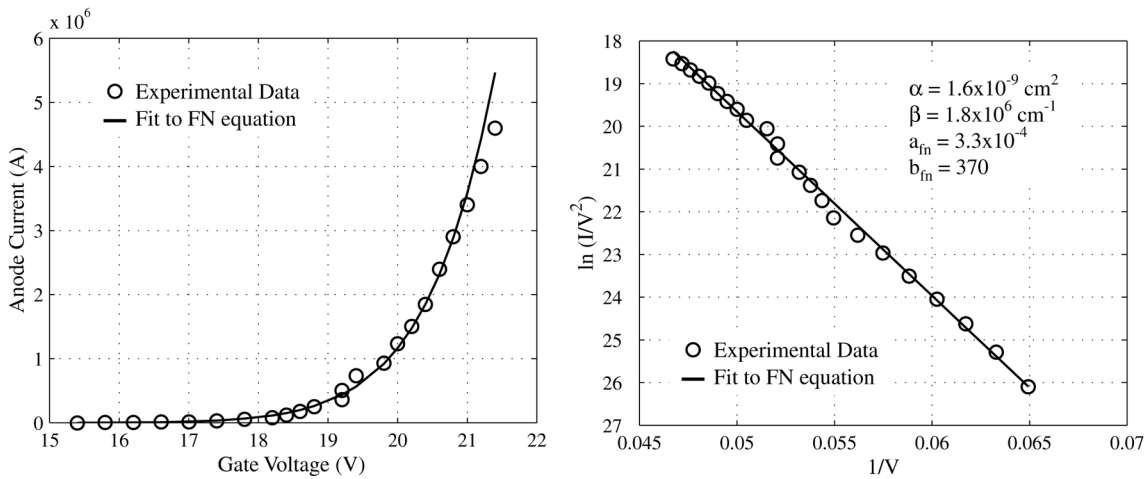


Figure 57: (left) Molybdenum-array anode current vs. gate voltage for 100 nm gate aperture array. (right) Fowler Nordheim plot confirming that field emission is the dominant contributing factor for the anode current.

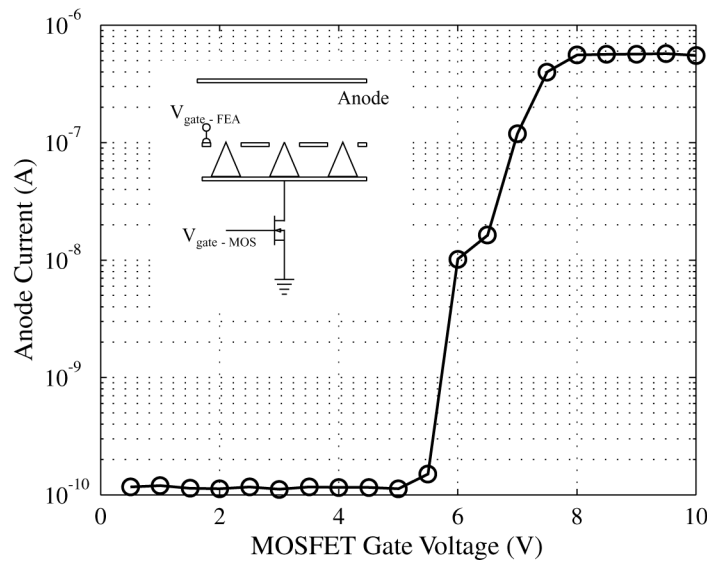


Figure 58: Molybdenum array anode current vs. MOSFET gate voltage showing control of over 3 orders of magnitude of the anode current with small variations in the MOSFET gate voltage.

## 24. High-Accuracy Assembly of X-ray Foil Optics

### Sponsors

NASA (Grant NAG5-5105), GSFC (NASA Grant NCC5-330)

### Project Staff

C. Chen, P. Konkola, O. Mongrard, G. Monnelly, Dr. G. R. Ricker and Dr. Mark L. Schattenburg.

Future x-ray astronomy missions will require orders of magnitude improvements in collecting area and resolution. Foils optics are attractive candidates for telescope optics because of the tremendous weight and cost savings which can be achieved compared to traditional monolithic optics. However, substantial improvements in our ability to form and assemble foils to high accuracy will be required. In this new research initiative we are applying a variety of microlithographic technologies to the patterning of assembly structures for the alignment and registration of foil optic components, both reflective and diffractive.

Silicon MEMS technology is used to lithographically fabricate silicon microstructures designed to guide and reference glass foils into precise three-dimensional shapes. Thousands of  $\sim 200 \mu\text{m}$ -thick foils are typically required for an x-ray telescope, each assembled to submicron accuracy. Fig. 59 shows SEM images of two types of microcombs under development.

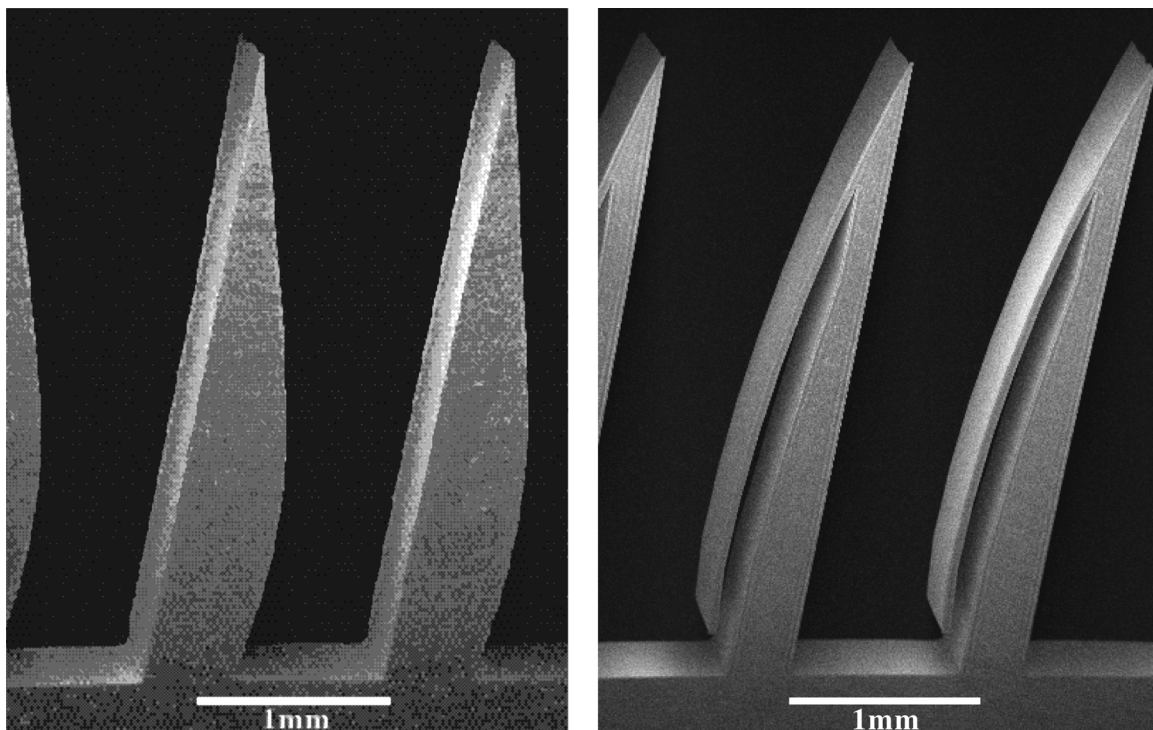


*Figure 59. Electron micrographs of silicon microcombs. Teeth are  $\sim 500 \mu\text{m}$  wide. Left: Reference comb. Right: Spring comb.*

## **25. Development of High Speed DFB and DBR Semiconductor Lasers**

### **Sponsors**

MIT Lincoln Laboratory, Contract BX-6558

### **Project Staff**

Farhan Rana, Michael H. Lim, Elisabeth Koontz, Professor Rajeev Ram, Professor Leslie Kolodziejewski and Professor Henry I. Smith.

High-speed semiconductor DFB and DBR lasers are crucial for high-speed optical communication links. These lasers can be directly modulated at frequencies reaching 20 to 30 GHz. They have important applications in optical links based upon WDM (wavelength division multiplexing) technology. Direct laser modulation schemes are much simpler to implement and integrate than modulation schemes based upon external modulators. However, modulation bandwidth of external modulators can easily go beyond 60 GHz. Thus, it is technologically important to have DFB/DBR lasers whose modulation bandwidths compete with those of external modulators. The goal of this project is to develop DFB and DBR lasers capable of being modulated at high speeds with low distortion and chirp.

High performance DFB and DBR lasers demand that careful attention be paid to the design of the grating, which provides the optical feedback. Spatial hole burning, side mode suppression, radiation loss, laser linewidth, spontaneous emission in non-lasing modes, lasing wavelength selection and tunability, laser relaxation oscillation frequency etc. are all features that are very sensitive to the grating design. Improved grating design can significantly enhance laser performance, especially at higher modulation frequencies. In the last few years various techniques have been developed in Nanostructures Laboratory that allow fabrication of gratings with spatially varying characteristics and with long-range spatial-phase coherence. Chirped optical gratings with spatially varying coupling parameter can be made using a combination of Interferometric lithography, spatially phase-locked electron beam lithography and X-ray lithography. This provides us a unique opportunity for exploring a wide variety of grating designs for semiconductor DFB and DBR lasers. We plan to explore laser devices suited for high speed as well as for low noise operation.

We have developed techniques for fabricating high-speed polyimide-planarized ridge waveguide laser structures that have low capacitance and are therefore ideally suited for high frequency operation. Figure 60 shows the cross section of a polyimide-planarized InP DFB laser. The active region consists of strain compensated InGaAsP multiple quantum wells. The grating and the ridge are dry etched in RIE using a mixture of hydrogen and methane. Planarization is achieved by spinning multiple coatings of polyimide followed by a high temperature cure. Cured polyimide is dry etched in RIE using a mixture of oxygen and carbon tetrafluoride until the top of the ridge gets exposed. Ohmic contact to the ridge is made by lift-off on top of the polyimide layer. The thick layer of polyimide significantly reduces the capacitance between the top metal contact and the substrate. A large value of this capacitance can short out the active region at high frequencies. Figure 61 shows an SEM micrograph of a laser structure fabricated using this process. Figure 62 shows the measured output power from a DFB laser fabricated using the polyimide process. Figure 63 shows the measured spectrum of the DFB laser. Laser characteristics show reasonably high single-mode output power with a side mode suppression ratio of 40 dB.

We are also developing techniques to fabricate co-planar stripline structures for high-speed DFB/DBR lasers. Co-planar striplines offer improved microwave performance compared to microstrip structures. Figure 64 shows a polyimide based co-planar stripline laser structure. Fabrication of this structure requires etching polyimide such that the sidewalls do not become too steep so that metal interconnects can be run over them. We have successfully developed etching techniques for polyimide that allows us to control the sidewall angle. Figure 65 shows an SEM of a metal interconnect running over the sidewall of a polyimide layer.

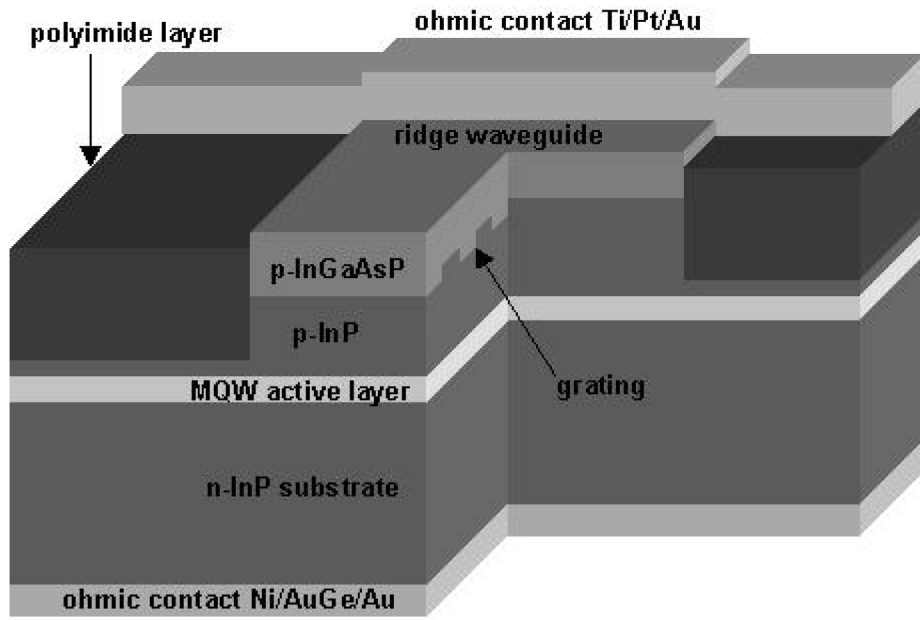


Figure 60: Polyimide planarized DFB ridge waveguide laser.

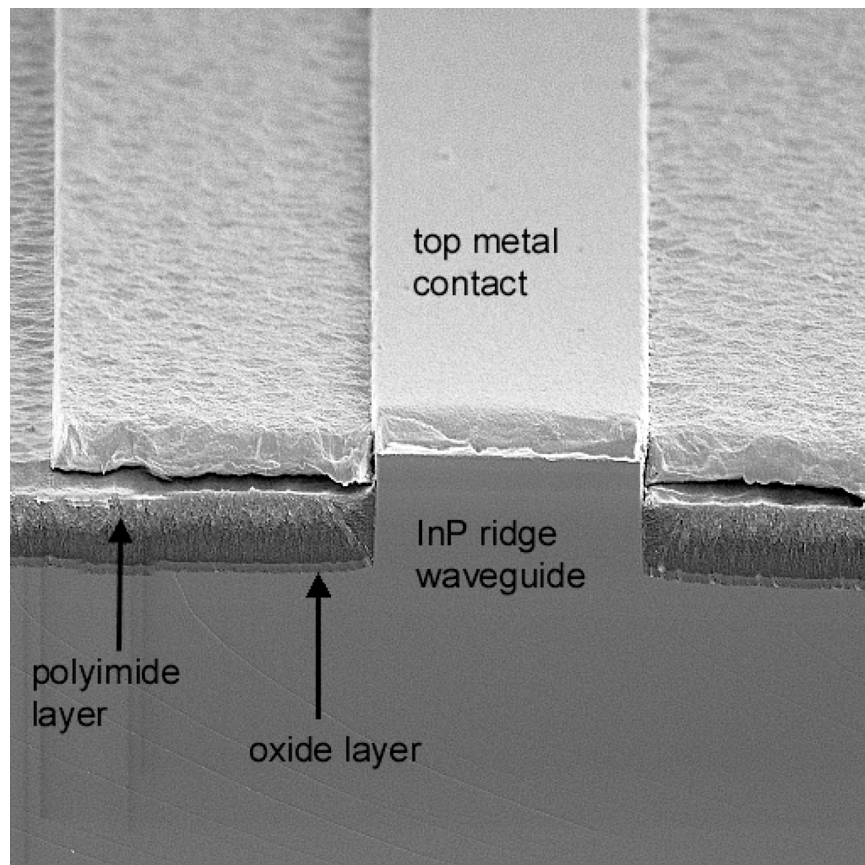


Figure 61: SEM of a polyimide planarized DFB laser.

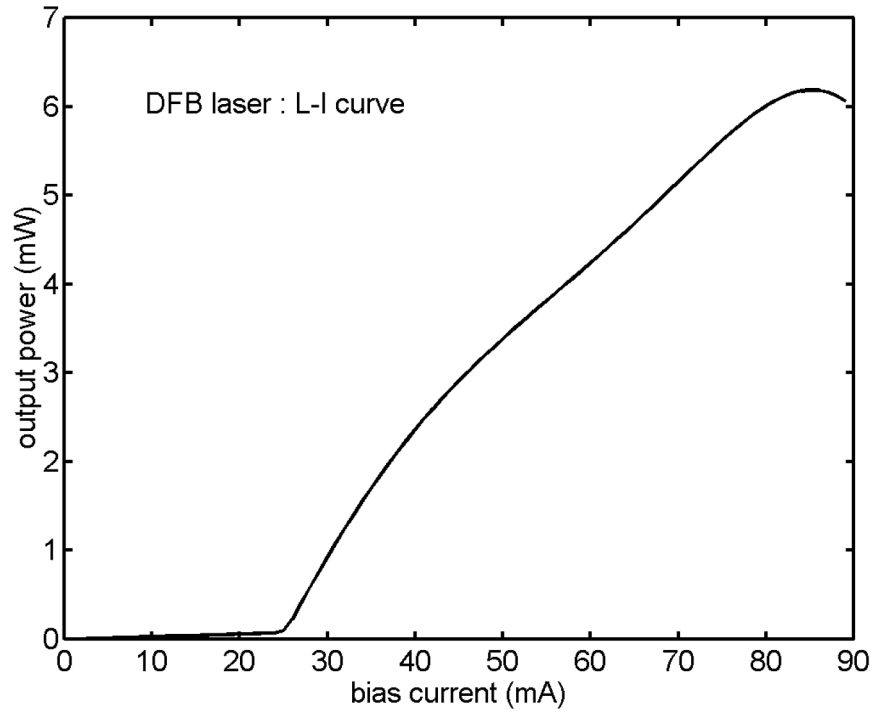


Figure 62: Measured output power from a DFB laser. Maximum single-mode output power is more than 6 mW.

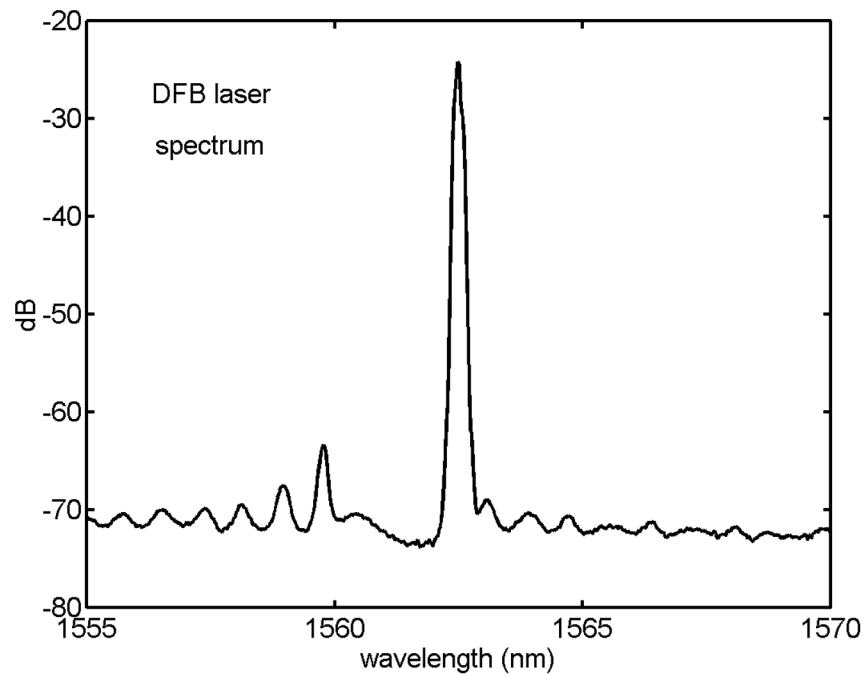


Figure 63: Measured spectrum of a DFB laser. Side mode suppression ratio is 40 dB.

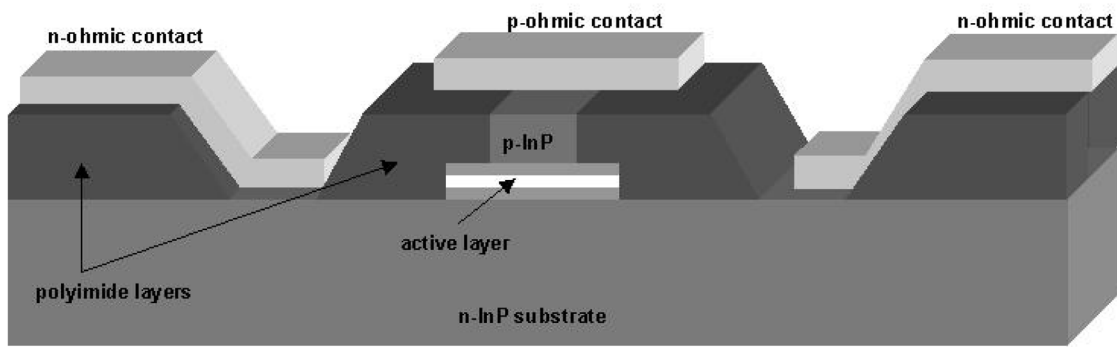


Figure 64: Co-planar stripline DFB laser structure.

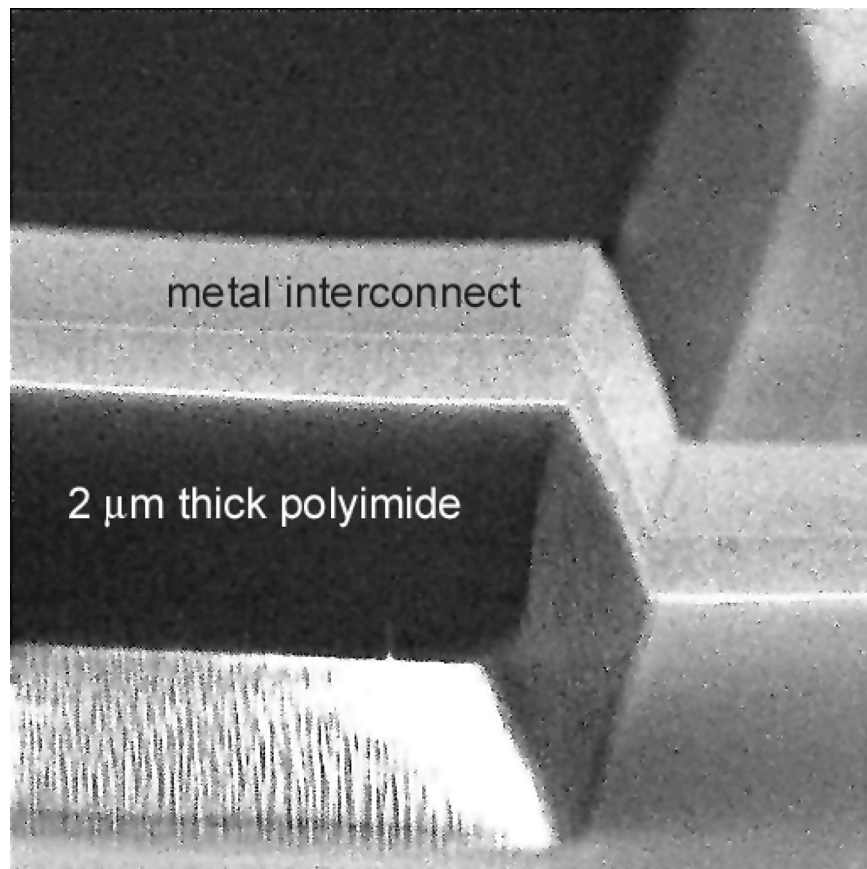


Figure 65: SEM of metal interconnects running over a 2  $\mu\text{m}$  thick polyimide layer.

## 26. Journal Articles, Published

1. D.J. Twisselmann, M. Farhoud, H.I. Smith and C.A. Ross, "In-Plane Magnetic Anisotropy in CoCrPt and CoCrTa Films Deposited Onto Patterned Silicon Substrates", J. Appl. Physics, 85, 4292-4294 (1999).

2. T.A. Savas, M. Farhoud, H. I. Smith, M. Hwang, and C.A. Ross, "Properties of large-area nanomagnet arrays with 100 nm period made by interferometric lithography" *J. Appl. Physics*, **85**, 6160-6162 (1999).
3. K-Y Lim, D.J. Ripin, G.S. Petrich, L.A. Kolodziejski, E.P. Ippen, M. Mondol, H.I. Smith, P.R. Villeneuve, S. Fan, J.D. Joannopoulos, "Photonic bandgap waveguide microcavities: monorails and air-bridges", *J. Vac. Sci. Technol. B* **17**(3), May/June (1999).
4. E.M. Koontz, G.D. U'Ren, M.H. Lim, L.A. Kolodziejski, M.S. Goorsky, G.S. Petrich, and Henry I. Smith, "Overgrowth of (In,Ga)(As,P) on Rectangular-Patterned Surfaces Using Gas Source Molecular Beam Epitaxy", *Journal of Crystal Growth* **198/199** 1104—1110 (1999).
5. J.O. Choi, H.S. Jeong, D.G. Pflug, A.I. Akinwande and H.I. Smith, "Fabrication of 0.1  $\mu\text{m}$  gate aperture Mo-tip field-emitter arrays using interferometric lithography" *Appl. Phys. Lett.*, **74** (20), 3050-3052 (1999).
6. M.L. Schattenburg, C. Chen, P.N. Everett, J. Ferrera, P. Konkola, and Henry I. Smith, "Sub-100 nm metrology using interferometrically produced fiducials (invited)", *J. Vac. Sci. Technol. B* **17**(6), 2692-2697 (1999).
7. E.E. Moon, P. N. Everett, M. Meinhold, M. Mondol and Henry I. Smith, "A Novel Mask-Wafer Gap-Measurement Scheme with Nanometer-Level Detectivity", *J. Vac. Sci. Technol. B*, **17**(6), 2698-2702 (1999).
8. M.H. Lim, T.E. Murphy, J. Ferrera, J.N. Damask and Henry I. Smith, "Fabrication Techniques for Grating-Based Optical Devices", *J. Vac. Sci. Technol. B*, **17**(6), 3208-3211 (1999).
9. M.H. Lim, J. Ferrera, K.P. Pipe and Henry I. Smith, "A Holographic Phase-Shifting Interferometer Technique to Measure In-Plane Distortion", *J. Vac. Sci. Technol. B* **17**(6), 2703-2706 (1999).
10. D.J.D. Carter, D. Gil, R. Menon, M. Mondol and Henry I. Smith, "Maskless, Parallel Patterning with Zone-Plate Array Lithography (ZPAL)", *J. Vac. Sci. Technol. B* **17**(6) 3449-3452 (1999).
11. M. Farhoud, J. Ferrera, A.J. Lochtefeld, M.L. Schattenburg, C.A. Ross and Henry I. Smith, "Fabrication of 200 nm period nanomagnet arrays using interferometric lithography and a negative resist", *J. Vac. Sci. Technol. B*, **17**(6), 3182-3185 (1999).
12. C. A. Ross, H.I. Smith, T. Savas, M. Schattenburg, M. Farhoud, M. Hwang, M. Walsh, M. Abraham, R. Ram, "Fabrication of Patterned Media for High Density Magnetic Storage (invited)", *J. Vac. Sci. Technol. B*, **17**(6) 3168-3176 (1999).
13. R.E. Grisenti, W. Schollkopf, J.P. Toennies, G.C. Hegerfeldt and T. Kohler, "Determination of Atom-Surface van der Waals Potentials from Transmission-Grating Diffraction Intensities", *Phys. Rev. Lett.*, **83**(9), 1755-1758 (1999).
14. C.A. Ross, T.A. Savas, H.I. Smith, M. Hwang and R. Chantrell, "Modelling of Hysteresis Loops of Arrays of 100 nm Period Nanomagnets", *IEEE. Trans. Magnetics*, **35**, 3781-3783 (1999).

### **26.1 Journal Articles, Submitted for Publication**

1. R.E. Grisenti, W. Schoellkopf, J.P. Toennies, J.R. Manson, T.A. Savas and H.I. Smith, "He Atom Diffraction from Nanostructured Transmission Gratings: The Role of Imperfections", Submitted to *Phys. Rev. A*, March 1999.

2. D. G. Pflug, M. Schattenburg, H.I. Smith and A.I. Akinwande, "Mo Cone field Emission Arrays with 100-nm Gate Aperture", submitted to *Electron Device Letters*, 1999.

### **26.2 Meeting Papers, Published**

1. J. Goodberlet, "A Very-High-Density Scintillation-Data-Storage Device", *Microelectronic Engineering* 46 145-148 (1999).
2. D.J.D. Carter, H.I. Smith, K.W. Rhee and C. Marrian, "Sub-40nm pattern replication with +/- 20% process latitude by soft contact x-ray lithography", *Proceedings of SPIE's 24th Annual International Symposium on Microlithography, Emerging Lithographic Technologies III*, 14-19 March 1999, Santa Clara, CA. SPIE vol. 3676, pp.70-78 (1999).
3. D.J.D. Carter, D. Gil, R. Menon, I. J. Djomehri and Henry I. Smith, "Zone-Plate Array Lithography (ZPAL): A new maskless approach", *Proceedings of SPIE's 24th Annual International Symposium on Microlithography, Emerging Lithographic Technologies III* 14-19 March 1999, Santa Clara, CA. SPIE vol. 3676, pp.324-332 (1999).
4. T. E. Murphy, B. E. Little and H. I. Smith, "Wavelength-and Polarization-Insensitive Integrated Directional Couplers using Mach-Zehnder Structures," in *Integrated Photonics Research, OSA Technical Digest*, pp. 138-140, July (1999).

### **26.3 Meeting Papers, to be published:**

1. J.T. Hastings, F. Zhang, A. Bernshteyn, J.G. Goodberlet and H.I. Smith, "Improved Pattern-Placement Accuracy in E-Beam Lithography Via Sparse-Sample Spatial-Phase Locking", Submitted to *Micro & Nano Engineering*, (1999).
2. J.G. Goodberlet, B.L. Dunn, "Deep-Ultraviolet Contact Photolithography", Submitted to *Micro & Nano Engineering*, (1999).
3. H.I. Smith, "Soft x-rays for deep sub- 100 nm lithography, with and without masks", Submitted to *Micro & Nano Engineering*, (1999).
4. R. Menon, D. J. D. Carter, D. Gil, and H. I. Smith, "Zone-Plate-Array Lithography (ZPAL): Simulations for System Design", to be published in the *Proceedings of the Vth International Conference on X-ray Microscopy (XRM99)*, Berkeley, CA., August 1-6 (1999).
5. H. I. Smith, D. J. D. Carter, J. Ferrera, D. Gil, J. Goodberlet, J. T. Hastings, M. H. Lim, M. Meinhold, R. Menon, E. E. Moon, C. A. Ross, T. Savas, M. Walsh, F. Zhang, "Soft X-Rays for Deep Sub-100 NM Lithography, with and without masks", *Materials Research Society Meeting*, Boston, MA., November 29-December 2 (1999).

### **26.4 Conference Presentations:**

1. K. Murooka, M. H. Lim, J. Ferrera, and Henry I. Smith, "X-ray lithography below 100 nm: An approach to eliminating distortion", *XEL 1999*, Yokohama, Japan, November 1999.

### **26.5 Theses:**

1. J. Bae, "A Data Storage System Based on Patterned Magnetic Media and Magnetic Force Microscopy", M.S. Thesis, Department of Mechanical Engineering, MIT, May 1999.

2. V. Chan, "Ceramic Nanostructures from Block Copolymers", Ph.D. Thesis, Department of Materials Science and Engineering, MIT, October 1999.
3. J. Ferrera, "Nanometer-Scale Placement in Electron-Beam Lithography", Ph.D. Thesis, Department of Electrical Engineering and Computer Science, MIT, October 1999.